PHD

Positron studies of ion implanted silicon

Mason, Ruth Elizabeth

Award date:
2006

Awarding institution:
University of Bath

POSITRON STUDIES OF ION IMPLANTED SILICON

RUTH ELIZABETH MASON

A thesis submitted for the degree of Doctor of Philosophy

University of Bath
Department of Physics
August 2006

ProQuest LLC
789 East Eisenhower Parkway
P.O. Box 1346
Ann Arbor, MI 48106-1346

DECLARATION

Bath, August 2006

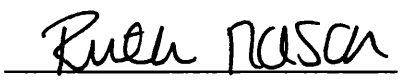

RUTH ELIZABETH MASON

To my Dad

ACKNOWLEDGEMENTS

Firstly I would like to express how extremely grateful I am to my supervisor Paul Coleman for all his help and support throughout the duration of this PhD. Without his enthusiasm, brilliant scientific insight and experimental prowess none of this work would have been possible. In recent months his patience, encouragement and generosity of time have been humbling.

I would also like to thank Paul Burrows, Xio Dong Pi and Harry Bone for technical and practical help in the lab.

Many thanks are due to my family for all their practical and emotional support, especially my Dad. A big thank you to my wonderful sisters Ellie and Bridget for their love, belief in me and motivational stationery (motivationery). Thanks to my Dad and his wife Carole for the emotional, financial and computational support; I am very grateful for the laptop loan when mine died at such a critical moment. Also many thanks to Bridget and Keith for the amazing printer and a special thank you to Bridget for proof reading it.

Thank you David for making what should have been an unpleasant time so lovely. You have been an unwavering source of support and I will miss sharing my daytimes with you!

And finally thanks to Ashraf Alam for first suggesting I did a PhD. It has been one of the most enlightening and interesting experiences of my life.

I would like to acknowledge the EPSRC studentship that made this work possible.

ABSTRACT

The well established technique of Variable Energy Positron Annihilation Spectroscopy (VEPAS) is utilised in a number of novel ways to examine vacancy defects in condensed matter. Three separate studies were carried out which are presented here; direct observation of monovacancies in ion implanted silicon, enhanced resolution depth profiling defects in ion implanted silicon and characterisation of thin ferromagnetic films before and after rapid thermal annealing (RTA). Descriptions are given of the theory of VEPAS, the relevant analysis techniques and the experimental apparatus; a variable mono-energetic positron beam with the various refinements necessary.

In normal experimental circumstances monovacancies are unobservable because they anneal to divacancies at room temperature. This was overcome by maintaining a low temperature (<100K) while creating the damage *in situ* and taking positron measurements. First measurements for 6keV He implantation, at post-implant temperatures between 60 and 300K, are presented. Benefits and drawbacks of the system are discussed.

The depth distribution of open-volume point defects created by room-temperature implantation of Cz silicon by 100 keV B^+ ions at a dose of 5 $x10^{14}$ cm^{-2} has been determined by using an incremental etch and measure technique allowing deep defect structures to be probed with a resolution that is usually restricted to the near surface region. The results presented here are in good agreement with Monte Carlo simulations, particularly in the traditionally difficult-to-measure deep tail region.

The VEPAS measurements of a series of ferromagnetic thin films grown at different temperatures in the presence of different gas mixtures before and after RTA are presented. The possible factors that influence the effect of the RTA are discussed.

CONTENTS

CHAPTER 1

INTRODUCTION AND BACKGROUND

CHAPTER 2

BEAM SET UP AND ANALYSIS OF RAW DATA

CHAPTER 1

INTRODUCTION AND BACKGROUND

1.1 Introduction

The positron is the antiparticle of the electron having the same mass (511keV) and the same spin (1/2) but opposite charge and magnetic moment. It has a long lifetime ($\tau > 2 \times 10^{21}$years) in a vacuum and is effectively stable but in solids it only has a lifetime of a few hundred picoseconds before it annihilates with an electron or is re-emitted either as a free particle (e+) or by picking up an electron and forming a bound state, positronium, Ps. Positrons were first discovered by Anderson in 1932 using a bubble chamber while studying cosmic rays [1.1]. Four years prior to Anderson's discovery, Dirac had postulated the existence of the positron to explain the negative energy solutions of the Dirac Equation [1.2].

Since its discovery the positron has been used in broad applications in many areas of science including Medical Physics and Materials Science. This is because once implanted into condensed matter positrons localise at low electron density sites such as vacancies, surfaces, free volumes, holes, pores and voids. The subsequent annihilation with an electron will produce gamma radiation which will betray the electronic environment in which it decayed. It is for this reason that positrons are now used so widely as a probe of matter. The review paper of [1.3] gives a comprehensive account of positrons and their uses in solid state physics.

The following thesis uses the well established technique of Variable Energy Positron Annihilation Spectroscopy (VEPAS) in a number of novel ways to examine defects in condensed matter; from silicon to thin ferromagnetic films.

The defects are introduced either through the growth process or via ion implantation. The silicon under examination is from high purity wafers that have been grown by the Czochralski method (Cz Si) or the Float Zone method (FZ Si) The float zone method results in silicon with fewer than 10^{16} oxygen ions per cm^3

compared to 10^{18} cm^{-3} introduced from impurities in the crucible in the case of the Cz method.

This first chapter is a detailed description of the main theory involved in the application and analysis of positron annihilation when used to characterise defect structures in solids. Emphasis is on the VEPAS technique but brief explanations of other positron methods are given. The second chapter details the experimental set up and refinement of the positron beam apparatus that was used throughout to take the relevant measurements.

Chapter 3, 4, and 5 are the results chapters and contain three separate studies addressing monovacancies, positron resolution enhancement and characterisation of thin ferromagnetic films respectively.

The study of Chapter 3 was an attempt to directly observe a particular type of damage in silicon that is created during ion implantation; monovacancies. In normal experimental circumstances they are unobservable because they anneal to divacancies at room temperature. This was overcome by maintaining a low temperature (<100K) while creating the damage *in situ* and taking positron measurements. This was the first study of its kind.

Chapter 4 was the development of a new measurement and analysis technique with the aim of overcoming the decrease in resolution as a result of implanting higher energy positrons. The technique allows deep defect structures to be probed with a resolution that used to be restricted to the near surface region.

The subject of Chapter 5 is the result of a collaboration between The University of Dundee, Qinetiq and the Slow Positron Group at The University of Bath. The positron beam facilities at Bath were used to characterise the structure of ferromagnetic thin films before and after rapid thermal annealing (RTA).

1.2 Positron Experiments

The basic principle of all positron experiments is that when a positron is implanted into condensed matter it will thermalise, diffuse and annihilate with an

available electron. The annihilation radiation (two gamma photons) produced is observed and measured. Which aspect of the annihilation radiation (energy, time, direction) is measured depends on the particular positron technique in use.

There are three main positron techniques; Positron Annihilation Spectroscopy, (PAS) which measures the energy of the annihilation radiation, Lifetime Spectroscopy which measures the lifetime of the positron in the solid before annihilation and finally, Angular Correlation of the Annihilation Radiation (ACAR) which measures the angle between the annihilation photons.

Conventional PAS techniques are used for bulk studies, but by controlling the energy of implanted positrons it is possible to depth profile defects. This method is called Variable Energy Positron Annihilation Spectroscopy (VEPAS) and would usually require the use of a positron beam. The depth that the positrons are implanted to can be controlled by altering the implantation energy and thus measurements are taken as a function of depth.

In order to form a mono-energetic positron beam it is necessary to obtain a decent intensity of slow positrons. Positrons can be produced by pair production using a Linear Accelerator (LINAC) or from positive beta decay of a radioactive source such as ^{22}Na which is a common source used by many laboratories in their positron beam systems. In order to form a beam the emitted positrons, which have a broad spectrum of energies, need to be slowed down, a process known as moderation. Fast positrons can be moderated by implanting them into a metal as a small proportion will be re-emitted as slow positrons. This phenomenon arises from the fact that some metals have a negative positron work function. The re-emission of slow positrons from chromium was first observed by Cherry [1.4] in 1958 at Princeton University. The results were not widely known as they were in an unpublished Ph.D thesis. It was not until ten years later that slow positrons were rediscovered by the group at The Gulf Energy and Environment in San Diego [1.5] Since then slow positron intensities have increased almost yearly enabling the technique to be applied to many phenomena. Chapter 1 of [1.6] gives a more detailed account of the history and development of low energy positron beams.

As positrons preferentially localise in vacancies and voids when implanted into solids they are most useful for studying vacancy type defects. Vacancy type defects are formed in huge numbers during the process of ion implantation used to dope semiconductors. During the high energy ion bombardment, the ions in the target become dislodged from their lattice sites and create Frenkel pairs; interstitials and vacancies. Many of these pairs will recombine during annealing but some vacancies will combine with each other to form larger, more stable vacancies. The microelectronics industry is demanding ever decreasing device dimensions [1.7] which means that imperfections in the doped semiconductors used in fabrication play a more significant role in the electronic functioning of the resulting devices. Hence it is more important than ever to understand the formation and behaviour of the defects that are created during the doping process.

1.3 Positrons within Solids

When positrons are implanted into condensed matter there are a number of different interactions and paths they can take. Figure (1.1) [1.8] shows the possible fates of slow positrons from a beam when incident on a solid surface. If the target is single crystal some of the incident positrons will scatter elastically and form a diffracted beam. The rest of the incident positrons will go through a variety of inelastic processes before being re-emitted or annihilating with electrons.

After implantation, the positrons that penetrate are slowed down to thermal energies through inelastic collisions with conduction and core electrons. Known as thermalisation this takes ~1ps, a small proportion of the total lifetime which is between 100ps and 500ps depending on the material. After losing most of their energy the positrons diffuse freely through the solid until annihilation with an electron occurs producing two gamma rays of ~511keV which is the predominant decay route. The positron is thermalised but the electron has an appreciable energy due to the Pauli Exclusion Principle. This means the annihilating pair have a small net momentum which gives rise to the gamma radiation deviating from collinearity and the energy being Doppler shifted.

A fraction of the implanted positrons will diffuse back to the surface and are re-emitted as free particles, or fall into the surface potential and annihilate there, or pick up an electron and leave the surface as positronium, Ps. Positrons that return to the surface and are re-emitted before thermalisation are called epithermal positrons.

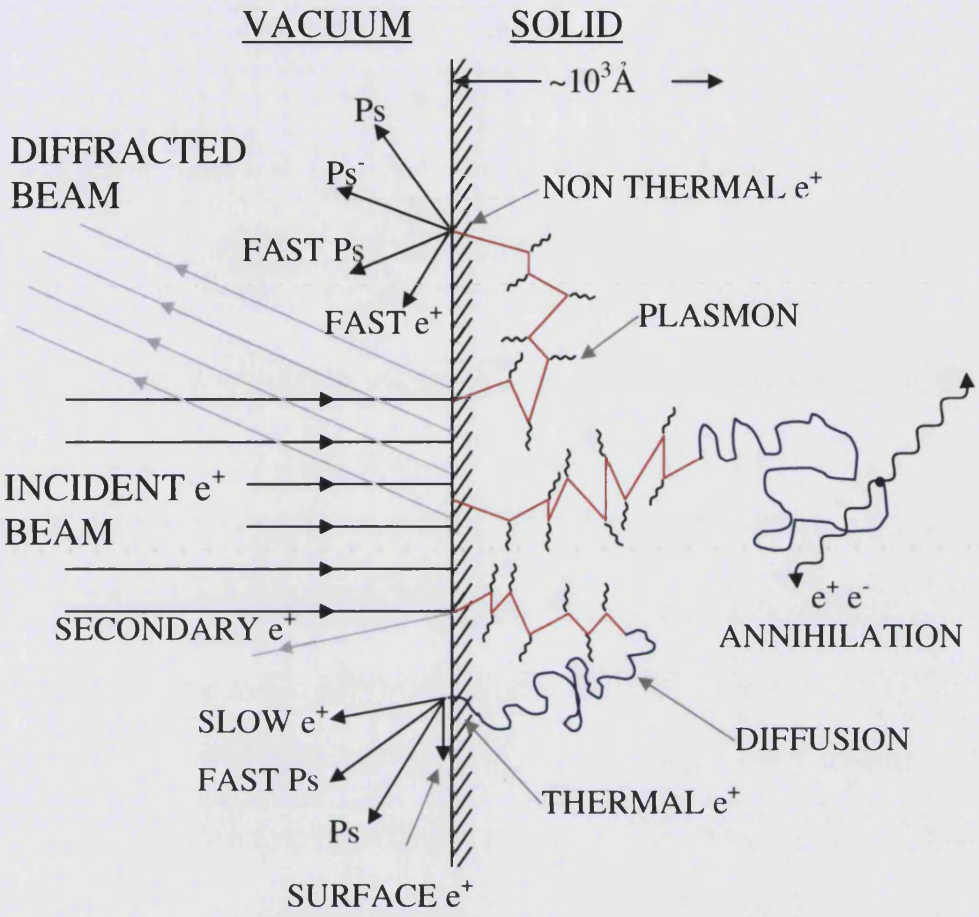

Figure (1.1) All possible fates of slow positrons from a beam implanted into condensed matter. Some of the positrons are elastically diffracted. Of the positrons that penetrate, energy is lost through core ionization as the positrons thermalise. However before thermalisation occurs some positrons may get back to the surface and escape either as a fast positron or as a bound state of an positron and an electron called positronium (Ps) which maybe in its ground state, or excited (Ps*). Some of the thermalised positrons also get back to the surface by diffusion. Again they may be emitted as Ps, Ps* or as slow positrons. They also can get trapped at the surface and annihilate there. The thermalised positrons that do not diffuse back to the surface, will annihilate with an electron either in bulk or in defects. This diagram is adapted from the one in [1.8]

1.3.1 Thermalisation

The positrons that are not backscattered or diffracted lose their high kinetic energy and reach thermal equilibrium with their surroundings; a process called thermalisation. The large energy is dissipated in the crystal lattice by inelastic scattering with core and conduction electrons. Once the energy of the positron is in the tens of eV then the energy loss processes that occur depend on the class of solid. The energy loss processes in semiconductors and metals are similar. For a positron in a metal, electron and plasmon scattering dominate until the positron energy is well below the Fermi Energy, E_F. Then phonon scattering dominates until thermal energies are reached. A positron in a semiconductor will lose energy through electron hole excitation until its energy drops below that of the band gap energy, E_g. Then like metals the less efficient energy loss process of phonon scattering will dominate.

Thermalisation time in insulators is prolonged as by definition E_g is bigger than in semiconductors so phonon scattering dominates to higher energies. Energy loss can also take place via positronium formation which isn't possible in the bulk of metals or semiconductors because the large electron densities screen the interaction.

1.3.2 Surface Re-emission and Moderation

The average distance the positron travels after thermalisation is called the effective diffusion length, L_{eff}. Implanted positrons that thermalise within L_{eff} of the surface have a probability of diffusing back to the surface. This fraction depends on the implantation energy; at lower energies more positrons will thermalise in this region and a greater fraction will return to the surface.

Once at the surface they can either be trapped by and annihilate in the surface potential or be re-emitted into the vacuum as free particles. These free particles are free positrons or positrons that have picked up an electron and formed a bound state, of positronium, Ps. The free slow positrons that are re-emitted into the

vacuum have a kinetic energy corresponding to the work function of the solid they are emitted from [1.9].

This spontaneous re-emission into the vacuum is the basis of moderators, which are materials used to slow down fast positrons emitted from radioactive sources in order to form mono-energetic beams. The work function of a material for a particle, be it a positron, $\varphi+$, or an election, $\varphi-$, is defined as the energy required to remove the particle from the bulk to a point outside the material where the surface no longer has any influence on it. For both electrons and positrons, the work function is made up of two components; a bulk contribution which is the chemical potential, $\mu+$ or $\mu-$, and a surface contribution which is the dipole barrier, D, caused by the tailing of the electron distribution into the vacuum. For positrons, D acts out of the material and for electrons it acts into it. This means that $\varphi+$ is very small and sometimes even negative which allows emission of slow mono-energetic positrons into the vacuum [1.3].

Accordingly moderators are materials, mostly metals, with negative positron work functions so that positrons implanted at low energies will diffuse back to the surface and be re-emitted with an energy corresponding to the work function of the material. The probability of re-emission is increased if there are no non equilibrium defects in the material which can be achieved by annealing in situ at a 80% of the melting temperature [1.6]. Tungsten is a common moderator material and it has been found that several layers of tungsten mesh increases the slow positron efficiency. This is also covered in §2.2.2

1.3.3 Positronium

Positronium is a bound state of an electron and a positron and has a vacuum binding energy of 6.8eV. There are two forms depending on whether the spins of the electron and positron are parallel (para-positronium) or opposite (ortho-positronium) with natural lifetimes of 125ps and 142ns and preferential decay into 2-γ and 3-γ respectively. The 3-γ decay of ortho-positronium presents a straightforward method for identifying positronium [1.10].

For semiconductors and metals Ps is only formed outside the crystal because of the effective screening by electrons in the lattice. This means that the formation of Ps will play no significant role in the research described in this thesis.

1.3.4 Epithermal Positrons

At low incident positrons energies, ≤1 keV, a fraction of the positrons reach the surface before thermalisation. These are called epithermal positrons and can also form positronium at the surface and be re-emitted to vacuum as fast positrons, fast Ps or an excited state of positronium, Ps*.

If fast p-Ps is formed [1.11] and emitted, because it only travels 1mm before annihilation it can affect the results obtained taken in VEPAS. A spectrum of the annihilation radiation is collected which has a distribution around the 511keV line due to Doppler broadening because the annihilating pair have a non zero momentum. As the positronium is high momentum, annihilating in sight of the detector would lead to a broader annihilation line.

Epithermal yields have been measured by Knights and Coleman [1.12] from a number of materials and are found to drop rapidly as the incident energy increases and are insignificant above 1keV. As far as epithermal positrons being trapped by defects below the surface are concerned, it has been shown that non thermal trapping was not important in aluminium and it is commonly accepted that this is also the case for semiconductors [1.13].

1.3.5 Diffusion and Annihilation

After thermalisation, the positrons that have not returned to the surface will diffuse through the lattice as charged particles. At any one time the probability is that there is only one positron in the solid so it will be in its lowest energy band. Due to the positive repulsion of the ion cores the largest position probability is in the interstitial regions. If the material has any open volume defects then the positrons will be attracted to these sites as the repulsive potential will be absent. For a given positron implantation energy a fraction will annihilate in bulk and a fraction will annihilate in defects. The relative fractions of these two annihilation

locations depends on the concentration of defects per atom, the trapping rate of the defect and the positron decay rate.

Annihilation is a relativistic process in which the particle masses are converted into energy in the form of electromagnetic radiation; gamma photons. The main decay route is to 2-gamma as 1-gamma decay requires the presence of a third body to absorb recoil momentum and 3-gamma has a spin averaged cross section of 0.27% that of 2-gamma [1.10]. This is small enough to be neglected.

1.3.6 Implantation Profiles

By controlling the energy of incident positrons it is possible to measure defects as a function of the penetration depth, z. The stopping or implantation profile is called a Makhovian distribution after Makhov [1.14]. The distribution of depths z (nm) of slow positrons at the implantation energy E (keV) in a material of density ρ (gcm^{-3}) is given by equation (1.1) the Makhov profile [1.15] [1.3]:

$$P(z,E) = \frac{mz^{m-1}}{z_0^m} \cdot \exp\left(-\left(\frac{z}{z_0}\right)^m\right) \tag{1.1}$$

where z_0, defined by equation (1.2) is a parameter related to the mean implantation depth, $\bar{z}$, (equation (1.3)) and empirically determined parameter m:

$$z_0 = \frac{\bar{z}}{\Gamma\left(1+\frac{1}{m}\right)} \tag{1.2}$$

where:

$$\bar{z} = \frac{A}{\rho} \cdot E^r \tag{1.3}$$

The mean implantation depth, eqn (1.3) is related to the empirically determined parameters A, and r. Widely used values for the parameters m, A, and r are: m = 2. A = 40 $mg.m^{-2}$ $(keV)^{-1.6}$, and r = 1.6 [1.16] for z_0 in nm. For the value of m=2 the Gamma function is $\Gamma(1.5) = \pi^{1/2}$ so $z_0 = 1.13\,\bar{z}$.

The profile has been determined experimentally by Mills and Wilson [1.17] to be close to the derivative of a Gaussian. The distribution can also be obtained theoretically [1.18][1.19] using Monte Carlo simulations and it has been shown that the fitting parameters depend on the material and the scheme used [1.20].

The FWHM of the implantation profile is approximately equal to the mean implantation depth. As a result the sensitivity in depth of positrons with energies higher than 10keV is reduced significantly. A novel method to eliminate this problem is addressed in Chapter 4 in detail. The implantation profile is also dependent on the density of the material used, which for the most part in this thesis is silicon (density of 2.321 gcm^{-3}) but in Chapter 5 Lead Scandium Tantalate, $Pb(Sc_{0.5},Ta_{0.5})O_3$ (PST) is examined which has a density of 9.1 g cm^{-3}. It is interesting to compare the implantation profiles and mean implantation depths of these two densities at 10keV and 20 keV (see figure (1.2)). In both cases the profiles broaden as the energy increases. The denser material stops positrons penetrating as deeply at comparable energies.

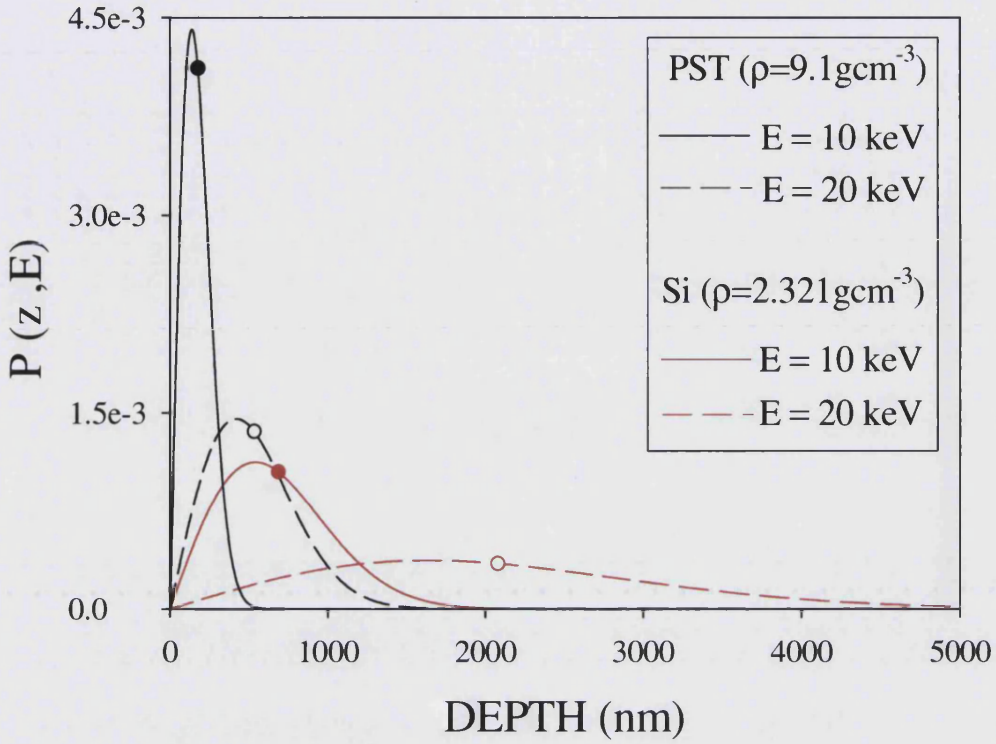

Figure (1.2) Makhovian implantation profiles obtained from equations (1.1)-(1.3) for 10keV and 20 keV positrons implanted into: Si (ρ =2.321gcm^{-3})and lead scandium tantalate, $Pb(Sc_{0.5},Ta_{0.5})O_3$ (PST) (ρ = 9.1 gcm^{-3})Data points are mean implantation depths of each profile.

1.4 Positron Techniques

There are a number of positron techniques that are able to detect open volume defects. They all rely on the fact that due to the missing ion there is no longer a repulsive potential and the resulting vacancy sites act as positron traps. Due to the lower electron density at these sites, trapped positrons will on average have longer lifetimes than un-trapped positrons in the bulk. When a trapped positron eventually annihilates with an electron it is more likely to be with a low momentum valence electron. On average, trapped positrons will annihilate with greater numbers of lower momentum valence electrons than positrons in the bulk which will annihilate with greater numbers of higher momentum core electrons.

The three main techniques are Angular Correlation of Annihilation Radiation (ACAR), Positron Annihilation Spectroscopy (PAS) and Lifetime Spectroscopy. The first two of these techniques, (ACAR and PAS) obtain information about the momentum states of the electron-positron pair prior to annihilation from which defect information is obtained. Lifetime Spectroscopy obtains defect information from the lifetime spectra of positrons. Below is a brief overview of the ACAR and Lifetime Spectroscopy. For a more comprehensive review of these other techniques see the review paper of [1.3].

1.4.1 Lifetime Spectroscopy

The time between implantation and annihilation is known as the positron lifetime. The average lifetime varies between 100ps and 500ps depending on the type of solid and the concentration and size of vacancy type defects. Positrons will be attracted to the defects as the repulsive ion is missing. In this effective positron trap the positrons will live longer relative to lifetimes in the bulk because of lower electron densities.

If lifetime experiments are using ^{22}Na as a source then the 1.27 MeV gamma photon that is emitted simultaneously with the positron is the 'birth' signal and the 511 keV gammas emitted at annihilation are the 'death' signals. The value of the longer positron lifetime component is a measure of the size of the open volume defects and the intensity is related to the defect concentration.

1.4.2 Angular Correlation of Annihilation Radiation (ACAR)

The positron is in thermal equilibrium when it annihilates with an electron and therefore has effective zero momentum. The same cannot be said of the electron as it is densely packed with millions of other electrons. The electron is a fermion and so must obey the Pauli Exclusion Principle, i.e. each energy state can only be occupied by one electron of each spin. This means that the electron has a small but significant momentum which as a consequence of momentum and energy conservation laws affects the direction and energy of the annihilation radiation.

In the centre of mass frame the gamma photons are collinear in direction and each have energy of exactly 511keV. However, as the annihilating pair actually has a small momentum, **P**, in the laboratory frame the energy is Doppler shifted by ± c**P**/2 where c is the speed of light (see § 1.5.1). As a result the photons will deviate from collinearity by a small angle $\Theta = \mathbf{P}_T / m_0 c$ (where m_0 is the rest mass of positrons/electron and $\mathbf{P}_T$ is the component of the momentum transverse to the direction of the gamma photons). This angular deviation is what is measured in ACAR and is usually smaller than 1°.

1.5 Variable Energy Positron Annihilation Spectroscopy (VEPAS)

In conventional PAS a radioactive source is sandwiched between two identical samples. The fast positrons annihilate in the bulk of the sample and the annihilation radiation measured. The advantage of this method is that it can be performed in air. However it can only be used to study bulk properties and the samples must be thick enough to ensure that a significant proportion of the positrons annihilate within the sample. By using a beam of mono-energetic positrons in a vacuum it is possible to control the positron energy and therefore study defects as a function of depth. It is also possible to study surfaces and very thin layers. This technique is called Variable Energy Positron Annihilation Spectroscopy (VEPAS) and is described in some detail as it is the technique that is used in this thesis. The data obtained from VEPAS experiments is analysed using a fitting program; a commonly used one is VEPFIT [1.21].

As with ACAR, VEPAS uses the fact that the annihilating pair have a non zero momentum. This gives rise to Doppler shifted gamma radiation which is used to determine defect information in the immediate vicinity of the electron-positron pair at the point of annihilation. Positrons trapped in defects will be more likely to annihilate with lower momentum valence electrons resulting in a smaller Doppler shift of the annihilation radiation with respect to undefected bulk.

1.5.1 Doppler Broadening

The component of the positron-electron pair, $\boldsymbol{p}$, in the direction of the emission of the annihilation photon gives rise to a Doppler shift in the photon energy of $c\boldsymbol{p}/2$ where c is the speed of light. This is derived below: Figure (1.3) is a schematic of the energies and momentums before and after annihilation.

(a) BEFORE ANNIHILATION

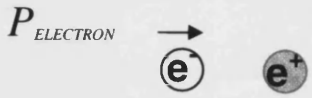

(b) POST ANNIHILATION

Figure (1.3) Diagram of energies, and momentums before **(a)** and immediately after **(b)** annihilation of a thermalised positron and an electron of momentum $P_{ELECTRON}$.

Prior to annihilation the energy of the system of a single electron and positron is composed of their rest masses, m_0, and the momentum of the pair, $\boldsymbol{p}$, of which the significant contribution will be from the electron, ($P_{ELECTRON}$ and $E_{ELECTRON}$) as the positron will have thermalised. Compared to their rest masses, the energy of the electron is very small so the total energy is given by eqn (1.4):

$$m_0c^2 + m_0c^2 + E_{ELECTRON} \approx 2m_0c^2 \qquad (1.4)$$

Post annihilation there are two gamma photons travelling in opposite directions. The energies will be Doppler shifted by -ΔE and by +ΔE. The photon travelling to the right (in this diagram) has energy and momentum given by equations (1.5) and (1.6):

$$E_{\gamma-right} = m_0c^2 + \Delta E \qquad (1.5)$$

$$P_{\gamma-right} = \frac{m_0 c^2 + \Delta E}{c} \tag{1.6}$$

For the gamma travelling to the left:

$$E_{\gamma-left} = m_0 c^2 - \Delta E \tag{1.7}$$

$$P_{\gamma-left} = \frac{m_0 c^2 - \Delta E}{c} \tag{1.8}$$

After the annihilation the total momentum to the right must be conserved and therefore be equal to $P_{ELECTRON}$ which is in turn equal to $\boldsymbol{p}$:

$$P_{\gamma-right} - P_{\gamma-left} = P_{ELECTRON} = \frac{2\Delta E}{c} \tag{1.9}$$

$$\Delta E = \frac{1}{2} c P_{ELECTRON} \tag{1.10}$$

So the energy shift of each gamma is given by (1.11)

$$E = m_{e\pm} c^2 \pm \frac{1}{2} c\boldsymbol{p} \tag{1.11}$$

where $\boldsymbol{p}$ is the momentum of the annihilation pair.

1.5.2 Shape Parameters

From eqn (1.11) it is clear to see that the larger the momentum of the annihilating pair, the greater the Doppler shift of the annihilation radiation. In VEPAS the energy of all the annihilating gammas are measured with a solid state detector such as a germanium detector. By taking many counts over a period of time a spectrum is built up which has a distribution either side of the 511keV annihilation line. Figure (1.4) is an example of such a distribution. As the resolution of such a detector is typically ~1keV and is therefore not very narrow compared to the line broadening, the observed broadened profiles are relatively smooth and featureless.

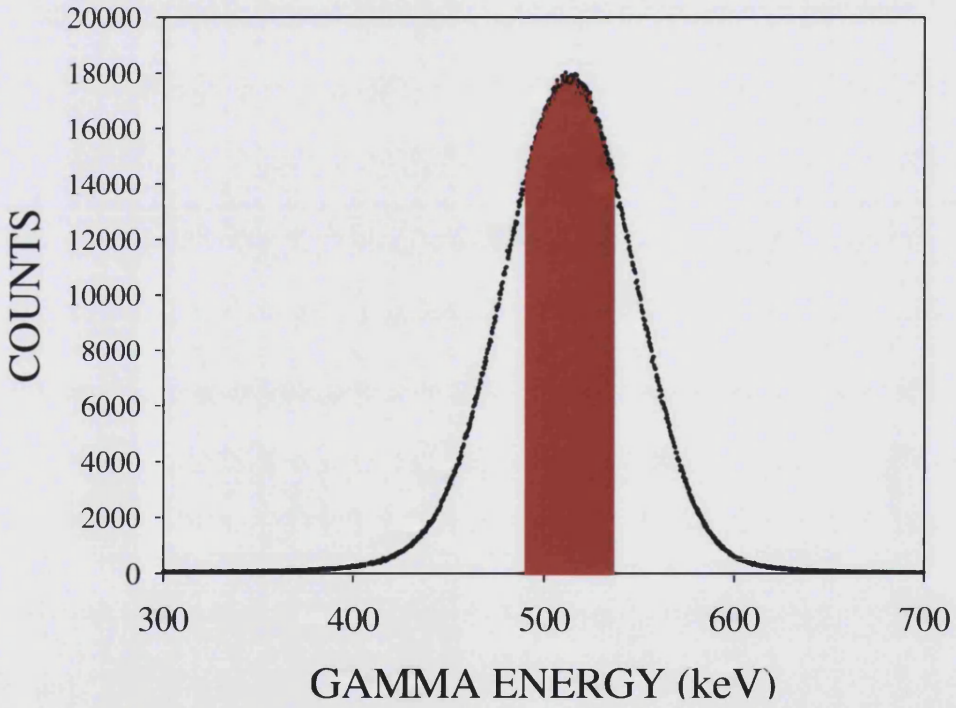

Figure (1.4). An actual spectrum of the Doppler shifted gamma photons showing the distribution of energies of the gamma radiation. They are both above and below the 511keV line depending whether they are travelling towards or away from the detector.

It is the shape of this spectra that is measured and used to compare different samples, regions and depths. The information in this spectra is encapsulated in two shape parameters; *S* and *W* which give the relative proportions of counts in

the different parts of the spectra. The *S* parameter is the Sharpness parameter and is the ratio of counts in the central region (shaded red in fig. (1.4)) to the total number of counts. The *W* parameter is the Wing parameter and is the ratio of the counts in the wings to the total counts. Figure (1.5) is a diagram of an idealised spectrum showing how *S* and *W* are calculated from equations (1.12) and (1.13) The positions of A, B, C, D E and F were traditionally fixed so that for a defect free material S= 0.5 and W= 0.25. However following Monte Carlo simulation work on the optimization of limits [1.22] it was found that S=0.6 and W=0.3 are optimum values for vacancies in silicon. For most of the new data presented these optimised values are used. However for the older data in Chapter 5 the regions were still defined such that *S*~ 0.5 and *W*~0.25.

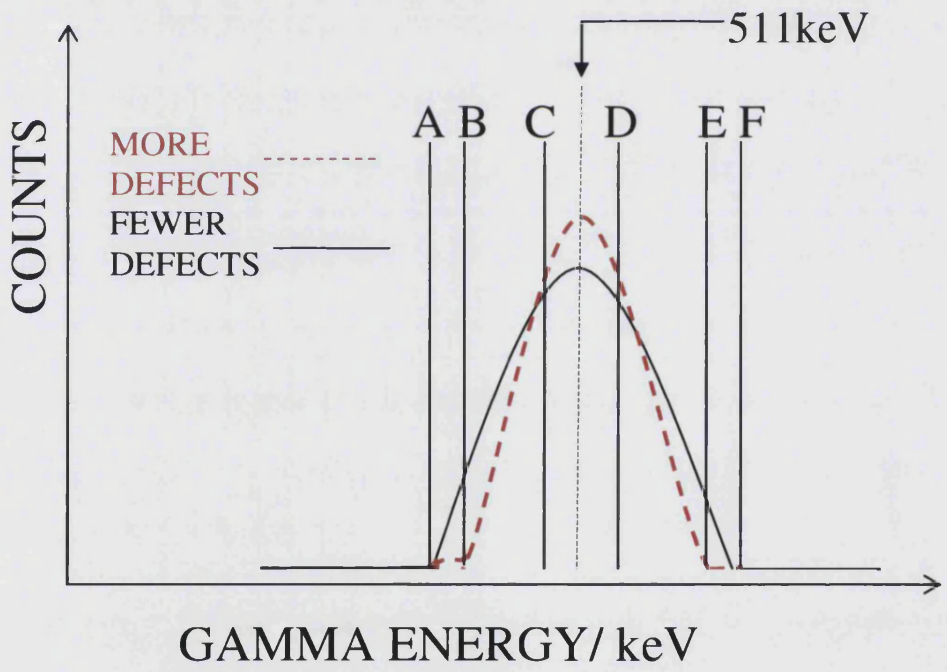

Figure (1.5) Diagram of two Doppler Spectrums showing the regions that define the *S* and W parameters. The red dotted spectrum shows a result with more defects relative to the black solid spectrum. The definitions of *S* and W with reference to this diagram are given by equations (1.12) and (1.13)

$$S = \frac{Counts\ in\ CD}{Total\ counts} \tag{1.12}$$

$$W = \frac{Counts\ in\ AB\ and\ EF}{Total\ counts} \tag{1.13}$$

The *S* Parameter is sensitive to low momentum electrons, ie valence electrons, whereas the *W* parameter is sensitive to high momentum, core electrons. *S* is therefore a useful parameter when looking at vacancy defects where the average electron momentum is lower and W is useful for vacancy impurity complexes where core electrons from neighbouring atoms may be seen by the positrons. This work is concerned with vacancy type defects and therefore it is predominantly the *S* parameter that is measured and used. Changes in the *S* Parameter can be measured to 0.1%. For ion implanted silicon where the predominant defects are divacancies the *S* parameter will increase by up to ~4% with respect to defect free bulk value depending on the concentration of divacancies.

1.6 Determining Defect Concentrations from *S* parameters

Every material consists of a number of available annihilation sites, each of which has a characteristic *S* parameter. If it were possible to make all the positrons annihilate at one type of site the Doppler spectrum would yield a characteristic *S* parameter for each type. Broadly speaking there are three categories of annihilation sites available; undefected bulk, defect sites and surface sites. In a material one would measure the *S* parameters as a function of increasing positron implantation energy, *S(E)*. These *S(E)* measurements would be linear combinations of the characteristic annihilation site *S* parameters, with weightings according to the abundance of each type of site in the region being probed.

For a perfect undefected crystal lattice the *S* parameter for the bulk of the solid is S_{BULK}. Most measurement data is normalised to this value so S_{BULK} =1. However 'perfect' a material the *S* parameter measured at the surface, $S_{SURFACE}$, will differ significantly from the bulk value. This is because of the oxide layer that forms on the surface of many solids when exposed to air. Unless the sample has been

cleaned in a vacuum the value of $S_{SURFACE}$ will be distinct from S_{BULK} as it is largely influenced by oxygen electrons.

Defects have their own characteristic S parameters depending on the species of defect. If there are defect species, i, ii, iii.....they will each have their own characteristic S Parameter; S_{DEFECT_i}, S_{DEFECT_ii}, S_{DEFECT_iii} and so on.

The measured S parameter at each energy is a combination of $S_{SURFACE}$, S_{BULK} and, depending on the number of defect types present, S_{DEFECT_i}, S_{DEFECT_ii}, S_{DEFECT_iii}....weighted by relative fractions of positrons that annihilate at each location. See equation (1.14). Positrons implanted into a material have a Makhovian distribution as covered in §1.3.6. The positron implantation profiles broaden with increasing energy so the region being sampled by the positrons increases with a corresponding loss of resolution. At low implantation energies the positrons will be less spread out but more likely to diffuse to the surface.

$$S_{MEASURED} = F_{SURFACE} S_{SURFACE} + F_{BULK} S_{BULK} + \sum_i S_{DEFECT\_i} F_{DEFECT\_i} \qquad (1.14)$$

If a set of S parameter measurements are made on a sample of undefected material as a function of increasing energy, the resulting $S(E)$ data will take the approximate shape of the line in Figure (1.6(a)). At low energies a large fraction of the incident positrons will diffuse back to the surface and the measured S parameter will be mostly composed of positrons annihilating at surface sites and the resulting measured value will be $S_{SURFACE}$. As the energy is increased, the mean implantation depth increases with $E^{1.6}$ (see equation (1.3)) so an ever decreasing fraction of the positrons will return to the surface. Eventually the positrons will be implanted deep enough into the material that only an insignificant fraction will not annihilate in the bulk of the sample and the measured S parameter will be S_{BULK}. As the diagram shows the measured S takes values between $S_{SURFACE}$ rising steadily to S_{BULK} the fraction annihilating at the surface decreases to zero and the fraction in the bulk increases to one.

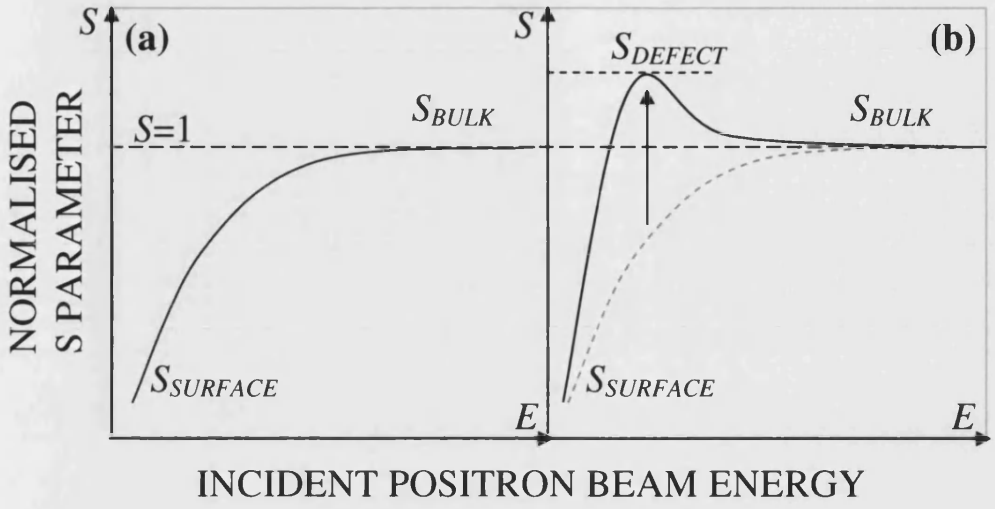

Figure (1.6) Diagrams of normalised *S* parameter measurements *S*(E) for: **(a)** defect free sample with surface *S* parameter $S_{SURFACE}$ **(b)** Sample with layer of defects near the surface with S_{DEFECT} which pulls the measured *S* parameter up above the bulk value (S_{BULK}) in the defected region. This case shows positron saturation trapping by defects, meaning that at some energy all the positrons are trapped by defects and the highest measured value is the S_{DEFECT}., labelled on diagram.

If one species of vacancy type defect with a characteristic *S* parameter that is higher than bulk is introduced into the sample of figure (1.6(a)) in a region close to the surface the resulting *S(E)* measurements will be something like the solid line in figure (1.6(b)). The positrons now have three possible annihilation sites; surface, bulk and defects. The low energy positrons will mostly diffuse back to the surface and the very high energy positrons will be implanted beyond the defected layer. As the energy is increased from low energies a greater fraction of the positrons will annihilate in the defects near the surface with the higher *S* parameter, S_{DEFECT}. This results in the measured *S* parameter being pulled up to a value larger than the bulk. If a series of samples are measured which have ever increasing defect concentration then the highest *S* parameter measured will increase for each sample. If a sample has a high enough concentration of defects, at some energy all the implanted positrons will annihilate at defect sites. This is known as *saturation trapping* and means $S_{MEASURED}$ at this point is effectively a direct measurement of S_{DEFECT}. When saturation trapping occurs the *S* parameter becomes insensitive to further increases in defect concentrations.

1.6.1 VEPFIT

The observable *S* parameters in VEPAS studies are used to obtain depth profiled defect information. The fractions of positrons annihilating at different sites that make up the different components of the measured *S(E)* data depend on the effective diffusion lengths of the positrons, the trapping of the defects present, the positron decay rate in undefected bulk and crucially the concentration of defects per atom $\mathbf{C_D}$.

Extracting defect concentrations as a function of depth from the observable *S(E)* spectrum can be achieved by using a numerical fitting scheme which uses the physics of positron diffusion, models of the defect profile and of course the measured data. One such scheme is a computer package called VEPFIT [1.21] which is specially designed for the fitting of slow positron beam data.

After implantation and thermalisation the positrons diffuse until they annihilate. The diffusion distance depends on the defect concentration, $\mathbf{C_D}$, the positron decay rate in undefected bulk, $\boldsymbol{\lambda}$, and the specific trapping rate for the predominant vacancy type present, $\boldsymbol{\nu}$. The average distance a positron diffuses in a defected material is called its effective diffusion length $\mathbf{L_{eff}}$ and is related to **L**, its average diffusion length in undefected bulk, by equation (1.15) [1.3].

$$L_{eff} = L\left(\frac{\lambda}{\lambda + \nu C_D}\right)^{\frac{1}{2}} \qquad (1.15)$$

For silicon the accepted values of the parameters are: L = 250nm, $\lambda = 4.54 \times 10^9\ s^{-1}$ and ν depends on the defect type; for monovacancies (V_1) in silicon $\nu\_V_1^{Si} = 5 \times 10^{14}\ s^{-1}$ and for divacancies (V_2) in silicon $\nu\_V_2^{Si} = 10^{15}\ s^{-1}$ [1.23]. After diffusion, prior to annihilation, one can imagine an annihilation profile akin to the implantation profile. For a heavily defected material, L_{eff} will be small so it will be similar to the implantation profile but for low defect concentrations or bulk, L_{eff} will be relatively big and the positrons will be able to diffuse some distance before annihilation. In this case the annihilation profile could be quite different from the implantation profile.

VEPFIT solves the diffusion equation (only necessary in one dimension to determine depth profiles) using an initial set of estimated parameters and calculates the annihilation profiles. From this it calculates the *S* parameter that would be measured at each energy, using the same initial parameters it used to solve the diffusion equation. It then compares the fitted data to the actual data and will change the initial parameters until a good fit is achieved. The output of VEPFIT are values of 'desurfaced' *S* parameters and diffusion lengths for each of the different layers as well as the line fitting of the raw data.

It is possible to input different models and fix certain parameters in VEPFIT, depending on the prior knowledge the user has of the samples and the defect profiles. If possible it is beneficial to do so because if VEPFIT has too many free parameters it will output a perfect fit but with unphysical results such as negative *S* parameters.

In the fictional sample of figure (1.6(b)) suppose it is known that the layer of defects near the surface are predominantly of one type which have an *S* parameter, S_{DEFECT}. From the measured data $S_{SURFACE}$ is known and the bulk values would also be known for commonly examined materials like silicon. The model input to VEPFIT would be two layers, one fixed with the bulk values and one with unknown *S* parameter and diffusion length. VEPFIT would then fit the *S* parameter, diffusion length and thickness of the defected layer. From the VEPFIT output it is possible to calculate defect concentrations by two different routes, one using the *S* parameter and one using the effective diffusion length.

1.6.2 Route 1 - C_D from the VEPFIT De-surfaced *S* parameter

For every layer VEPFIT is required to fit, it will output an effective diffusion length and an *S* parameter that has been de-surfaced. The de-surfaced *S* parameter is the *S* parameter of the layer only taking into account the contribution of the positrons that annihilate in it, either at bulk or defect sites. Any contribution from surface positrons has been 'removed' by VEPFIT. The VEPFIT generated *S* parameter for each layer is given by eqn (1.16) but as the relative fractions of bulk and defect must add up to one it can be expressed as eqn.(1.17). In order to avoid

confusion with the fractions of equation (1.14) the de-surfaced relative proportions of defect and bulk annihilations are called P_{DEFECT} and P_{BULK} respectively.

$$S_{LAYER} = P_{DEFECT} S_{DEFECT} + P_{BULK} S_{BULK} \tag{1.16}$$

$$S_{LAYER} = P_{DEFECT} S_{DEFECT} + (1 - P_{DEFECT}) S_{BULK} \tag{1.17}$$

In equation (1.17), the known quantities are:

S_{BULK} This will be well known for the apparatus and previous results. All the data will be normalized to this value so it will be equal to unity.

S_{DEFECT} Known from experience of saturation values. This is assuming a simple case where there is only one type of defect making a significant contribution to the measured *S* parameters

S_{LAYER} This is what VEPFIT will have calculated.

This leaves P_{DEFECT} as the only unknown which can therefore be calculated from the above values.

The relative proportions of P_{DEFECT} and P_{BULK} are given by eqns (1.18) and (1.19)

$$P_{DEFECT} = \frac{\nu C_D}{\nu C_D + \lambda} \tag{1.18}$$

$$P_{BULK} = \frac{\lambda}{\nu C_D + \lambda} \tag{1.19}$$

where, as before, λ = the positron decay rate in undefected bulk, and ν = the specific trapping rate for predominant vacancy type present and C_D = the concentration of defects per atom. It assumed that λ and ν are known from earlier experiments. So using P_{DEFECT} (calculated from VEPFIT fitted *S* parameter values) and equation (1.17) C_D, the concentration of defects per atom is calculated.

1.6.3 Route 2 - C_D from the VEPFIT Diffusion Length

Obtaining the value of C_D from the fitted diffusion length is much more straightforward as it is just simply a matter of using equation (1.15) to calculate C_D. For this route, it is assumed that the diffusion length **L** in undefected bulk is known as well as **λ** and **ν**. For pure silicon the accepted value is ~250nm.

In both cases C_D can be converted into the density of defects by multiplying it by the number of atoms per unit volume.

1.6.4 Self Consistency of VEPFIT

Obviously it is important that whichever values are used from VEPFIT they lead to self consistent results. It is possible to derive a relationship between the S_{LAYER} as given by VEPFIT and L_{eff}. This is done by rearranging equation (1.15) and thereby relating L_{eff} with P_{DEFECT}. See equation (1.20). This is then substituted into eqn (1.17) to eliminate P_{DEFECT} which results in eqn (1.21):

$$\left(\frac{L_{eff}}{L}\right)^2 = \frac{\lambda}{\nu C + \lambda} = P_{bulk} = 1 - P_{defect} \qquad (1.20)$$

$$S_{layer} = \left(1 - \left(\frac{L_{eff}}{L}\right)^2\right) S_{defect} + \left(\frac{L_{eff}}{L}\right)^2 S_{bulk} \qquad (1.21)$$

Now it is possible to plot this relationship using example values. For this example we will use silicon, which for pure undefected bulk has a positron diffusion length of L=250nm. L_{eff} will therefore take values between 0 and 250nm, depending on how defected the particular layer of the silicon is. Assuming that the defects are predominantly divacancies then $S_{DEFECT} = S_{DIVACANCY} = 1.04$. This value would be known for a particular beam/detector set up. Figure (1.7) shows the resulting graph using these values.

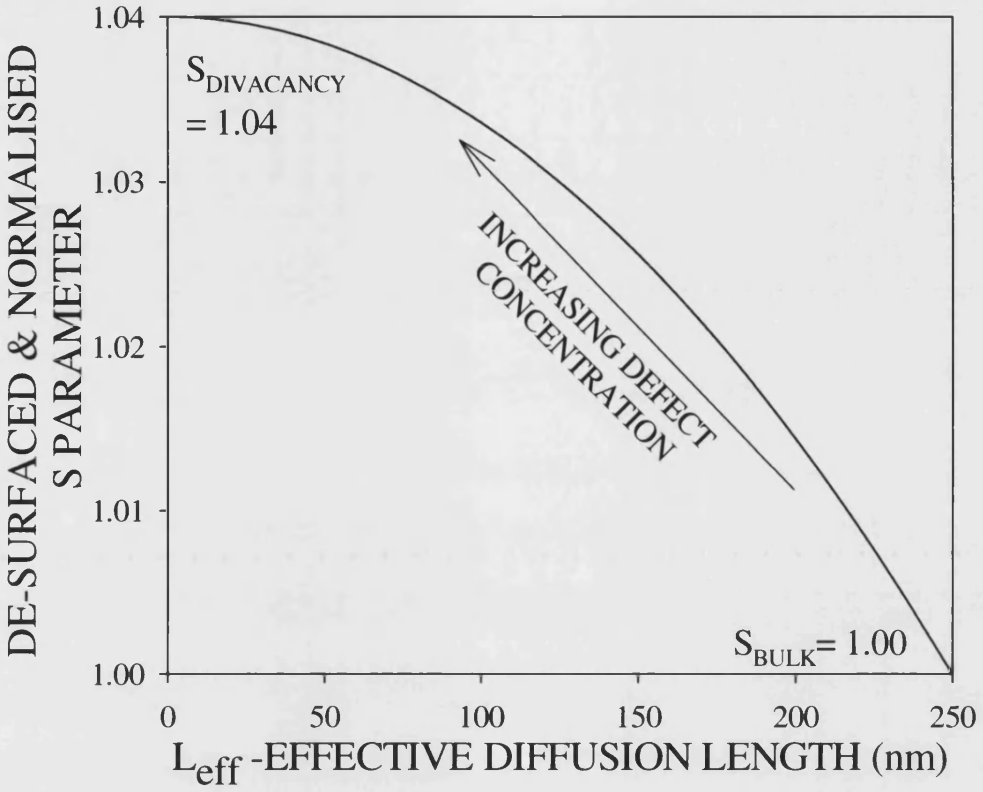

Figure (1.7) The relationship between L_{eff} and S_{LAYER} as given by VEPFIT, using the example of divacancies in silicon, with S_{DEFECT}=$S_{DIVACANCY}$ = 1.04 and L =250nm. All pairs of VEPFIT values of L_{eff} and S_{LAYER} should lie on this line to remain physical.

1.7 Ion Implantation

Ion implantation is a well established technology for doping the semiconductor materials used in the fabrication of microelectronic devices. Doping is the controlled introduction of impurities into a semiconductor in order to manipulate its electronic properties. This is achieved by directing energy and dose controlled beams of ions at wafers of semiconductor. High energy ions bombarding the crystal lattice will inevitably cause radiation damage which will contribute to changes in the semiconductors electronic properties, potentially in a detrimental way. This damage may also inhibit the actual doping process itself. It is therefore of fundamental interest and importance that the formation and behaviour of

defects is understood in as much depth as possible given the widespread application of ion implantation in semiconductor doping.

Positron beam analysis has been proven to be a very sensitive technique to detect small amounts of defects created by ion implantation. Ion induced damage will take the form of Frenkel pairs; interstitials and vacancies. Many of these pairs will dynamically anneal during implantation but some of the vacancies will agglomerate with each other to form higher order vacancies; divacancies trivacancies and so on resulting in much of damage being vacancy type defects. The damaged region caused by ion implantation will usually be located in the first few μm of the surface depending on the mass and energy of the incoming ions. This subsurface region and type of defect are ideal for probing by slow positrons. In the mid eighties Hautojärvi et al [1.24] carried out one of the first studies of ion induced damage with 50keV BF_2. Vacancy type defects were found up to 100nm with mean a depth close to the maximum profiles of the implanted atoms. Since then, the use of positron techniques to study ion induced damage has become routine for such samples.

1.7.1 Ion beams, Doses and Energies

Ion implantation is implemented by ionising the doping material and magnetically and electrostatically accelerating it to strike the sample surface, thereby embedding the dopant into the substrate. The concentration and distribution of damage that is caused depends on the dose, energy, target temperature, atomic masses and any pre-existing impurities in the sample.

Typical ion doses are in the range of 10^{10}-10^{15} ions per cm^2 and beam energies range from 10keV - 0.5 MeV depending on desired application. Higher beam energies are possible but can often cause great structural damage to the target, and because the depth distribution is broad, the net composition change at any point in the target will be small. Lower beam energies result in very little damage. Some common doping ions are arsenic, phosphorus, oxygen and boron and common substrates are silicon and germanium.

As each ion enters the target it loses energy by undergoing a series of elastic and inelastic collisions with the target nuclei and electrons respectively. The damage caused by inelastic collisions is negligible unless the incoming ion has energy in the MeV range. The ions have a random path losing energy as they travel through the lattice. The binding energy of the lattices sites is 10-20 keV so incoming ions knock atoms from their sites leaving vacancies. The dislodged atoms will have gained some energy from the ion so can then also travel through the lattice knocking out other atoms. The particle cascade will stop once the average energy per particle is less than the binding energy. All the knocked out atoms as well as the beam ions will end up as interstitials. After many ions have been implanted the once perfect crystal will end up highly disordered in a region and density corresponding to the ion beam energy dose respectively.

1.7.2 Recombination and Agglomeration of Defects

The distribution of the implanted ions is approximately Gaussian [1.25] and after ion implantation there will be many vacancies and interstitials. Due to the high doses involved it is possible to predict the distributions using Monte Carlo simulations. For example TRIM [1.26] is one such computer program that use Monte Carlo simulations to calculate the initial distributions of vacancies and ions in a material. TRIM allows one to fix the energy and species of the incoming ions and the species of the target. Figure (1.8) shows the distributions of the ions and the vacancies in silicon after the implantation of 4 MeV silicon ions.

An important aspect to bear in mind with TRIM is that does not take into account the subsequent annealing of the vacancies and interstitials. Immediately after implantation many of the interstitials and vacancies will recombine or agglomerate to divacancies or larger clusters. Recombination becomes more significant at higher temperatures. The annealing temperature of monovacancies has been shown to be ~170K [1.27] so at room temperature nearly all monovacancies will have agglomerated with each other or recombined with interstitials. It has been shown that divacancies are the dominant defect type left in ion implanted silicon [1.28] [1.29].

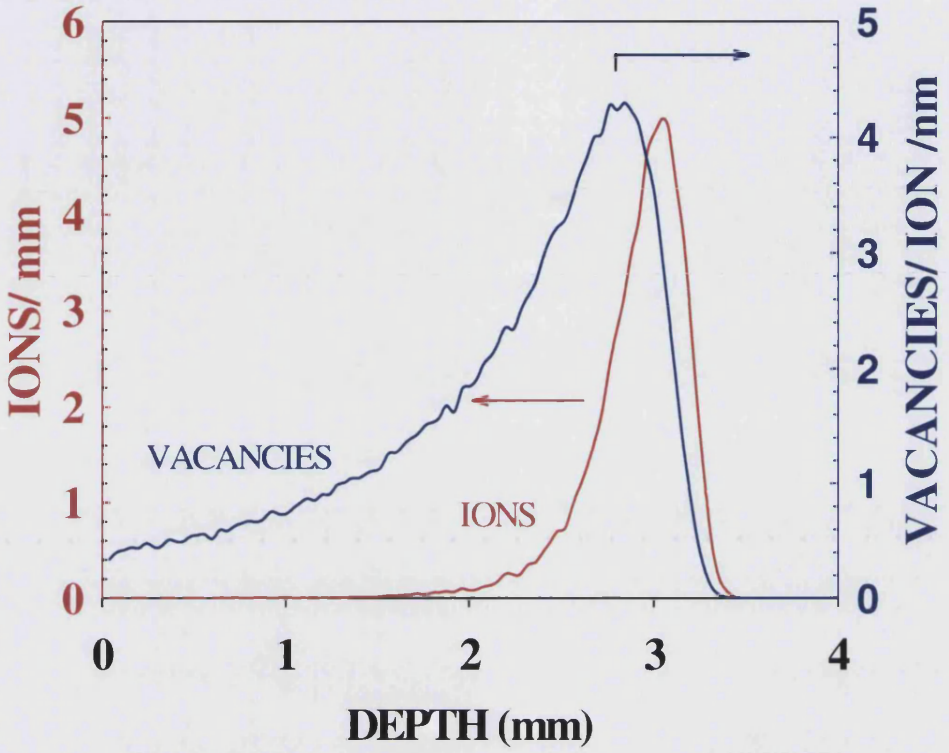

Figure (1.8) TRIM simulations of 4MeV silicon ions implanted into silicon. The blue line is is the distribution of vacancies and the red is the ion distribution.

Due to having an anneal temperature of ~170K monovacancies, unlike divacancies, are not routinely observed in ion implanted samples. In order to study monovacancies it is necessary to perform ion implantation at temperatures <170K and maintain the sample temperature until positron measurements have been taken. The logistics of maintaining a low sample temperature while transferring it from an ion beam implantation system to a positron measurement system, more than likely at a different location, mean that it is preferable to perform the ion implantation *in situ* where the positron measurements are taken. This was attempted using 6 keV helium ions implanted at 60K and is the subject of Chapter 3.

CHAPTER 2

BEAM SET UP AND ANALYSIS OF RAW DATA

2.1 Introduction

The positron beam used was built at the University of East Anglia in 1984 by S M Hutchins et al. [2.1]. In 1998 it moved with the group to the University of Bath and was reassembled over a period of time with numerous modifications. It has been set up to perform slow positron annihilation spectroscopy experiments since October 2002. In the initial runs, a few problems with the system were encountered so a number of modifications and adjustments were made in order to optimise the beam and measurements taken.

The basic principle of the beam system is that a source of fast positrons is moderated to produce slow positrons. These are then accelerated and manipulated with electric and magnetic fields down an evacuated tube and directed at the sample. The positrons then annihilate with electrons in the sample and the annihilation radiation is detected by a germanium detector and a Doppler spectrum collected.

2.2 Production of Slow Positrons

2.2.1 Sources

At the heart of all positron experiments is the need for an adequate intensity of slow positrons. These are obtained by moderating positrons emitted by beta plus decay of radioactive sources such as ^{22}Na, ^{68}Ge, and ^{44}Ti. Each source has different merits depending on activity, half life and cost. A popular choice is the 22 isotope of sodium, ^{22}Na, as it is reasonably priced, has a long half life of 2.6 years, and a high rate of positron emission. The positrons are emitted by β^+ decay simultaneously with an electron neutrino and 3.7 ps later [2.2] the excited state of neon decays emitting a 1.28 MeV gamma photon:

$$^{22}Na \rightarrow {}^{22}Ne^* + e^+ + \nu_e$$

$$^{22}Ne^{*} \rightarrow {}^{22}Ne + \gamma\,(1.28MeV) \qquad (2.1)$$

The 1.28MeV gamma photon emitted 3.7ps after the creation of the positron can be considered to be emitted simultaneously. It is an integral part of positron lifetime studies as it is the 'birth' signal and the annihilation radiation is the 'death' signal. In VEPAS it has no role and it is important that the source is well shielded from the detector so that it does not contribute a background signal to the annihilation radiation spectrum. The energy spectrum of the positrons from beta plus decay is very broad as shown in figure (2.1) and therefore moderation is required in order to produce slow positrons to form a mono-energetic beam.

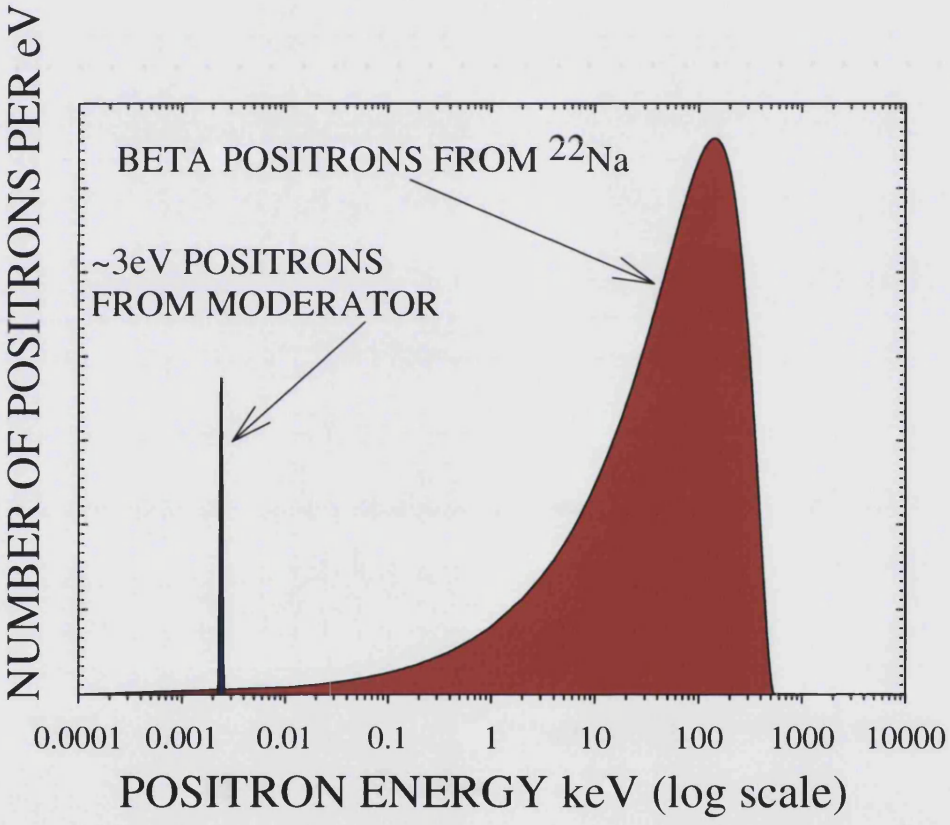

Figure (2.1) The energy spectra of positrons emitted from Na22 (red curve) and the spectra emitted from well annealed tungsten (blue spike).

2.2.2 Work functions and Moderators

As covered in §1.3.2 the work function of a positron is defined in the same way as for an electron; the energy required to move the particle from a point inside a solid to a distant point outside where the surface no longer has any influence. The work function is made up of two parts, a bulk term and a surface term which for positrons acts out of the material. Therefore positron work functions are generally small or in some cases negative resulting in the possibility that positrons originating from within the solid will be emitted into the vacuum with energy equal to the work function of the material.

The efficiency, ε, of a moderator is defined as the number of mono-energetic positrons delivered to the target per unit time divided by the total activity of the primary source [2.3]. Efficiencies are small because only the lower energy β positrons will be stopped within a diffusion length of the surface and the vast majority penetrate to much greater depths and are never re-emitted. Hence the efficiency can be increased if the number of equilibrium defects is minimised so that the effective positron diffusion length is maximised and more of the positrons fall into this category

Tungsten with minimised equilibrium defects by annealing has been shown to have an efficiency of $\sim 10^{-3}$ [2.4] For the best moderator performance the annealing process should be at as high a temperature as possible (>2000°C) and at as low ambient pressure as possible ($<10^{-6}$ Pa). Annealed tungsten is a widely used moderator, not only due to its large positron work function of 2.7 eV but also because ε is not seriously reduced with exposure to air or mono-layers of surface contamination so *in situ* annealing isn't strictly necessary. The geometry is also an important factor in determining moderator efficiencies.

The moderator material and geometry used in this system are multiple layers of fine tungsten mesh which has an efficiency of ~0.03 %. This is geometry is known as quasi–transmission and requires application of a small potential between the source and moderator to ensure the positrons leaving the backside of the moderator are turned away from the source and into the beam line.

2.3 Overview of Positron Beam

Figure (2.2) is a schematic diagram of the system as it is now and all curly bracketed numbers{} in this Chapter refer to it. It is basically an evacuated tube with a positron source at one end, a sample at the other and a series of coils and fields to get positrons of the desired energy from the source to the sample

Positrons are emitted from the source {1} on the LHS of figure (2) On entering the moderator {2} the positrons have a broad spectrum of energies but 0.1% are re-emitted with energies of ~2-3eV

The moderated positron beam travels through the centre of the tube guided by the magnetic field produced by coils {19(a)-(f)}. The velocity filter {5} removes any remaining fast positrons.

The beam is then accelerated to an energy between 0.5keV 30keV depending on the voltage set on the accelerator {8}.

The beam position after this point can be adjusted with two perpendicular coils {11} to guarantee it hits the sample mounted on the sample holder {13(b)}.

The positrons in the beam annihilate with electrons in the sample producing gamma radiation which is measured by the germanium detector {14}.

The beam can be observed visually using a channel-plate detector and phosphor screen {17} and a camera {18}. This is used for setting up experiments and ensuring the sample is in the centre of the beam.

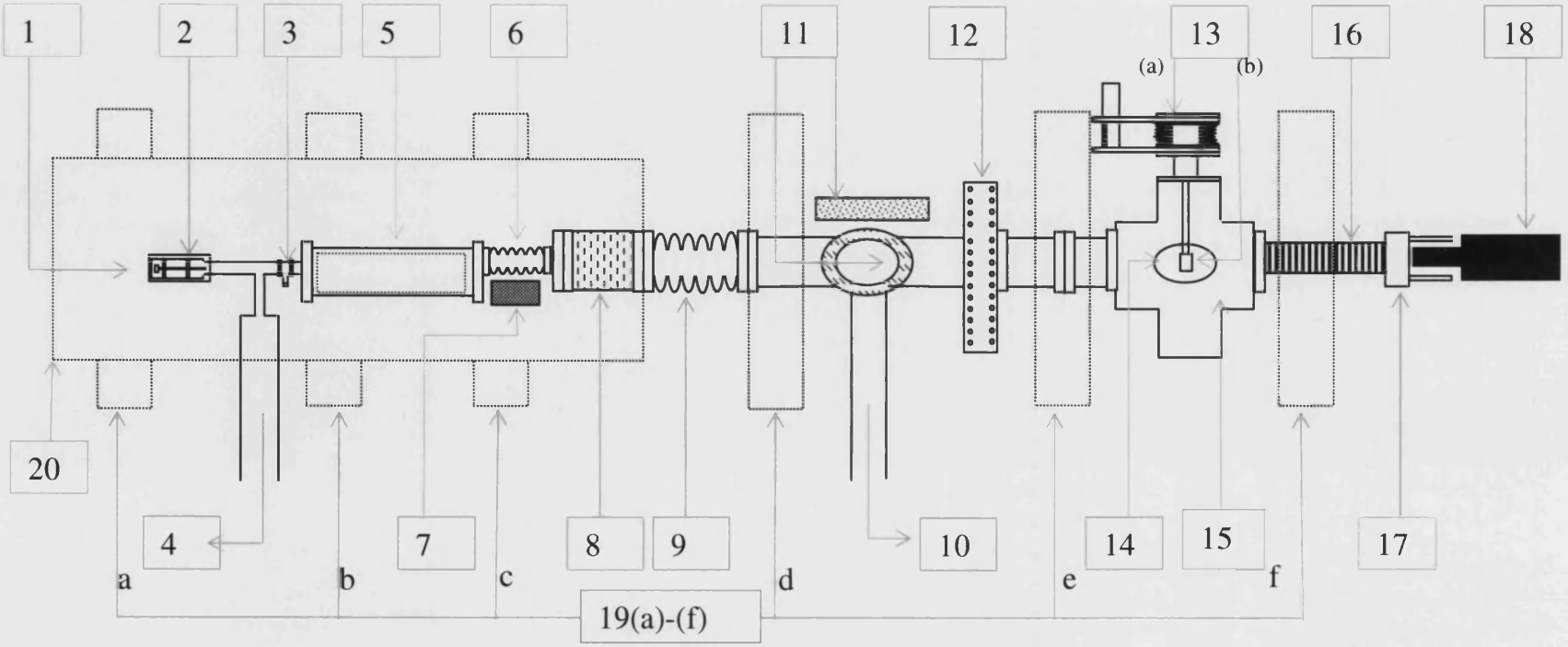

Figure (2.2) Positron Beam System

{1} Source
{2} Moderator
{3} Valve
{4} To ion pump#1
{5} Velocity Filter, *See fig (2.4)*
{6} Small Bellows
{7} Lead block
{8} Ceramic accelerator
{9} Large bellows
10} To ion pump #2
{11} Small Coils to control beam position.
{12} Gate Valve
{13} Travelling sample holder:
{a} moving bellows {b} sample mounting area
{14} Ge gamma detector
{15}Sample chamber
{16}Focussing coil
{17} Channel-plate detector and phosphor screen
{18} Video camera
{19} Guiding coils {a to f}
{20} Protective cage

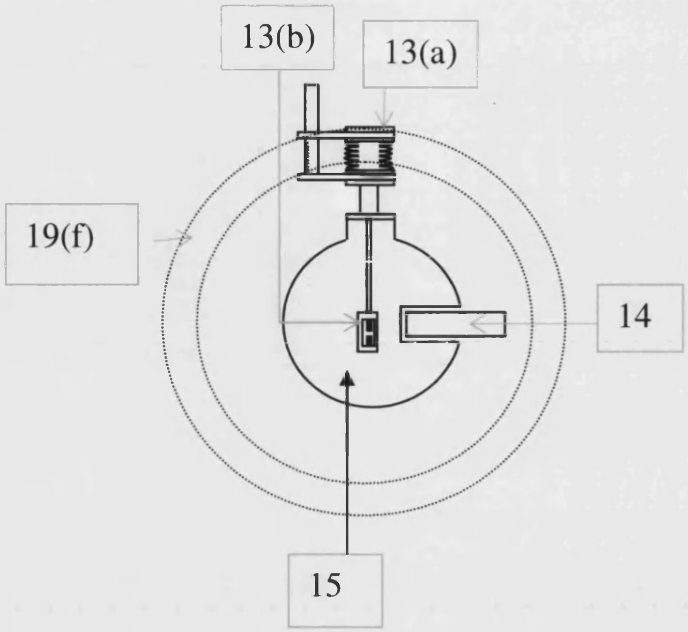

Figure (2.3) End view of Positron Beam Apparatus looking from the sample end towards the source. Numbers refer to same parts as in fig. (2.2):{13a}-Sample mount. {13b}-Moving bellow. {14}-Germanium gamma detector {15}-Sample chamber. {19f}-Guiding coil.

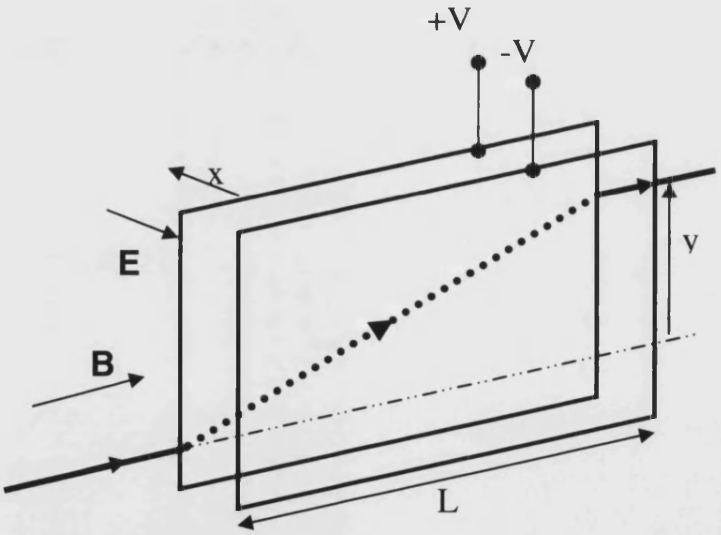

Figure (2.4) Diagram of the velocity filter.{5} in fig. (2.2). On entering the space between the E x B plates the slow positrons are deflected upwards by distance y and exit into the small bellows (Fig. (2.2).{6}) Any fast positrons are deflected only marginally and carry on straight through the filter to be absorbed by a lead block (Fig. (2.2) {7}).

2.4 Detailed Description of Beam Components

2.4.1 The Vacuum

As positrons are anti particles, experiments where the source is any distance away from the sample need to be carried out in vacuum. This is to ensure that they do not scatter or annihilate in air before reaching the sample. The beam apparatus has been designed with the ability to isolate certain sections so they can be kept evacuated while other parts are open to the air.

With reference to fig.(2.2): The section from the source {1} to the gate valve{12} can be isolated and kept evacuated while the RHS is brought up to air. This is used regularly when changing samples. It is also possible to keep the source isolated and evacuated while the rest of the system is at air by closing valve {3}.

2.4.2 Source {1} and Moderator {2}

Positrons leave the source, ^{22}Na with a large spectrum of energies and enter the mesh tungsten moderator. This emits about 0.1% of the positrons at the tungsten positron work function which is 2.7eV. As the source is held at 100V and the moderator at 90V the positrons leaving the moderator have energies of about 92.7eV with respect to the chamber.

2.4.3 Guiding Coils {19(a) –(f)}

There are six coils {19(a)-(f)} each carrying a current of about 4 amps at a voltage of 60V, which provide a magnetic field that guides the positrons through the centre of the system.

2.4.4 Velocity Filter {5}

After leaving the moderator the positrons enter the velocity filter {5}. See fig. (2.4). The velocity filter consists of two parallel plates with an electric field between them. The positrons entering the filter will be deflected by an amount dependent on the time spent between the plates which is dependent on their speed. Slow positrons will spend longer and be deflected by a greater distance whereas

faster positrons will be deflected less. The slow positrons are deflected into the narrow bellows {6} and the fast positrons annihilate in the lead block {7} underneath. The actual plates are curved as the shape of the beam can become deformed as it travels through due to the slightly different electrostatic potentials on each side of the beam. See [2.5] for a more detailed explanation.

2.4.5 Ceramic Accelerator {4}

Next the positrons are accelerated across the ceramic tube {8}. The whole of the source-moderator end of the system is raised to the accelerating potential and the sample environment is at ground. In order to achieve a uniform electric field in the ceramic tube it was made with a helical track on the inside of the accelerator [2.6]. For safety purposes the high voltage end is surrounded by an earthed metal mesh cage {20}.

A disadvantage of such a set up is that the accelerating potential is not perfectly aligned to the guiding magnetic field created by the coils {19(a) –(f)}resulting in an **E** x **B** effect producing transverse forces that deflect the beam. The deflections at the sample depend on the beam energy and unless corrective measures are taken (see §2.4.8), a fraction of the positrons can miss the target. In this beam set up there is no aperture defining the shape of the beam but they are a common feature present in many systems. The result of an aperture defining the beam is that the aperture image will go in and out of focus as the positron energy changes as a result of the positrons going in and out of relative phase with each other. Defocusing and transverse shifts can be minimised by optimising the uniformity and alignment of the accelerating electric and guiding magnetic fields [2.3].

2.4.6 Bellows {8}, Gate Valve {12} and Sample Chamber {15}

Once accelerated the beam of positrons passes through the larger bellows {8}, the open gate valve {12} and through to the sample chamber {15}. The sample is attached to a sample holder {13(b)} the vertical and horizontal position of which can be adjusted with {13(a)}.

2.4.7 Detector {14}

The Ge crystal {14} detects the annihilation radiation. Figure (2.3). shows the view of the sample chamber looking down the beam from the camera {18} end. From this diagram one can see the detector is not actually inside the vacuum system but inserted into a cavity very close to the sample. The Ge detector is cooled to liquid nitrogen temperatures to reduce background signals from thermal noise. It is important that the Ge detector must not touch the sides of the cavity (called a can) and pick up further background signals arising from Earth loops or mechanical vibrations.

2.4.8 Positioning Coils {1}), Focusing {16} and Camera {18}.

In order to take measurements it is important that the positron beam is positioned accurately so that the positrons hit the sample. As covered in §2.4.5 the beam can be deflected by the $\underline{\mathbf{E}}$ x $\underline{\mathbf{B}}$ effect of the accelerating electric field and the guiding magnetic field. Adjustment of the position of the beam is done by adjusting the current in two coils {11} which deflect the beam left –right and up-down.

The beam is observed using the camera {18} which films the channel-plate detector/phosphor screen {17} which the positrons hit after passing through the focusing coil {16}. To position the beam correctly a washer ~4mm across is mounted on the sample holder {13(b)}. Using the camera, the beam is positioned so it intersects with the washer and the sample is then moved to where the washer was. As the transverse forces on the beam are energy dependent, the beam needs to be positioned separately for each accelerating voltage. These settings are saved in a set up file which the computer reads and executes when the experiment runs. See [2.7] for details about the computer controlled system.

2.5 Experimental Set Up

The previous sections detailed the beam system as it is now but it has undergone several major and minor modifications in order to optimise the accuracy and reliability of the data produced. The next sections outline the experimental data that prompted the alterations, details of the modifications and the changes in the data resulting from the work.

2.5.1 Initial Measurements

A set of samples was measured with the system prior to any changes. These were all made from a silicon wafer deposited with a thin film of aluminium on its surface. The samples were produced from the original wafer by altering the annealing temperatures and times. Three of the samples (S1) (S2) and (S3) produced from the Al/Si wafer are used to illustrate the issues with the data. The annealing temperatures and times follow:

(S1) Al/Si-As grown, ie **no anneal.**

(S2) Al/Si -Annealed at **400C for 1 min**

(S3) Al/Si -Annealed at **500C for 1 min**

For each of the three samples the *S* parameter was measured as a function of positron implantation energy using the previous beam set up. The resulting *S(E)* plots are shown in fig. (2.5) exhibited unexpected uneven features. In particular in the *S* values there were consistently two bumps (highlighted in fig. (2.5)), superimposed on the expected gradual descent to the bulk value, at approximately 12keV and 26keV. These anomalies did not diminish through longer experimental running times, ie by collecting more points and increasing the statistical reliability of the results. It was therefore concluded that these features were indicative of a problem with the beam set up and not purely statistical fluctuations.

In order to understand what could be causing the fluctuating *S* parameter measurements at different energies the corresponding count rate for each *S* parameter were examined. For all of the samples this revealed large fluctuations of the count rate from energy to energy. As the count rate drops the *S* parameter goes up and vice versa. These fluctuations correlated with the *S* parameter anomalies as shown for sample (S3) in figure (2.6).

It is known that the resolution of the detector and the resulting *S* parameters are dependent on count rate [2.8]. Achieving a steady count across all energies is an essential first step in correcting any problems with the beam apparatus. The aim was to locate the cause(s) of the fluctuations and stabilise the count rate. If there were still fluctuations in the *S* parameter then at the very least the resolution of the detector could be eliminated as a factor.

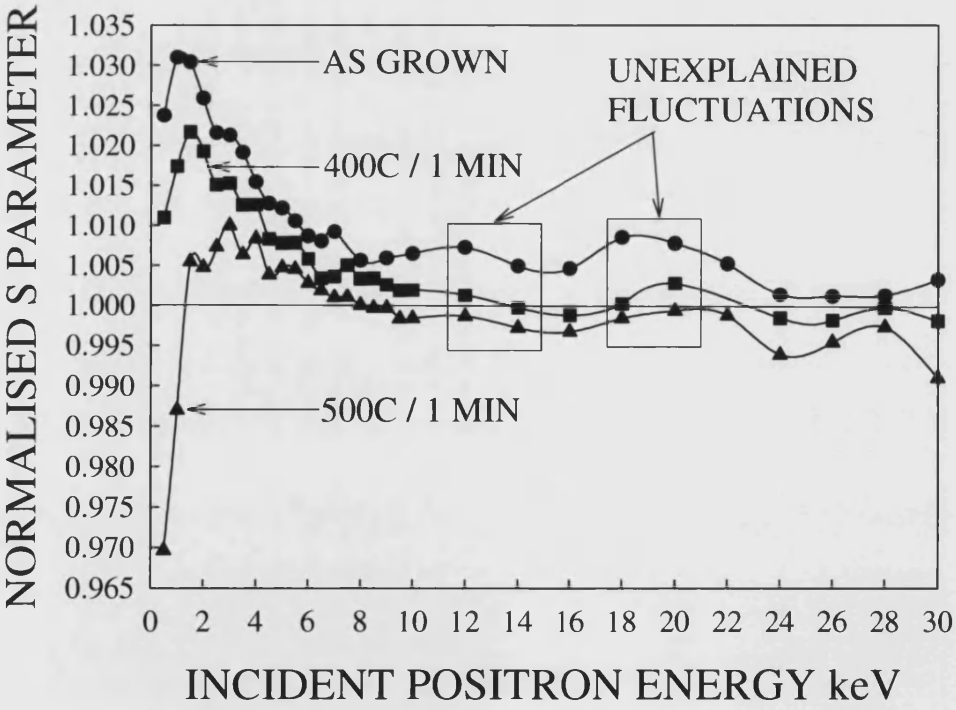

Figure (2.5) Normalised *S(E)* response to three samples of silicon with thin aluminium films on their surfaces.The samples are: **(S1)**-●- As grown **(S2)** -■- 400°C anneal for 1 min **(S3)** -▲- 500 °C anneal for 1 min. The two rectangular boxes highlight the two peaks that appeared in all measurements regardless of the length of time over which the spectrum was collected.

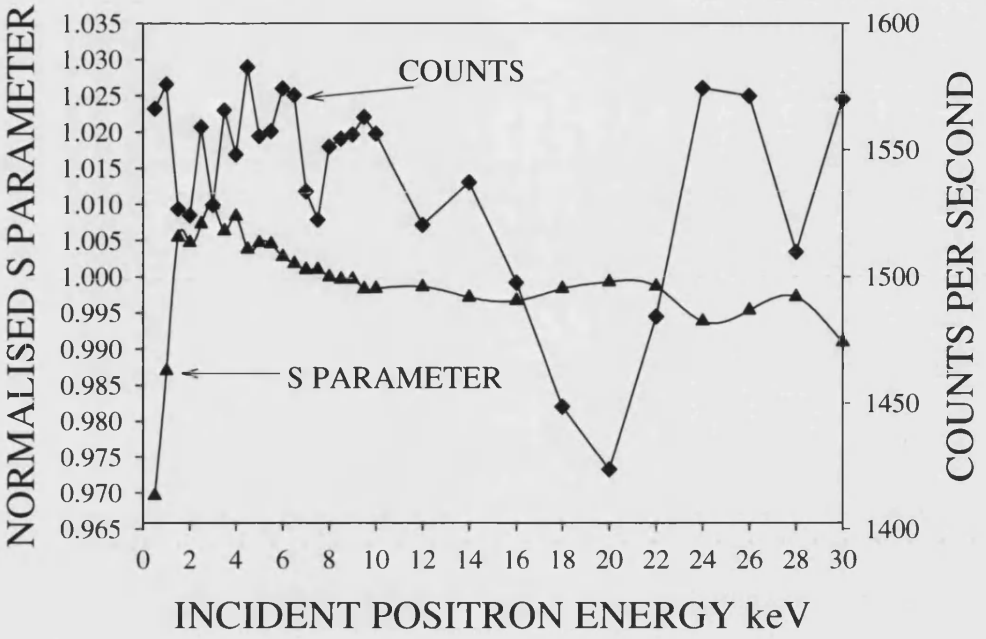

Figure (2.6) *S(E)* response -▲- and count rate variation -◆- with increasing incident positron energy for **(S3)** 500 °C anneal for 1min

2.5.2 Possible Causes of Fluctuations

It was proposed that there could be something obstructing the beam line which a fraction of the positrons were hitting and annihilating in instead of the sample. As mentioned in §2.4.5 the beam position is dependent on the positron energy because of the **E** x **B** effect. This transverse movement of the beam, means that the presence of an obstruction would have a greater or lesser effect as a function of energy. This is consistent with the observed count rate fluctuations with energy. Figure (2.7) is a diagram of the possible fates of positrons in the beam. The influence of an obstruction on the *S* parameter would be as a result of a combination of two things:

(1) The positrons that do not annihilate in the sample may still be detected if they annihilate within sight of the detector. This would alter the measured *S* parameters.

(2) The resolution of the detector is count dependent and large fluctuations would change the resulting *S* Parameter.

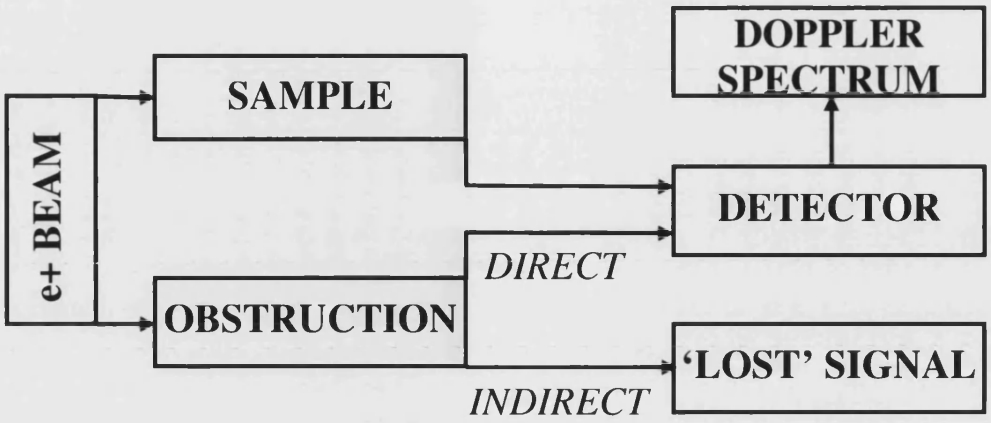

Figure (2.7) A schematic diagram of the possible influence of an obstruction on the Doppler spectrum and resulting *S* parameters. The obstruction could contribute *directly* to the Doppler spectrum and skew the *S* parameter accordingly. Or it could contribute *indirectly* because even if none of the off target positrons annihilate within sight of the detector the lower count rate would alter the detector resolution and the resulting *S* parameter.

2.5.3 System Modifications

Several changes were made to the system in an attempt to try clear the beam line of any obstructions and regulate the beam to be as unperturbed as possible. The modifications are briefly outlined in the following list with reference to fig. (2.2):

(1) Attempt to equalise the currents and voltages in each large coil {19(a) to (f)}, thus making the magnetic field more uniform and reducing the transverse movement of the beam [2.3].

(2) A large coil was added {16} to the sample end of the apparatus enabling the focusing of the beam during beam set up. (Initially the phosphor screen and camera were attached directly to sample chamber). This made the process of setting up the beam position at each energy much easier as the beam was more visible and sharp after focusing.

(3) From previous positron re-emission experiments there were internal deflecting plates located on the RHS of the gate valve. These were removed as they were no longer needed and were so close together that they were candidates for the obstruction to the beam. As they were close to the detector any radiation resulting from positrons annihilating in them may have reached the detector and altered the *S* Parameter.

(4) When the system was open it was noticed that the mesh covering one side of the ceramic accelerator was hanging loose. As this may have been the obstruction it was removed with the intention that if necessary it would be replaced properly at a later date. So far the system is functioning adequately without it.

(5) During all the above changes a longer sample holder was constructed out of stainless steel. This was to allow the maximum number of samples to be loaded and minimise the number of times the system had to be opened up to air to change samples. The maximum distance the travelling sample holder {13(a) and (b)} could move was measured and this was the length of the new sample holder.

2.5.4 Effect of System Modifications on *S(E)* and Count Rates

After the equipment had been modified it was put back together and appropriate beam set up files created. All the samples (S1), (S2) and (S3), were re-measured and all showed significant improvement in both the count rate and *S* parameter values. The two 'undulations' of fig. (2.6) were reduced and the count rate was much smoother although it still oscillated a small amount at higher energies. Figure (2.8) is the previously obtained and new *S* parameter data for the sample (S3) which is the silicon with aluminium film annealed for one minute at 500°C. Figure (2.9) is the count rate data for the same sample (S3)

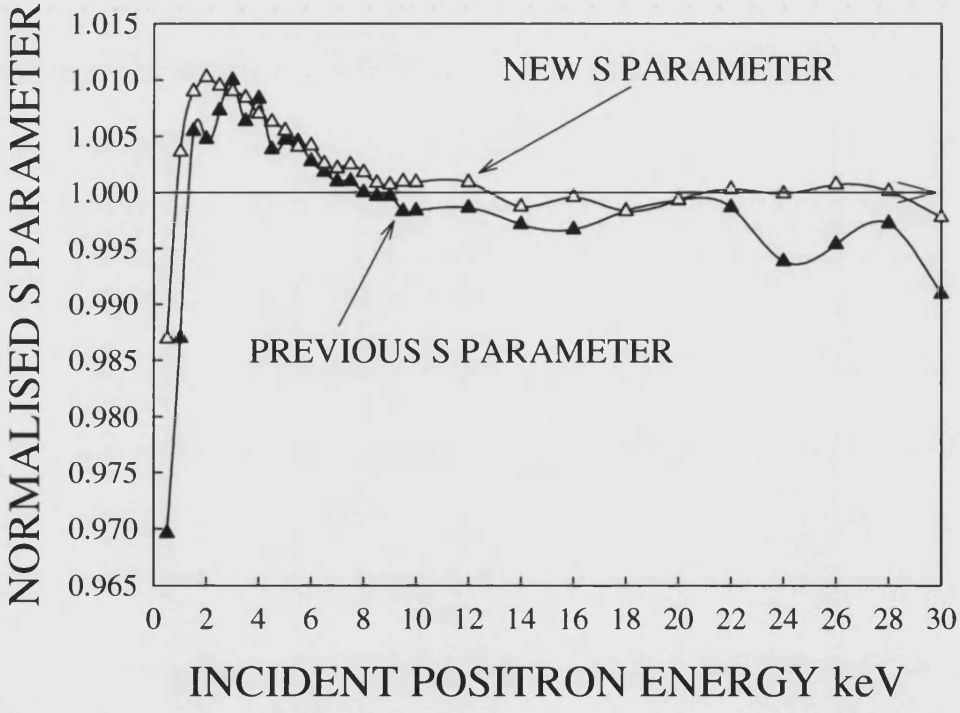

Figure (2.8) Normalised *S(E)* response to (S3)-silicon with aluminium film annealed for 1 min at 500°C. The two lines are from before -▲- and after-△- system modifications.

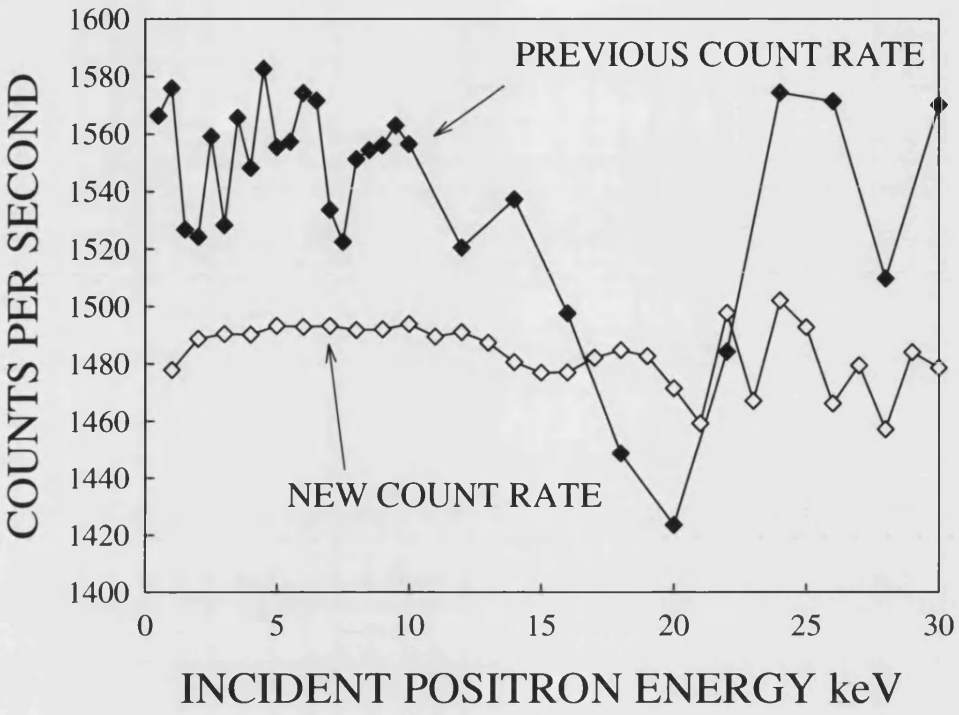

Figure (2.9) Variation of count rate with incident positron energy for (S3) silicon with aluminium film annealed for 1 min at 500°C. The two lines are from before -◆- and after -◇- system modifications.

2.6 Normalisation of Count Rate

With the changes in the experimental set up a significant stabilisation of the count rate variation with energy was achieved. The intensity of the positron beam will always change with energy [2.8] so an entirely flat count rate could not be achieved by this method. However it is possible to normalise the *S* parameter results to one count rate. This was done in an attempt to create smooth *S* reliable parameter results. This count normalisation procedure should not be confused with normalising the *S* parameter to the bulk value S_{BULK}. All the results are already S_{BULK} normalised and this is count rate normalisation.

2.6.1 Method and Results

As covered previously, the resolution of the detector and therefore the measured *S* parameter depends upon the count rate, i.e. the number of signals received by the detector per unit time. It was assumed that over small count rate variations a linear relationship existed between count rate and *S* Parameter. This assumption seemed reasonable after the beam was positioned on the sample at three different points relative to the detector. See fig (2.10). *S* parameter measurements were taken for each position at several different energies from 12keV to 22keV.

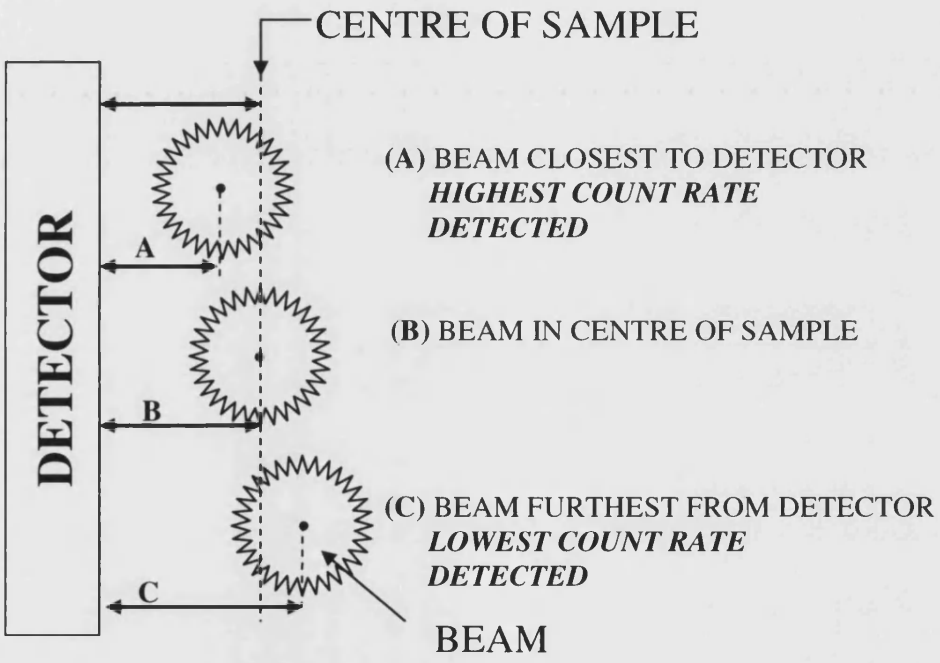

Figure (2.10) Diagram showing three different positions A B and C of the beam relative to the detector in order to alter the number of counts accumulated and hence corresponding *S* Parameters. The highest count rate is achieved with the beam in position A and least when in position C. The sample position is fixed and marked by the dotted line.

The further away the beam was from the detector the lower the count rate as fewer gamma photons were able to hit the detector. This was in line with expectation. The count rate and *S* parameter are plotted in fig (2.11) for the three different positions at energies 12keV, 14keV 18keV and 20keV. As one can see from fig. (2.11) a linear relationship is a reasonable assumption (over this level of fluctuation) so straight lines were fitted for each energy using least squares method. A weighted average of the gradients obtained was calculated using the R^2 of fit as the weighting factor.

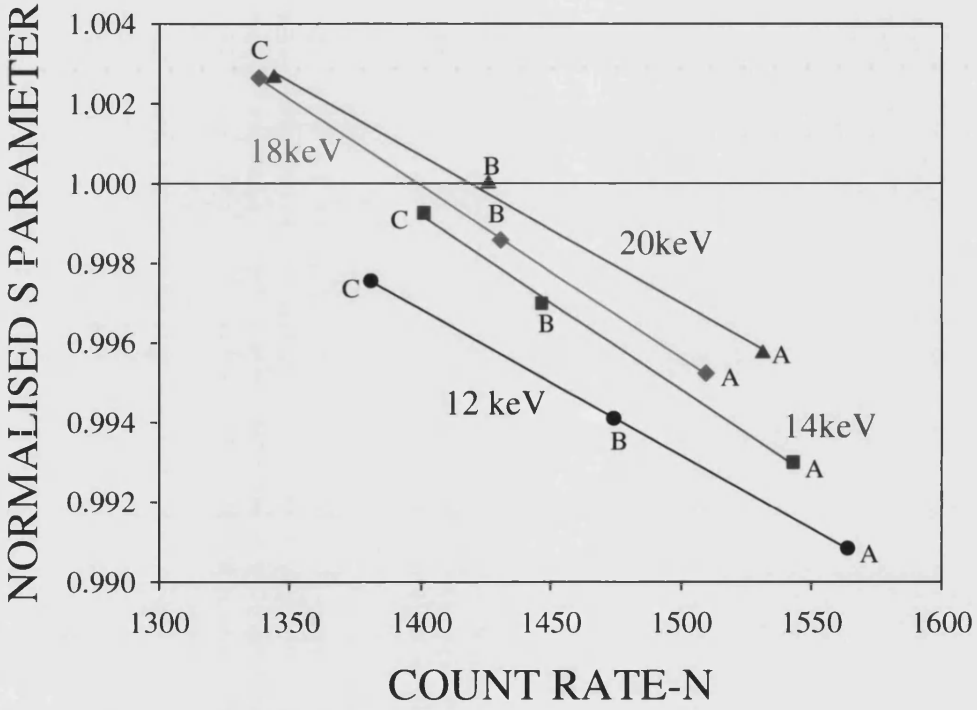

Figure (2.11) The variation of *S* parameter with count rate for a reference sample. For each energy the *S* parameter was measured in 3 different positions (A) (B) and (C) relative to the detector.

If N is the Count rate and *S* the *S* parameter then the weighted average gradient was calculated to be:

$$\frac{dS}{dN} = -3.97 x 10^{-5} \qquad (2.2)$$

For a given set of data a normalising count rate N_{NORM} is decided on and *for each energy* the difference between that and the actual count rate, N_{ACTUAL} is defined to be *dN* as in equation (2.3).

$$dN = N_{ACTUAL} - N_{NORM} \tag{2.3}$$

Likewise dS is defined as:

$$dS = S_{ACTUAL} - S_{NORM} \tag{2.4}$$

Using equations (2.2) and (2.3) *dS* is calculated and used to calculate S_{NORM} from eqn (2.4). The normalising count rate N_{NORM} was chosen by averaging the count rate over a particularly smooth part of the count spectrum.

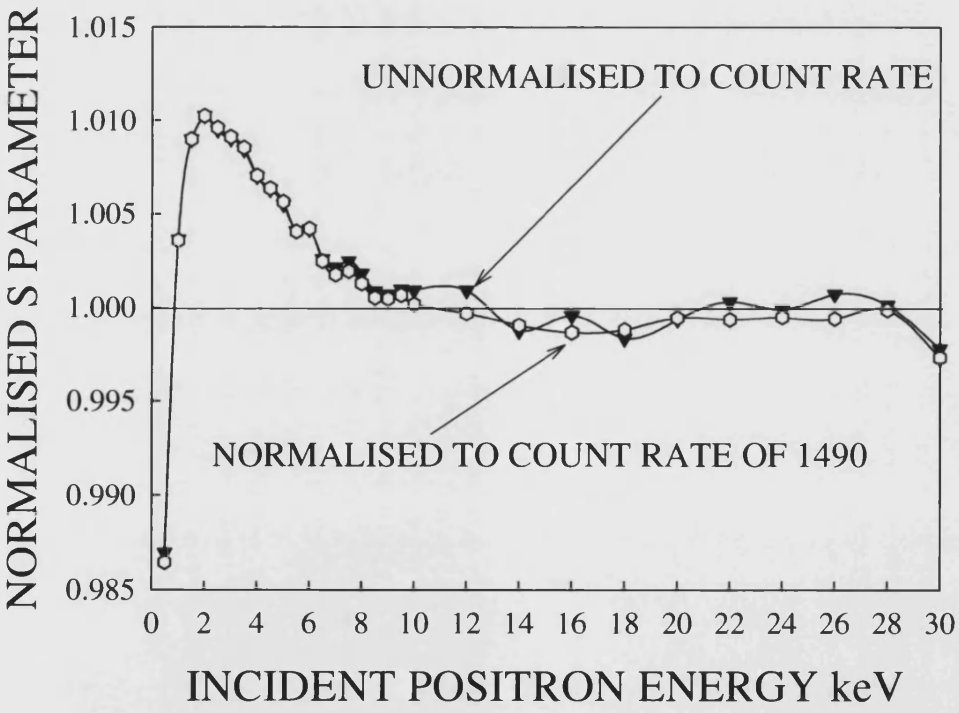

Figure (2.12) *S(E)* response of S3 (Al/Si -500°C, 1 min). As measured *S* parameter -▼- and count normalised *S* Parameter -○ -,

Figure (2.12) shows the results of the count normalising *S* parameter data from (S3) -silicon with aluminium film, annealed for 1min at 500°C. The results were count normalised to N=1490 as this was the average count rate from 0.5keV to 6keV. Over this range there was a particularly steady count rate in the original data. See fig (2.9). While the spectrum is certainly smoother after applying this method it was nevertheless concluded that the slight improvement was not worth the added stage of analysis and labour involved.

2.7 Example Analysis of Silicon Implanted with Oxygen

In §1.5.2, the use of *S* and W Parameters to characterise the width and shape of the annihilation line is described. This section is concerned solely with *S* Parameters and their use in the analysis of defects in solids. The samples used in the following analysis are silicon wafers implanted with 400keV oxygen ions at varying doses. As the behaviour of oxygen implanted silicon is well known the samples were originally to be used as a means of calibrating results obtained from this positron beam setup with another beam.

The *S(E)* data for these samples was first obtained in October 2002. However as more data was accumulated it became apparent that there were problems with the beam evidenced by the unreliable data. Addressing these issues with the beam took place and is the subject of §2.5. Hence the following data sets are used to demonstrate the analysis procedure and highlight potential problems with the fitting program used but are not the best examples of *S* Parameter data of oxygen implanted silicon.

Normalised *S(E)* data for the oxygen implanted silicon is presented here and the fitting model described. The data was fitted using VEPFIT [2.9] and the outputs of this are used to calculate defect concentrations for two of the samples using both the methods described in §1.6.2 and §1.6.3. Finally after a brief investigation the limitations of VEPFIT are presented and discussed.

2.7.1 Preparation of Samples

The samples were created at the Ion Beam Centre at the University of Surrey; 400keV oxygen ions at doses varying from $1x10^{10}$ to $1x10^{13}$ ions cm^{-2} (ions per square centimetre) were implanted into silicon. There is greater detail on ion implantation in §1.7. A brief summary follows; on implantation the implanted ions (in this case oxygen) undergo a series of collisions losing energy and dislodging the target (silicon) atoms from the lattice sites, thus creating many vacancy and interstitial pairs. Most of the vacancies and interstitials recombine during the ion implantation but some of the vacancies will combine with other vacancies to form divacancies, which are stable at room temperature and are the predominant defect type in this case [2.10] [2.11]. The number of divacancies present will increase as the dose increases, which will result in greater numbers of positrons being trapped and therefore a larger *S* parameter. However the depth of the damage is dependent on the incident energy of the oxygen ions and so will be roughly constant for all doses.

2.7.2 *S(E)* Response to Increasing Dose

For each of the samples the *S* parameter was measured as a function of energy. The normalised *S(E)* data for the different ion doses is shown in figure (2.7) along with an oxygen free, virgin sample. The results have all been normalised so S_{BULK} = 1. The *S* Parameter increases near the surface due to the higher number of divacancies in this region.

For each energy the measured *S* Parameter is a linear combination of contributions from the surface, bulk and defects; $S_{SURFACE}$, S_{BULK} and S_{DEFECT} respectively. The relative weighting depends on the fractions of positrons that annihilate at each site. See equation (1.14) from Chapter 1.

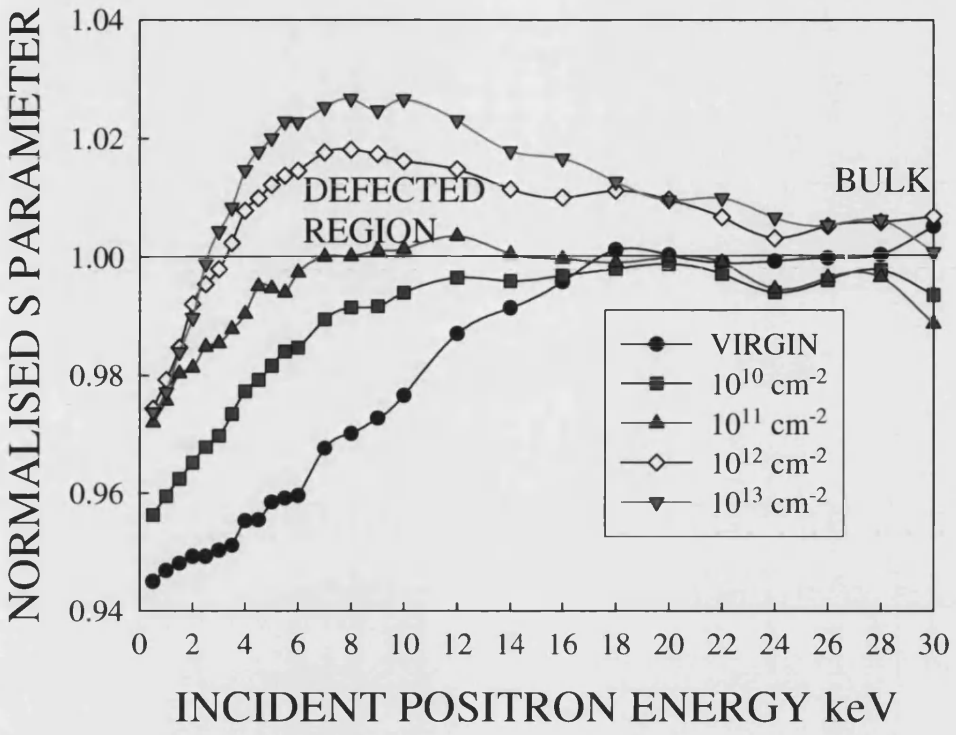

Figure (2.13) Normalised *S* Parameter –Energy plot of virgin silicon and silicon implanted with 400keV oxygen at doses from $1x10^{10}$ions/cm^2 to $1x10^{13}$ ions/cm^2.

If the concentration of damage is sufficiently high, saturation trapping will occur. That is, all the positrons annihilate at defect sites and the *S* parameter becomes insensitive to further increases in defect concentration. When saturation occurs the highest *S* parameter measured is a direct measurement of the defect *S* Parameter S_{DEFECT}. It is known that for a 400 keV dose of $1x10^{13}$cm^{-2} oxygen ions the defect concentration is not quite high enough for saturation. With this beam it was known that the saturation value is actually ~1.036 and that the defects are predominantly divacancies so $S_{DIVACANCY}$ = 1.036. This value can be used to calculate defect concentrations in non saturated samples.

2.7.3 Model and Analysis

The *S* -parameters in two of the samples with ion doses of $1x10^{11}$ cm^{-2} and $1x10^{12}cm^{-2}$ were fitted with VEPFIT. A two layer model was used to describe the damage and is pictured in figure (2.14). Layer 1 is a defected region which extends from the surface to depth, D. Using an Monte Carlo simulation program that models ion implantation damage TRIM [2.12], D was found to be 720nm which is used in the model. The *S* Parameter and diffusion length of Layer 1 are both to be fitted by VEPFIT.

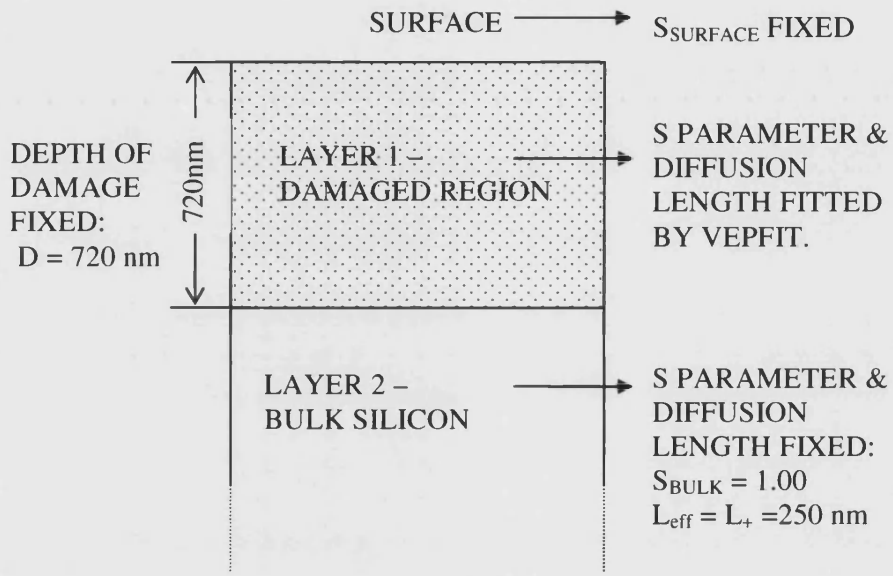

Figure (2.14) Diagram of model used to fit Parameters in VEPFIT. Two layers; one defected from surface to depth D at 720nm and one bulk. The bulk layer has values S_{bulk} =1 and L_{eff} =250nm which are fixed. $S_{SURFACE}$ is fixed from the data and $L_{eff\_Layer\_1}$ and $S_{DEFECTED}$ are both fitted by VEPFIT

The second layer, Layer 2, is the remaining bulk of the sample and has the properties of virgin silicon, S_{BULK} =1 and L_{eff} =250nm which are both fixed. The *S* parameters at the surfaces of each sample were obtained from the data and fixed.

To obtain the concentration of defects from VEPFIT there are two routes which are described in §1.6.2 and §1.6.3. The principle equations; (1.17) and (1.18) from 'Route 1' (§1.6.2) are reproduced below. (λ is the positron decay rate in defect free material ; for silicon $\lambda = 4.54 \times 10^9\ s^{-1}$ and υ is the defect trapping rate which for divacancies in silicon $\upsilon = 1 \times 10^{15}\ s^{-1}$).

$$S_{LAYER} = P_{DEFECT} S_{DEFECT} + (1 - P_{DEFECT}) S_{BULK} \tag{1.17}$$

$$P_{DEEFCT} = \frac{\nu C_D}{\nu C_D + \lambda} \tag{1.18}$$

By rearranging equation (1.17) and substituting S_{BULK} =1 we get:

$$P_{DEFECT} = \frac{S_{LAYER} - 1}{S_{DEFECT} - 1} \tag{2.5}$$

Then by incorporating equation (2.5) into (1.18) we obtain a single expression for the concentration of defects per atom, C_{R1} via 'route 1'. Input values are the 'desurfaced' S_{LAYER} from VEPFIT and the S parameter of the particular defect type which can be obtained from saturation of heavily defected samples:

$$C_{D\_R1} = \frac{\lambda}{\nu}\left(\frac{(S_{LAYER} - 1)}{(S_{DEFECT} - S_{LAYER})}\right) \tag{2.6}$$

From 'route 2' ((§1.6.3) the primary equation is (1.15)

$$L_{eff} = L\left(\frac{\lambda}{\lambda + \nu C_D}\right)^{\frac{1}{2}} \tag{1.15}$$

This is rearranged to form a single expression for the concentration of defects per atom, C_{D_R2} via 'route 2' The input required is the effective diffusion length L_{eff} in a region given by VEPFIT:

$$C_{D\_R2} = \frac{\lambda}{\nu}\left(\left(\frac{L}{L_{eff}}\right)^2 - 1\right) \qquad (2.7)$$

2.7.4 Fitting Results.

The VEPFIT generated fits for the two samples are shown in figure (2.15) and the fitted values of the *S* parameters and diffusion lengths in the top layers are shown in table (2.1) with the corresponding defect concentrations.

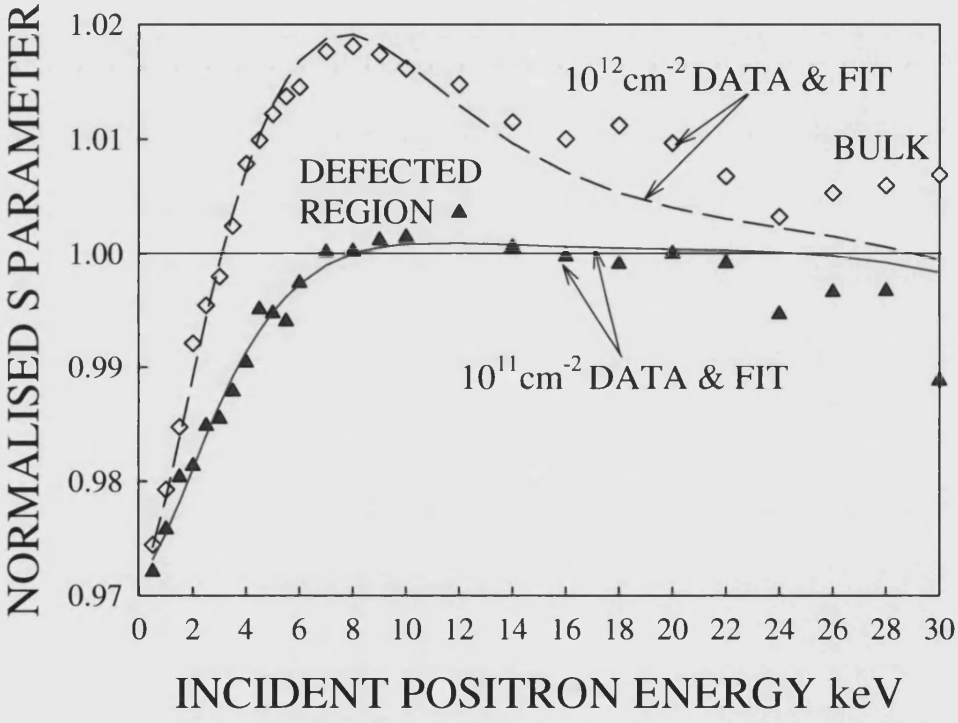

Figure (2.15) Data and VEPFIT fits of *S* parameter for oxygen doses of: 10^{11} ions cm^{-2} (data ▲, fit —) and 10^{12} ions cm^{-2} (data ◇, fit —) **(S3):** 500 °C anneal for 1 min

The raw data is badly scattered at higher incident positron energies which has resulted in VEPFIT fitting sloped lines. The reality is that at energies above 20keV there is only bulk silicon with a uniform *S* parameter and the fitted line should tend to the *S* =1 line and not go below it.

.

Sample	FIXED	S_{layer} **Fitted**	Layer L_{eff} **Fitted**	C_D-defects/atom	
				From fitted *S* parameter (Route 1)	From fitted L_{eff} (Route 2)
O in Si dose $1x10^{11}$ ions cm^{-2}	$S_{surface}$ = 0.972 S_{Bulk} = 1.000 Bulk L_{eff} =250nm	1.004	135nm	$5.68 x10^{-7}$	$1.10 x10^{-5}$
O in Si dose $1x10^{12}$ ions cm^{-2}		1.027	123nm	$1.36 x10^{-5}$	$1.42 x10^{-5}$

Table (2.1) Fitted VEPFIT parameters and calculated defect concentrations for oxygen implanted silicon.

The data in table (2.1) is the output values for *S* and Leff from VEPFIT and the calculated defect concentrations for each sample using both *S* (route 1) and L_{eff} (route 2) as starting points. Neither of the fitted pairs of values are consistent with each other (see fig.(1.7)) and as a result two different defect concentrations have been calculated for each sample. The inconsistency is most likely as a consequence of a combination of the erratic data and VEPFIT's limitations which are discussed in the next section.

The values of the surface *S* parameters of the raw data are quite low (due to an oxide layer) and drag down the average *S* parameter of the defected region. This isn't so important for the higher dose sample ($1x10^{12}$ ions.cm^{-2}) as the concentration of defects is still high enough to pull the *S* parameter up to a peak above the bulk in the damaged region. This means that the fitted *S* and L_{eff} are both physically realistic and result in values of C_D that are plausible and actually quite close to each other.

For the lower dose sample this isn't the case and as a result VEPFIT has fitted it as though it was virgin bulk silicon with a slightly shorter diffusion length; 135nm opposed to 250nm. The value of C_{D_R1} resulting from *S*, is so low, $\sim 10^{-7}$ defects/atom, it is virtually defect free but this is misleading. In this case the C_{D_R2} obtained from the L_{eff} is a more realistic value for C being the correct order of magnitude $\sim 10^{-5}$. Neither of these results are particularly useful in understanding the defect profile present. Given the dominating effect of the low surface *S*,

etching off the oxide surface would have yielded better raw data to analyse. Another factor is that with 'good' data one would expect all the samples to have a similar bulk value but this data had differences in the bulk value of up to ~0.015. This uncertainty in the bulk value would have affected all the results to some extent.

2.7.5 Limitations of VEPFIT

Measured data is input to VEPFIT along with parameters which are either fixed or fitted as desired according to knowledge of the substances, defects and model in use. VEPFIT solves the diffusion equation (using the fixed input parameters and the initial guesses for the parameters to be fitted) and calculates how far implanted positrons at each energy diffuse, thereby calculating the fraction of positrons at each depth prior to annihilation. This is called the annihilation profile from which VEPFIT calculates the S parameters that would be measured. These are compared to the actual S parameter data and the fitted parameters adjusted until a good fit is achieved.

For VEPFIT to work well it needs to have as many parameters fixed as possible, for example, the number of layers, the diffusion lengths within those layers, the S parameter of the bulk and so on. For each fitted layer VEPFIT will output a de-surfaced S parameter and the diffusion length. From these values C_D the number of defects per atom is calculated by one of two routes which are described in §1.6.2 and §1.6.3

The initial guesses can affect the output values, different values producing different and sometimes unphysical results. This problem can be overcome by having initial guesses as close to the 'actual' values as possible. This can be achieved by running VEPFIT a few times and using the first output values simply to obtain realistic input values. In a brief investigation it was found that initial guesses of S parameters at surfaces or layers could vary widely and VEPFIT consistently fitted the same values. However the initial guesses of the diffusion length altered both the fitted diffusion lengths and S parameters. Hence, it was important to be aware of this and a range of values for each fitting parameter

before accepting the results. Figure(2.14) is a demonstration of the effect of the initial diffusion length guesses on the VEPFIT outputs for a sample of silicon with a thin layer of aluminium deposited on its surface. The sample structure was modelled as two layers, with the upper surface of aluminium having fixed parameters of S = 1.004 and L_{eff} = 90nm (these were known from other similar samples and analysis) and the silicon (bulk) having its parameters fitted. VEPFIT was run repeatedly with different initial guesses of diffusion length at 5nm intervals from 5nm to 400nm. The resulting fitted S parameter and diffusions lengths are plotted in figure (2.14)

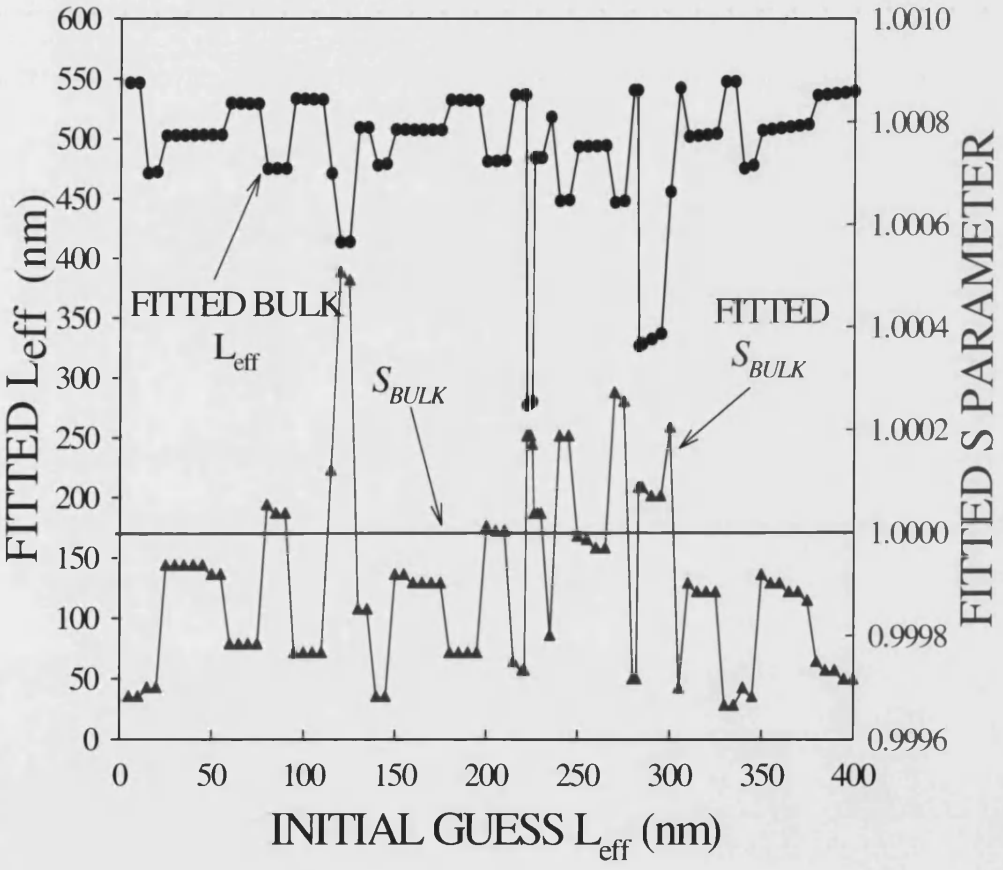

Figure (2.14) Fitting results for a sample of silicon deposited with a thin layer of aluminium. The aluminium parameters were fixed: S=1.004 and L_{eff} = 90nm. The silicon (bulk) parameters were fitted; S_{BULK} -▲- and diffusion length -●- using different starting values of diffusion length.

In the example of figure (2.16) it is apparent that VEPFIT is fairly poor at producing accurate diffusion lengths simultaneously with *S* parameters. Where accurate *S* parameters are fitted (initial L_{eff} guesses of ~80nm, ~210nm, ~250nm) the corresponding diffusion lengths are all much higher than the generally accepted 250nm value. The converse is also true, however the fitted diffusion length is even less frequently a physically realistic value. Additionally none of these pairs of values lie on the (equivalent) line of figure (1.7); the arrangement is appears to be fairly random. One can only conclude that fitted parameters generated by VEPFIT need to be treated with caution and used as general guide to the physical system and not taken at face value without thought and judgment as to how realistic they actually are.

CHAPTER 3

LOW TEMPERATURE ION IMPLANTATION OF SILICON

3.1 Introduction

The use of positron beam-based Doppler broadening spectroscopy has been applied to the study of ion implanted semiconductors routinely [3.1] [3.2] since the first successful results in the mid eighties [3.3]. During ion implantation of silicon, monovacancies are formed in abundant quantities and their distribution can be simulated by the widely used code TRIM [3.4]. However, as monovacancies in silicon anneal at ~170K [3.5], too few survive to be observed with conventional positron techniques because ion implantation and/or positron beam measurements are usually performed at room temperature. The monovacancies recombine or agglomerate into small vacancy clusters - principally divacancies [3.6]. Further, especially in Cz Si, these divacancies can form complexes with oxygen [3.7].

Polity et al. performed positron lifetime measurements on electron-implanted silicon and other semiconductors at low temperatures and studied the evolution of monovacancies with sample temperature [3.8]. To the authors' knowledge, however, no direct measurements of monovacancies produced in ion implantation have yet been attempted.

In order to study monovacancies formed during the implantation process it is thus necessary to (a) implant at low temperatures (i.e., significantly below 170K) and (b) maintain the low sample temperature before and during positron measurements. To achieve this one could add a positron beam spectrometer and cooling mechanism to an existing ion beam implanter or the other way round - the addition of an ion implanter and cooling facilities to a positron beam. This latter course was pursued and it allowed *in situ* positron measurements of ion implanted samples at low temperatures.

This work was first published in [3.9]. First measurements which were using a voltage of 6kV and helium gas at post implant temperatures of 60K to 300K are presented with a discussion of the benefits and drawbacks of this system. In addition is a brief description of at some of the results obtained since this work was carried out.

3.2 Detecting Monovacancy Damage

The positron beam at Bath (described in Chapter 2 and reference [3.10]) was set up for taking measurements at low temperatures by replacing the sample holder with a cold finger made of copper attached to the expander head of closed cycle helium refrigeration unit. Damage was introduced by ion implantation which was accomplished by holding the sample at a high negative potential and bleeding a small amount of gas into the sample chamber, the idea being that the gas would ionise and discharge into the sample knocking out silicon atoms creating vacancy damage.

The high voltage was set at 6keV and helium gas was bled into the sample chamber. The damage distribution that this would cause was simulated using TRIM [3.4] (see figure (3.1)). Usually TRIM profiles are of limited use because the actual vacancy damage profile would differ from the simulated one due to subsequent migration, agglomeration and recombination of defects. However in this case the damage should remain pretty much as in figure (3.1) because the low temperature 'freezes' in this damage. Figure (3.1) shows a peak of vacancy damage at ~50nm which would be detectable with positrons in the 2-3 keV energy range as these have a mean implantation depths of 50-100nm.

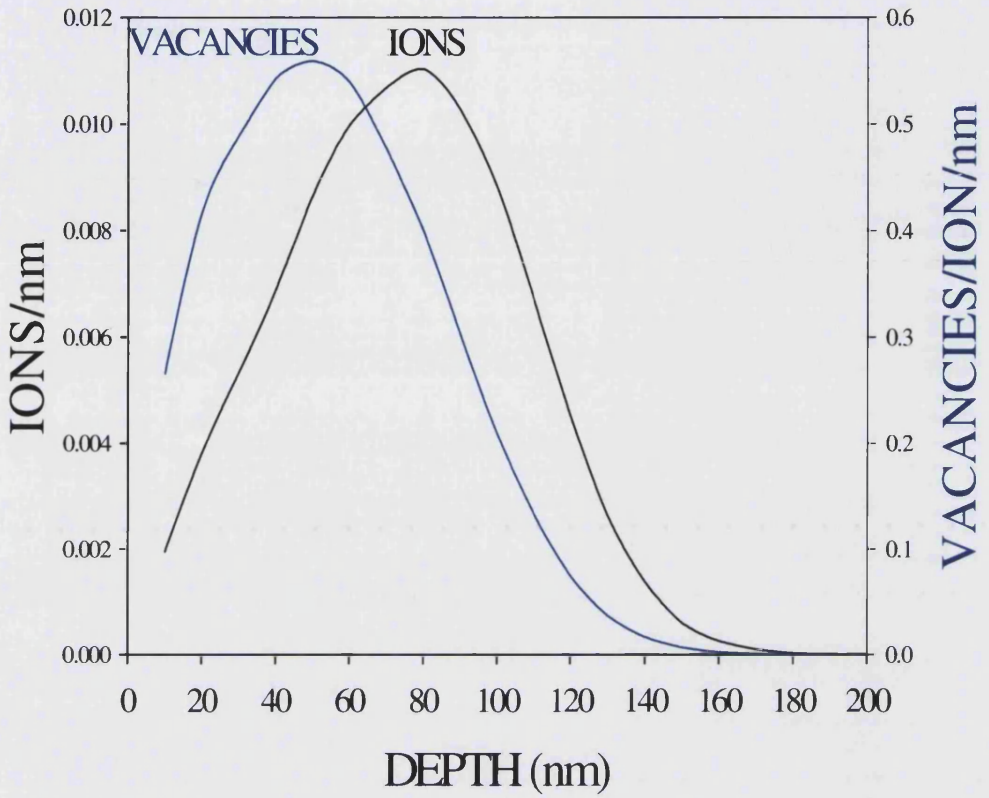

Figure (3.1) TRIM simulation of vacancy and ion distributions created by helium ions implanted into silicon at 6keV. For every ion approximately 45 vacancies are created.

The discrimination of monovacancies and divacancies by Doppler broadening spectroscopy is, in principle, straightforward; the widely-used lineshape parameter *S* (defined and discussed in Chapter 1) characteristic of positron annihilation in monovacancies is about 2.5% higher than that for perfect silicon, whereas its value for annihilation in divacancies is about 4% higher. This figure of 2.5 % has never been directly measured but is a reasonable estimate based on previous experience of divacancies and larger agglomerations by extrapolating down. The difference between divacancies and monovacancies should be easily measurable if the material has a high enough concentration of either defect type to cause saturation trapping - that is, that all the positrons implanted into the defects region annihilate at defect sites and the defect *S* parameter is measured directly.

However, in the case of non-saturation trapping it may be more difficult to distinguish the S parameter response of divacancies from monovacancies. Positrons implanted into the defected region will annihilate both in bulk ($S = 1.00$) and in divacancies (S=1.04), which would result in a measured S parameter between these values. If the measured S was greater than 1.025 then we would know it was due to non-saturation trapping of divacancies, as monovacancies could not cause a response greater than the saturation value. Conversely, if the measured S was less than or equal to 1.025 it could reflect saturation trapping by monovacancies or non-saturation trapping by either defect type.

3.3 Experimental Method

3.3.1 Apparatus

A schematic diagram of the sample chamber is shown in figure (3.2). A copper cold finger connected to a helium expander cooling unit replaces the simpler sample holder of described in §2.4.6. This facilitates positron measurements to be made at low temperatures. Figure (3.3) is a detailed diagram of the adapted copper cold finger/sample holder showing the high voltage lead and break with sapphire insert. Figure (3.4) is a photo of the external cooling apparatus attached to the positron beam at Bath.

To achieve the necessary low temperatures *in situ* the sample was mounted on a cold finger connected to a compressor head of an ADP Cryogenics closed-cycle helium refrigerator. The cold finger was a 25mm-diameter copper rod, half of which was milled away to form a flat, vertical mounting surface. The $25mm^2$ silicon sample was secured in position by two screws and a small amount of vacuum grease.

As the sample was to be floated at high voltages it needed to be in good thermal contact but electrically isolated from the Cryostat cooling unit. This was achieved by slicing the copper rod in two and inserting a disc of 0.3 mm thick, 50mm diameter sapphire held in place with teflon clamps. Sapphire has high thermal, but low electrical, conductivity, allowing the sample and its copper mount to be cooled to 48.5K and to be held at a negative potential of up to 10 kV. The potential was applied via a high-voltage feedthrough and a wire with appropriately effective (60kV) insulation.

The cryostat had an inbuilt temperature probe and gauge but due to the length of copper rod and presence of sapphire disc it could not be guaranteed that this reading was the actual sample temperature as a gradient was sure to exist. Hence detailed temperature calibration was carried out the results of which are presented in the next section.

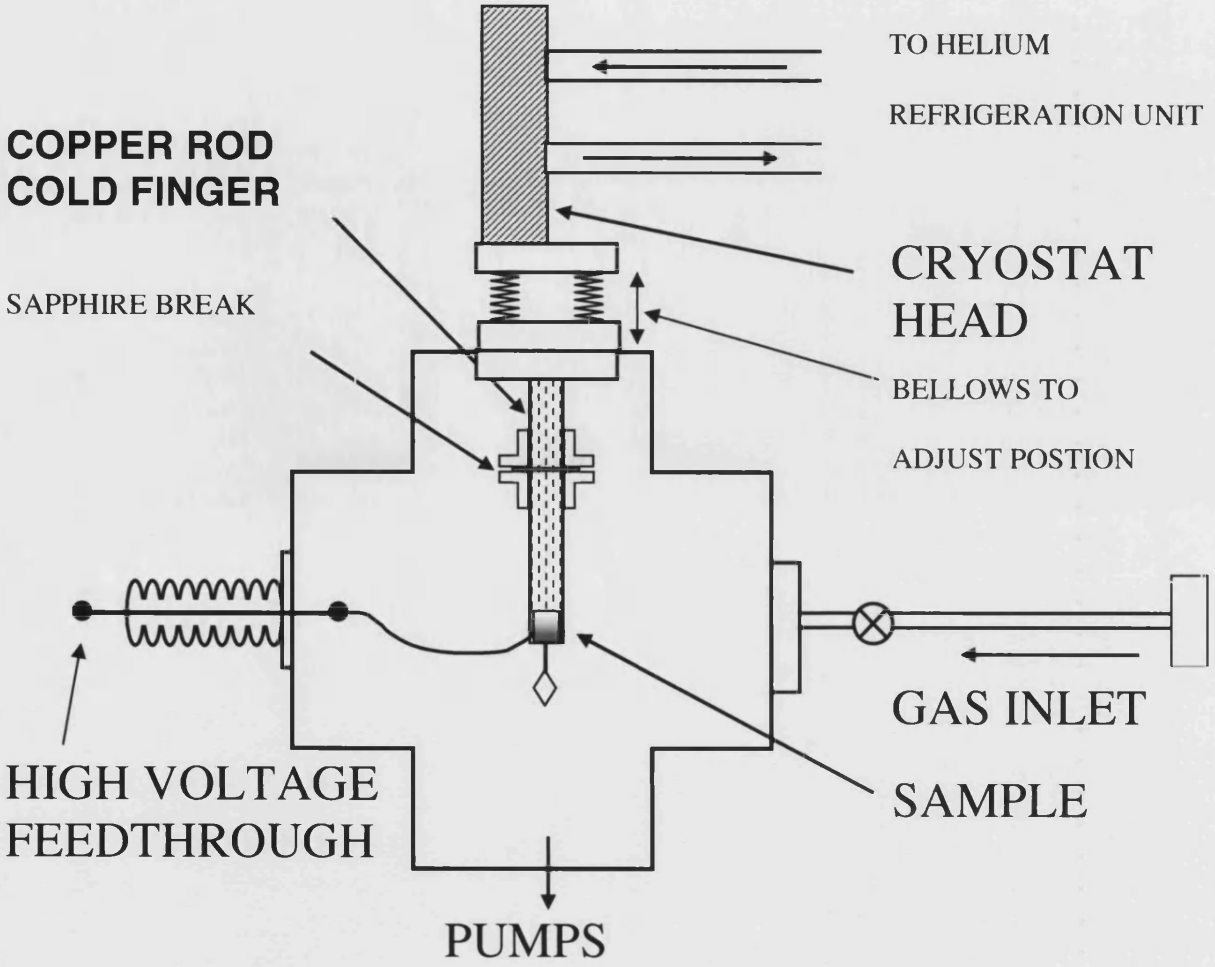

Figure (3.2)

Schematic diagram of the sample chamber; The sample is attached to the end of a copper rod (cold finger), the other end of which is attached to the compressor head.

There is a break in the cold finger in which a sapphire disc is inserted. The two halves are held together with teflon clamps.

The vertical position of the sample is manipulated with the bellows.

The high voltage is applied to the sample via the wire attached to the high voltage feedthrough. The ions to be implanted are bled in as a gas via the gas inlet.

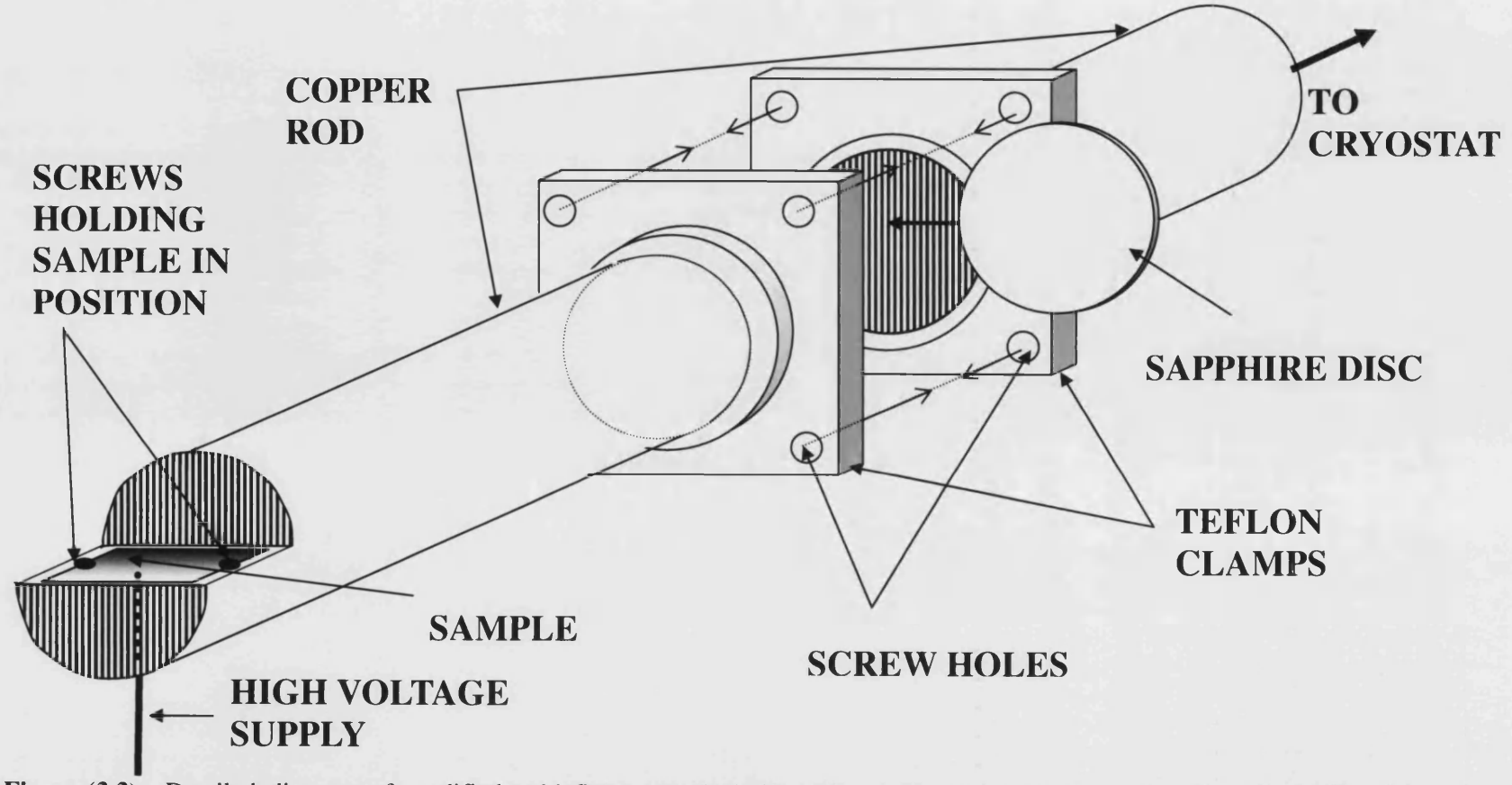

Figure (3.3) Detailed diagram of modified cold finger-sample holder; the copper rod was split and a disc of sapphire inserted to electrically isolate the sample end but maintain thermal contact with the cryostat. The sapphire was clamped between the copper rods with Teflon components.

The cold finger was mounted vertically in the sample chamber of the positron beam system at Bath described in Chapter 2. The compressor flange was mounted on a bellows-type linear travel manipulator, allowing vertical positioning of the sample in the beam line using a diamond-shaped projection attached to the base of the sample mount. The positron beam position was adjusted until the shadow of the diamond was seen in the centre of the image of the beam by viewing a microchannel plate-phosphor screen assembly at the end of the beam line. This was repeated for every positron energy used, and a file built up including every beam accelerating potential and the currents in two trim coils used to position the beam correctly. The centre of the sample was then moved to the position formerly occupied by the diamond and measurements taken under computer control.

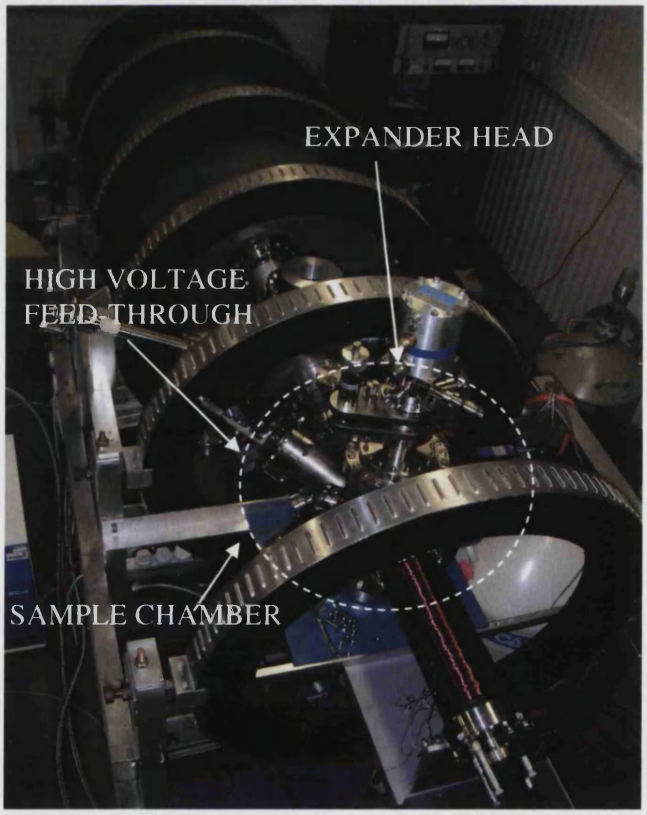

Figure (3.4) External photograph of the positron beam at Bath with cryostat attached. Dotted circle shows the approximate position of the sample chamber. The copper cold finger (unseen) is attached to the compressor head.

3.3.2 Thermocouple calibration

The cryostat-cold finger unit was equipped with a built in thermocouple and heater but due to the positioning of this at the top of the cold finger the reading it gives is not necessarily the temperature of the sample. In order to verify what, if any, temperature gradient existed between the cold finger and the sample a number of tests were carried out with a second thermocouple positioned exactly where the sample would be. The idea was to ascertain the relationship linking the two temperatures so that during the actual ion implantation the integral thermocouple of the cold finger could be relied on. This was necessary because it would not be possible to have the second thermocouple positioned on the sample during the high voltage ion implantation.

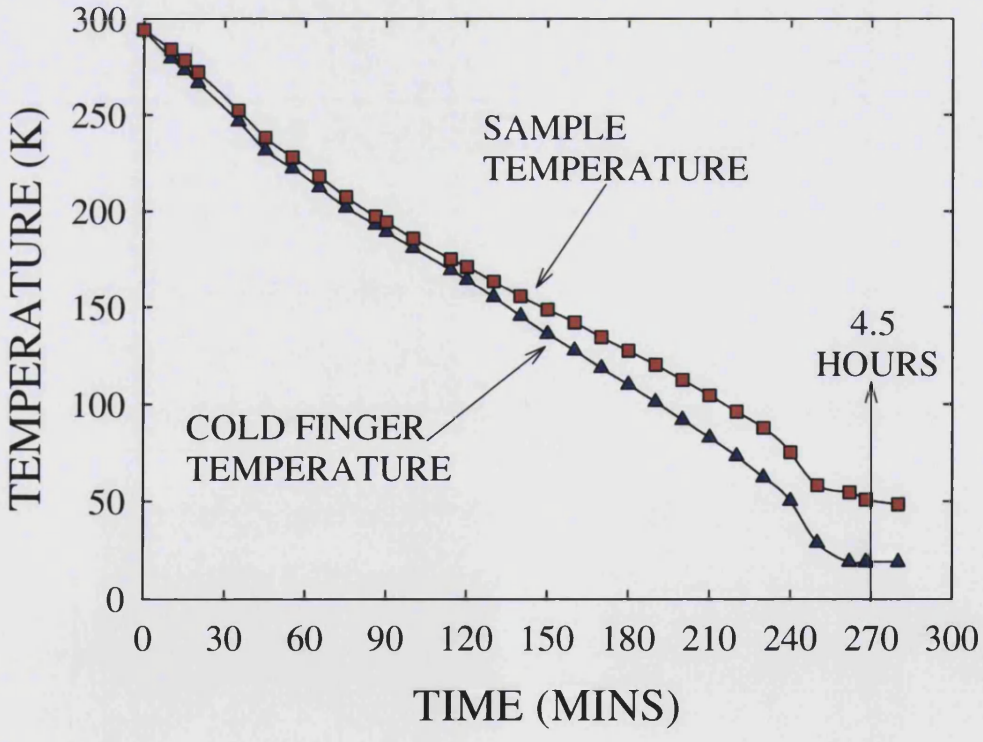

Figure (3.5 Time for the cold finger (-▲-) and the sample.(-■-) to cool to lowest possible temperatures of 18.8 K and 48.5 K respectively.

The first test simply involved turning on the cryostat and recording the temperatures of the cold finger and sample every 10 minutes until the lowest temperature was reached. This is shown in figure (3.4). Between room temperature and ~160K the two temperatures are comparable, below this a separation develops. After 4.5 hours the cryostat reached the lowest temperatures which were 18.8K for the cold finger and 48.5K for the sample.

The system was then warmed up in stages allowing the temperature to stabilise and the sample and cold finger temperatures recorded. The cold finger and sample temperatures are plotted against each other on figure (3.6) along with the cooling data.

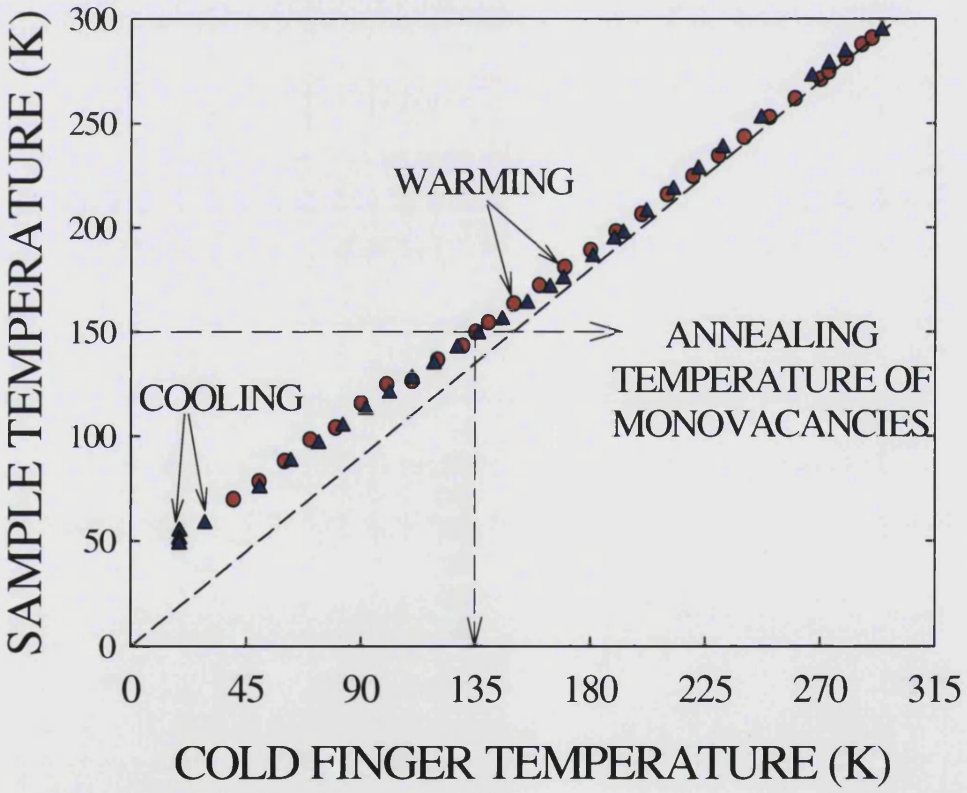

Figure (3.6) The cooling (▲) and warming (●) lines showing the relationship between the cold finger temperature and the sample temperature. The dashed diagonal line shows the x = y relationship for comparison.

The important temperature is 150 K as this is the lowest value in the range of published annealing temperature of monovacancies [3.11] and it is vital that the sample is well below this during the ion implantation and subsequent positron measurements. For the sample to be < 150K then the cold finger should be reading at least < 135K.

The final test involved positioning the secondary thermocouple at the sample point as the integrated thermocouple of the cold finger. The cryostat was then set to 40K, 60K, 150K, 200K and 250K and the temperatures monitored every minute on both thermocouples at each temperature for up to an hour. The results of the 40K and 60K monitoring are displayed in figure (3.7). The 60K results have been shifted on the time axis to align with the 40K results. The cold finger readings in both cases were constant and never more than 0.1K from the programmed temperatures. The secondary thermocouple recorded an oscillating temperature with a period of about 15 minutes. This same pattern was observed at all temperatures although only two (40K and 60K) are shown here in figure (3.7).

The oscillations are probably due to the internal temperature regulatory system of the cryostat which are electronically filtered by the control box of the integral thermostat system which is why they do not show up on the cold finger readings. This was tested by monitoring the temperature of the system at room temperature. As expected the oscillations were not present due to the equilibrium temperature requiring no heating or cooling. The average maxima and minima were measured so that the average peak to trough amplitude of the oscillations could be calculated. The amplitude decreased as the temperature increased from the highest value of ~5 K at 40 K to 1.6 K at 250K. The average temperature of the thermocouple was always within 2K of the set temperature apart from 40K where it was closer to 3K.

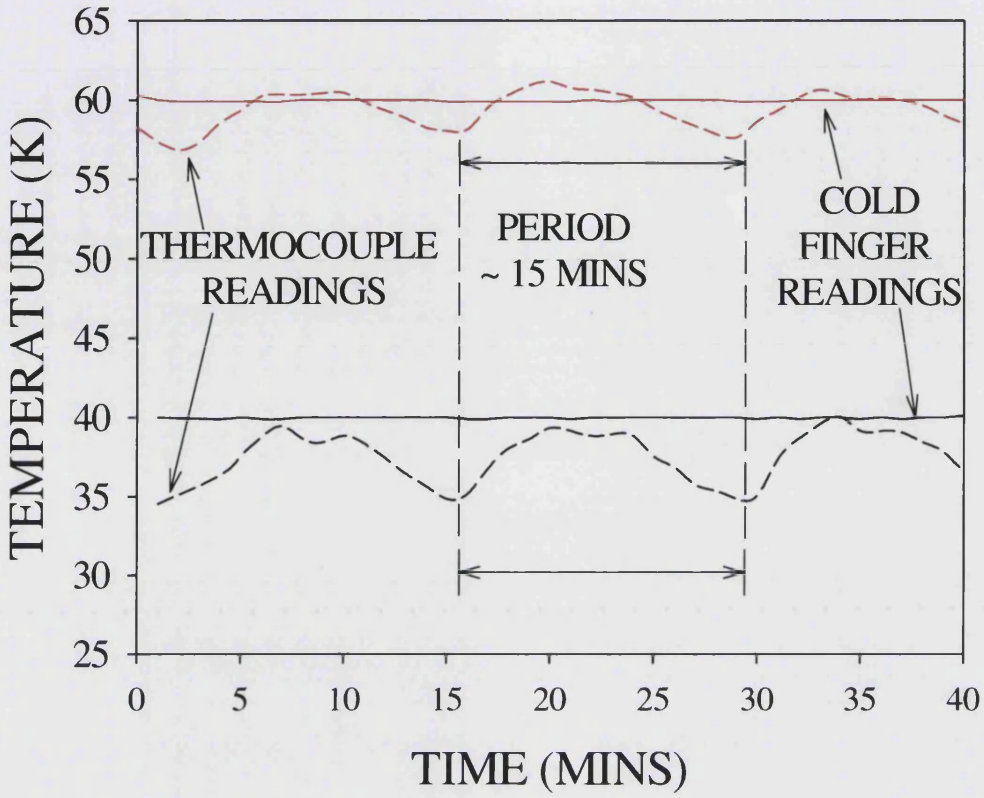

Figure (3.7) The cold finger (sold lines) and secondary thermocouple readings (dashed lines) of temperature when the thermostat is set to 40K (black lines) and 60K (red lines)

In conclusion, as expected the sample temperature is higher than the cold finger temperature; this effect is more pronounced at lower temperatures and hardly noticeable above 160K. The integral cold finger thermocouple filters out the oscillations of the feedback system but they are present. However the differences in temperature are small and for this application are unimportant. The crucial thing is that the sample is well below the lowest possible annealing temperature of monovacancies, ~150K which is easily attained by maintaining the cold finger well below 135K. The lowest temperature the sample can be maintained at in the present set up is 48.5K which is more than adequate for these purposes.

3.3.3 Experimental Procedure

The experimental procedure was as follows. First, measurements of the S parameter at incident positron energies E between 0.5 and 30 keV were taken for the silicon sample at room temperature. The sample was then cooled to 60K and the measurement of $S(E)$ repeated. -6 kV was then applied to the sample and helium gas bled into the sample chamber until a glow discharge was observed through the chamber window. This discharge was maintained for 30 seconds and, after pump down, $S(E)$ was remeasured. This procedure was repeated until a large increase in the value of S was seen for positron energies associated with mean probed depths of approximately of 75 nm (i.e., about 2.5 keV), at which the peak of vacancy-type damage by 6keV helium atoms was expected. $S(E)$ for the sample in this condition was recorded. The sample was then progressively heated in stages up to room temperature, and at each temperature $S(E)$ was recorded.

3.4. Results and Discussion

Positron measurements were made on a virgin sample of silicon at room temperature. The sample was then cooled to 60K and damage was introduced by ion implantation and further $S(E)$ measurements taken. The sample was heated up to a series of intermediary temperatures where more positron measurements were taken. Examples of $S(E)$ at 60, 170 and 300K are shown in figure (3.8). Raw data at other temperatures were recorded but lay between those shown.

The positron response is as expected; a peak in $S(E)$ at ~ 2.5 keV. However, as the measurement temperature increased past the monovacancy annealing temperature (~170K) the change in S is slight and, possibly, within experimental uncertainties.

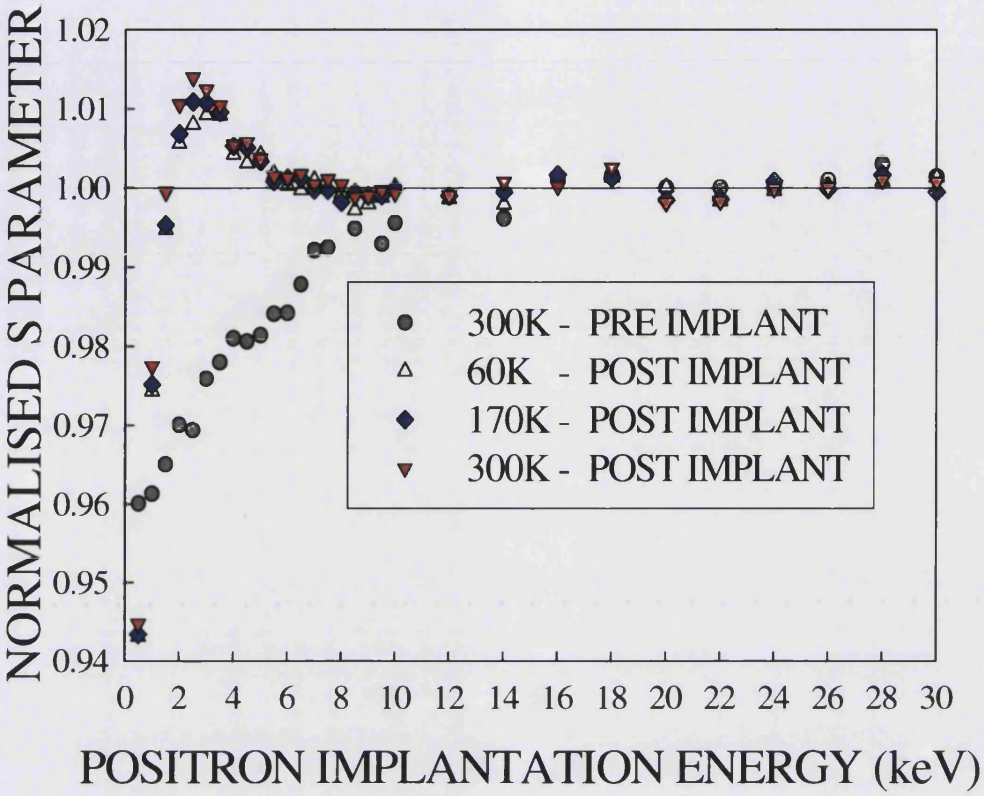

Figure (3.8) Normalised *S*(E) response for silicon before and after *in situ* implantation with 6keV helium at 60K. Figure shows *S(E)* taken at room temperature prior to implantation and data taken post implantation at 60K and 170K and 300K.

This lack of change with temperatures in *S(E)* response could be because concentration of monovacancies initially created was coincidentally such that the resulting divacancy response after heating was approximately the same as the original monovacancy response. The following calculation is an attempt to estimate the changes in the *S(E)* peak that could be expected with a temperature increase from 60K to 300K if the damage peak in figure (3.8) is indeed due to monovacancies and these were to anneal to divacancies.

If the *S* parameter for the defect layer at 60K (figure (3.8)) is taken to be 1.01 then it is possible to work out the approximate values average monovacancy concentration. This is done by combining the expression for the de-surfaced *S* parameter in a defected layer (eqn (1.17)) with an expression for the proportion of positrons that annihilate at defect sites (eqn (1.17)) reproduced below for clarity:

$$S_{LAYER} = P_{DEFECT} S_{DEFECT} + (1 - P_{DEFECT}) S_{BULK} \tag{1.17}$$

where S_{LAYER} is the de-surfaced layer S parameter and P_{DEFECT} is the proportion of positions that annihilate in the layer that do so at defect sites.

$$P_{DEFECT} = \frac{\nu C_D}{\nu C_D + \lambda} \tag{1.18}$$

where C_D is the concentration of defects per atom, λ the positron decay rate in defect free material (4.54×10^9 s^{-1} for silicon) and υ is the specific defect trapping rate which has values of 5×10^{14} s^{-1} and 1×10^{15} s^{-1} for monovacancies and divacancies, respectively [3.12]. The rate for divacancies is double the rate of monovacancies.

Combining equations (1.17) and (1.18) and substituting S_{BULK} = 1.00 gives an expression for the defect concentration per atom:

$$C_D = \left(\frac{\lambda}{\nu}\right) \frac{(S_{LAYER} - 1)}{(S_{DEFECT} - S_{LAYER})} \tag{3.1}$$

Multiplying C_D by the number of silicon atoms per cubic centimetre (5.15×10^{22} cm^{-3}) yields the density of monovacancies.

Using the S layer value of 1.01, the appropriate defect trapping rate and S parameter defect value of 1.025 gives a value for monovacancy concentration of about 3×10^{17} cm^{-3}. If the number of vacancy trapping sites falls to 5% on annealing, as is commonly thought to be the case, then the divacancy concentration would be 1.5×10^{16} cm^{-3}. By doing the calculation in reverse (see eqn (3.2) with the correct divacancy parameters it is possible to work the new value of S_{LAYER}

$$S_{LAYER} = \left(\frac{\nu C_D}{\nu C_D + \lambda}\right)(S_{DEFECT} - 1) + 1 \tag{3.2}$$

The above values produce a new *S* parameter for the layer, assuming 5% of vacancies traps survive in the form of divacancies, of ~1.0024, which is only fractionally larger than undefected bulk silicon. If this value is correct then it suggests that the density of monovacancies created was not great enough to be distinguishable from bulk silicon on annealing. This could be rectified in future experiments by discharging the gas for longer periods to increase the concentration of defects. This simple calculation depends on parameters (e.g. the percentage of vacancies surviving as divacancies) whose absolute values are at best only known to within 50% and at worst to within an order of magnitude.

Furthermore the fact remains that as the temperature increased no change was observed in the *S* Parameter response to bulk or otherwise. Let us consider whether this could be due to the vacancies created during ion implantation trapping the implanted helium. The presence of helium decorating the vacancies would affect both positron trapping rates and defect *S* parameters, and this effect is quite likely because the helium ions were implanted at 6keV so the peaks in ion and vacancy distributions are only separated by ~30nm. (see Figure (3.1)). However, only about 2% of the vacancies could be filled with helium atoms (each ion produces about 45 vacancies) and so the effect is likely to be negligible.

Another possibility is that the sample was not actually at 60K during the implantation process. The sample may have lost thermal contact with the cold finger at some point meaning that the damage was basically created at room temperature. In this case the initial monovacancies would have rapidly annealed to divacancies and hence no changes would be observed at different temperatures. It would consequently be inappropriate to draw quantitative conclusions from the data presented here.

The final possibility is that the ion dose was such that the near surface region of the sample was amorphised, and thus the positron response would not change at 300K.

It is therefore difficult to draw quantitative conclusions about the possible evolution from monovacancies to divacancies from the data presented here. Nevertheless, the data of figure (3.8) do suggest that the technique is worth pursuing. The principal differences in future measurements will be:

(A) *The avoidance of significant helium decoration of vacancy damage.*
This can be achieved by one of two methods. Increasing the energy of the implanted ions by increasing the voltage applied to the sample. This would result in a larger separation of the vacancy and ion distribution profiles thus decreasing the chance of helium ions decorating vacancies. The other method is to create the damage using heavier ions which are less mobile than lighter ions and therefore less likely to migrate to vacancy site and if they did the trapping probability is lower for heavier ions. Heavier ions would need to be implanted at higher energies to ensure the damage was created suitable distances from the surface because of the lower mean implantation depth.

(B) *Creating adequate defect concentrations*;
By extending the duration of the gas discharge during ion implantation one can increase the likelihood that an adequate concentration of defects will be present both before and after annealing. An estimate of the density of monovacancies required to produce an average layer S parameter change from 1.024 to 1.025 on annealing was calculated (from eqns (3.1) and (3.2)). Assuming 5% trapping site survival rate on annealing the monovacancy concentration worked out to be ~7.8×10^{18} cm^{-3} which is roughly 2.5 times the number estimated from the data of figure (3.8). A possible method of calibrating the damage produced during the *in situ* ion implantation is comparing the $S(E)$ response of these samples at room temperature with sample implanted with known doses in ion beams.

(C) *Ensuring constant thermal contact between the sample and cold finger.*

Refinement of the physical set up to ensure that the sample and cold finger never lose thermal contact.

Further measurements, building on the experience of the research described above, were undertaken by P.G. Coleman and C.P. Burrows. The results of their experiments are summarised in the following section.

3.5 New Research

This progress that was made formed the foundation of work that was carried on by the group and some successful results were obtained. Many thanks to Paul Coleman and Paul Burrows for the following data.

Figure (3.9) shows some of the results obtained since the development of the technique and the early results, using 20keV helium ion implantation. This data has a clear damage peak with an *S* parameter peaking at ~1.025, which is indicative of the presence of monovacancies. The damage peak is a little deeper than in figure (3.8) because of the higher energy of the helium ions.

They studied the change in the peak *S* Parameter *S (E=3.5keV)* as a function of time for different types of silicon with a view to calculating activation energies. With FZ Si they observed a single annealing step at 250K from *S* = 1.024 to 1.009 over a period of about 24 hours. See figure (3.10).

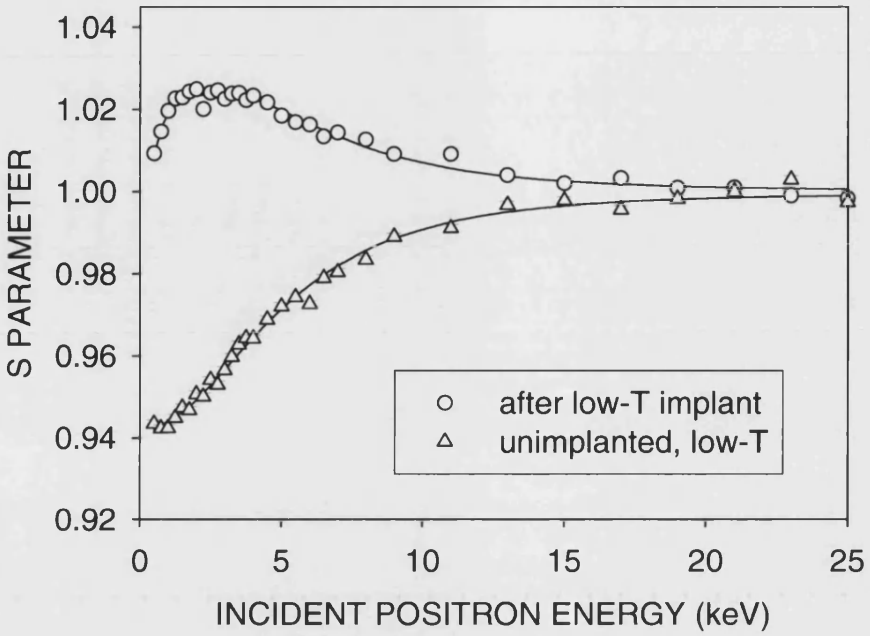

Figure (3.9) *S(E)* response of silicon at low temperature before (-Δ-) and after (-O-) ion implantation with 20keV helium ions [3.13].

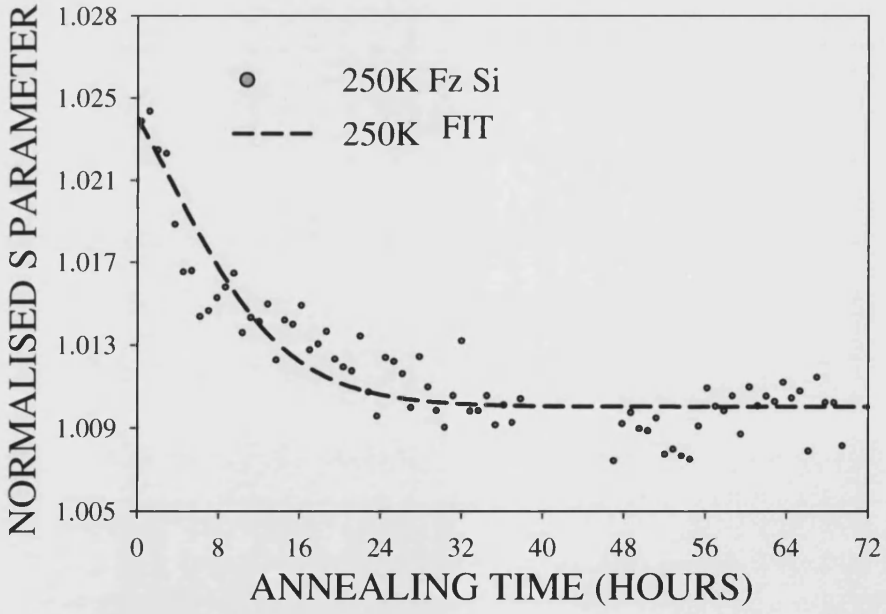

Figure (3.10) The change of *S*(*E*=3.5keV) as a function of time in FZ Si at 250K after low temperature *in situ* implantation of 20keV He ions [3.13].

The same process and experiment was carried out with n^+ doped silicon. In this case two distinct annealing stages were observed at 263K and 337K. This could be due to the vacancies or interstitials getting trapped by impurity atoms (of which there is an abundance) after partial annealing and becoming less mobile. At the higher annealing temperature the vacancies and interstitials start moving again and annealing proceeds.

This work is continuing.

3.6 Conclusions

The aim of this study was to directly observe monovacancies created during ion implantation in silicon using positron annihilation spectroscopy. This necessitated overcoming the practical difficulties involved in performing *in situ* ion implantation to create damage at temperatures well below the monovacancy annealing temperature of ~170K. The low temperature had to be maintained during subsequent positron measurements to prevent agglomeration or recombination of the introduced damage.

The post implant low temperature results show a *S(E)* peak at ~2.5keV which is evidence that vacancy type damage was introduced at some point during the implantation process. The *S* parameter was 1-2 % greater than the bulk value which may have been indicative of monovacancies. However the peak did not change significantly as the temperature increased, which is what one would have expected as the monovacancies annealed to divacancies.

There are a number of possible reasons for this lack of change. The first is that monovacancies recombined and agglomerated forming the exact proportion of divacancies that would produce an S parameter in the damage peak of ~1.02. Rough estimates of the values involved make this possibility unlikely. The second is that some of the vacancies trapped the implanting ions. This decoration would have influenced trapping rates and *S* Parameters, but is likely to have an influence only at the ~ 2% level. The third is that the sample was not actually in thermal contact with the cold finger during the 6keV

implant. This would mean that the monovacancies would have already annealed by the time any positron measurements were taken. The fourth is that the sample was amorphised and could not be recrystallised at 300K.

As a result it is difficult to draw quantitative conclusions regarding the evolution of monovacancies to divacancies from the data presented here. However, the progress made here into the development of the technique enabled further work to be carried on the activation energies by studying the changes *S* Parameter in the peak as a function of time at a set temperature and this work is continuing.

CHAPTER 4

DIRECT HIGH RESOLUTION DETERMINATION OF VACANCY TYPE DEFECT PROFILES IN ION IMPLANTED SILICON

4.1 Introduction

Profiling of defects is attained in conventional position spectroscopy experiments by using a variable energy positron beam and therefore controlling the average depth of the incident positrons. This is the technique known as Variable Energy Positron Annihilation Spectroscopy (VEPAS). The higher the energy of the incident positrons the deeper into the sample they probe but by the nature of the positron implantation profile a loss of resolution occurs at higher energies. This is due to the spreading out of the implantation profile (and therefore the annihilation profile) as the energy increases (see figure (4.1)). In the following experiments this decrease in resolution is overcome at the expense of the non destructive nature of VEPAS. This is achieved by progressively etching samples and thus bringing deeply buried defects to the surface and allowing them to be probed with low energy positrons at a higher resolution.

4.2 VEPFIT and Implantation Profiles.

Control of the energy of the implanted positrons, typically between 0.5 and 30 keV, allows one to gain some semi-quantitative information non-destructively on the depth profile of the defects. This information is usually obtained through fitting raw positron data with a code such as VEPFIT [4.1], which assumes a Makhovian positron implantation profile: (See §1.3.6 and equations (1.1), (1.2) and (1.3)

$$P(z,E) = \frac{mz^{m-1}}{z_0^m} \cdot \exp\left(-\left(\frac{z}{z_0}\right)^m\right) \qquad (4.1)$$

where z is the distance measured from the surface, E is the incident positron energy, and z_0 is related to the mean implantation depth, $\bar{z}$ (= $(40/\rho)E^{1.6}$ for a material of density ρ) (z_0 in nm and E in keV). The most widely accepted version of eq (4.1) uses $m = 2$ – ie, $P(z, E)$ is a Gaussian derivative, for which $z_0 = 1.13\bar{z}$. The implantation profiles of 5keV, 10 keV and 20 keV positrons in silicon are shown in figure (4.1)

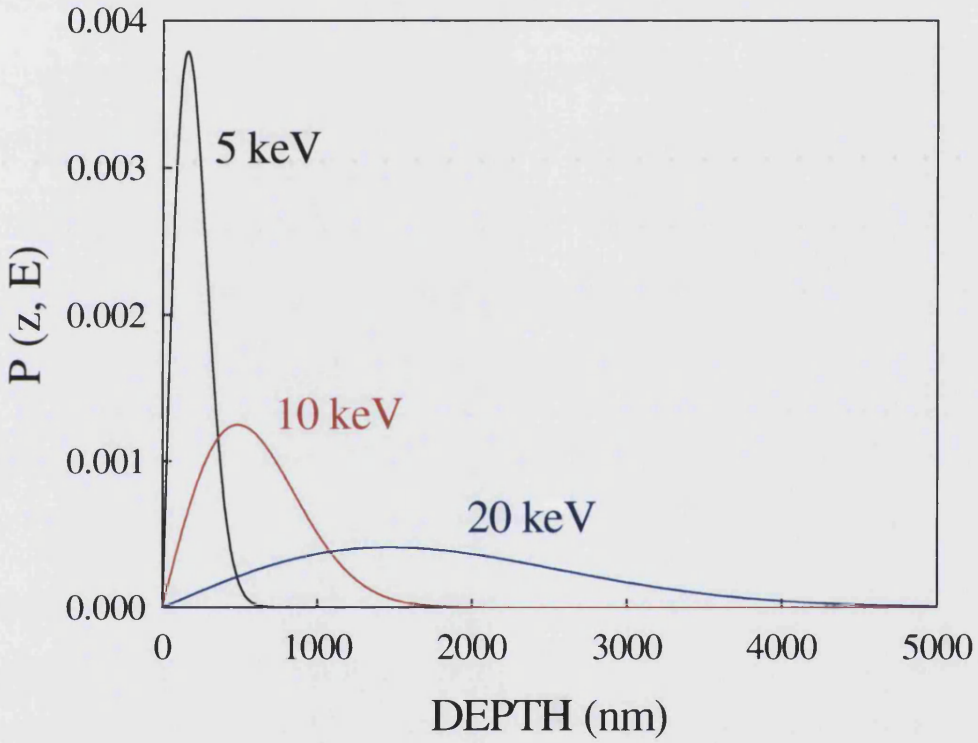

Figure (4.1) Implantation profiles of 5keV, 10keV and 20keV positrons in silicon showing the broadening of the profile as the energy increased

Using the implantation profile VEPFIT then solves the positron diffusion equation and calculates a positron annihilation depth profile which best fits the observed data $S(E)$. This is achieved by fitting values for the S parameter and the effective positron diffusion length L_{eff} in each of any number of layers whose boundaries can either be fixed or fitted. For the simplest case of ion-implanted silicon, VEPFIT will fit the raw data by assuming a simple defect box profile of fitted thickness having characteristic values of S and L_{eff}. Average defect concentrations

C_D can be deduced from L_{eff} if the specific trapping rate for the predominant defect type, ν, and the mean positron lifetime in pure Si, λ, are known:

$$L_{eff} = L\left(\frac{\lambda}{\lambda + \nu C_D}\right)^{\frac{1}{2}} \tag{4.2}$$

Where L is the diffusion length in defect free bulk and for silicon has a generally accepted value of 250nm. L_{eff} decreases as the concentration of defects, C_D increases because the positrons are more likely to be trapped and annihilate. Figure (4.2) shows the relationship between L_{eff} and C_D for silicon. The inset graph has C_D on a log scale. As the effective diffusion length drops very rapidly to a few nm with increasing defect concentration, the implantation profile is a good enough approximation to the annihilation profile as the positrons cannot diffuse far before they annihilate.

The more complicated a defect profile is the more unreliable fitting results become; generally it is wise to accept the simplest model for which a good fit can be obtained and so one obtains only an indication of the defect distribution and its average S parameter. In the simplest case of silicon implanted with one type of ion, VEPFIT fits a square box defect profile. This is shown in figure. (4.3b) with figure (4.3a) which is the normalised S Parameter data that it is fitted from.

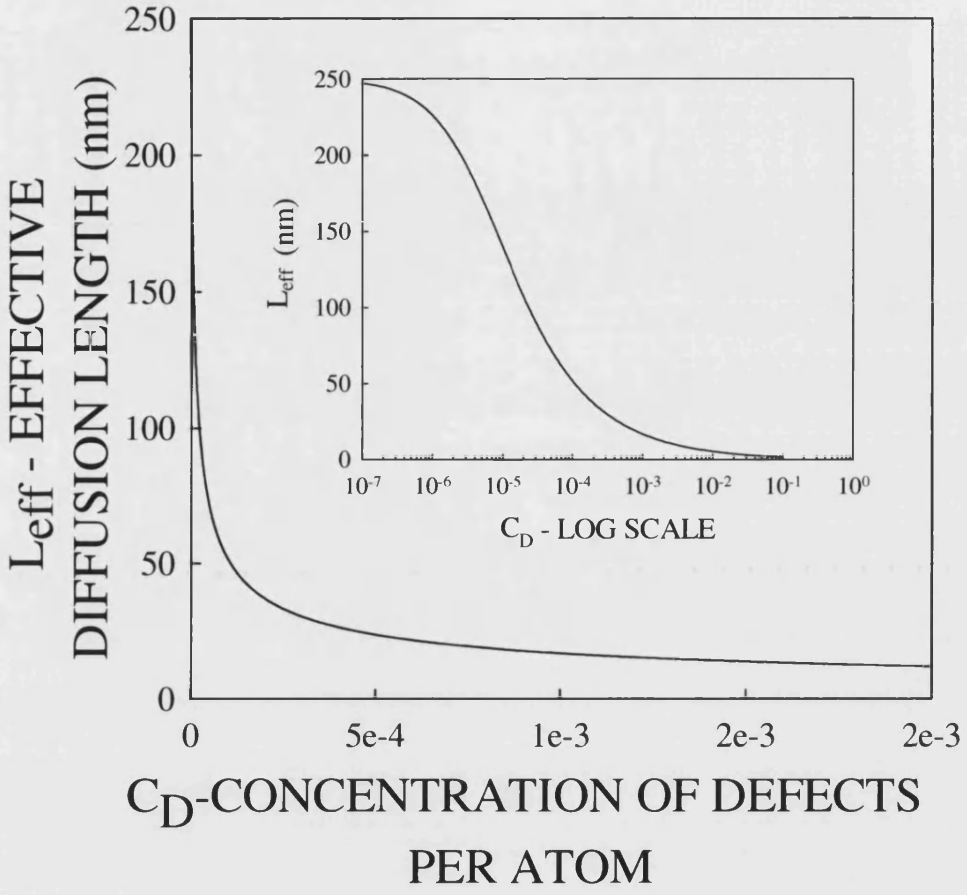

Figure (4.2) The relationship between the effective diffusion length L_{eff} and the concentration of defects per atom C_D as given by eqn (4.2) using $\lambda = 4.54 \times 10^9\ s^{-1}$ (the positron decay rate in the undefected silicon) and $\nu = 10^{15}$ s (specific trapping rate for divacancies). The inset graph shows the same relationship plotted with C_D on a log scale.

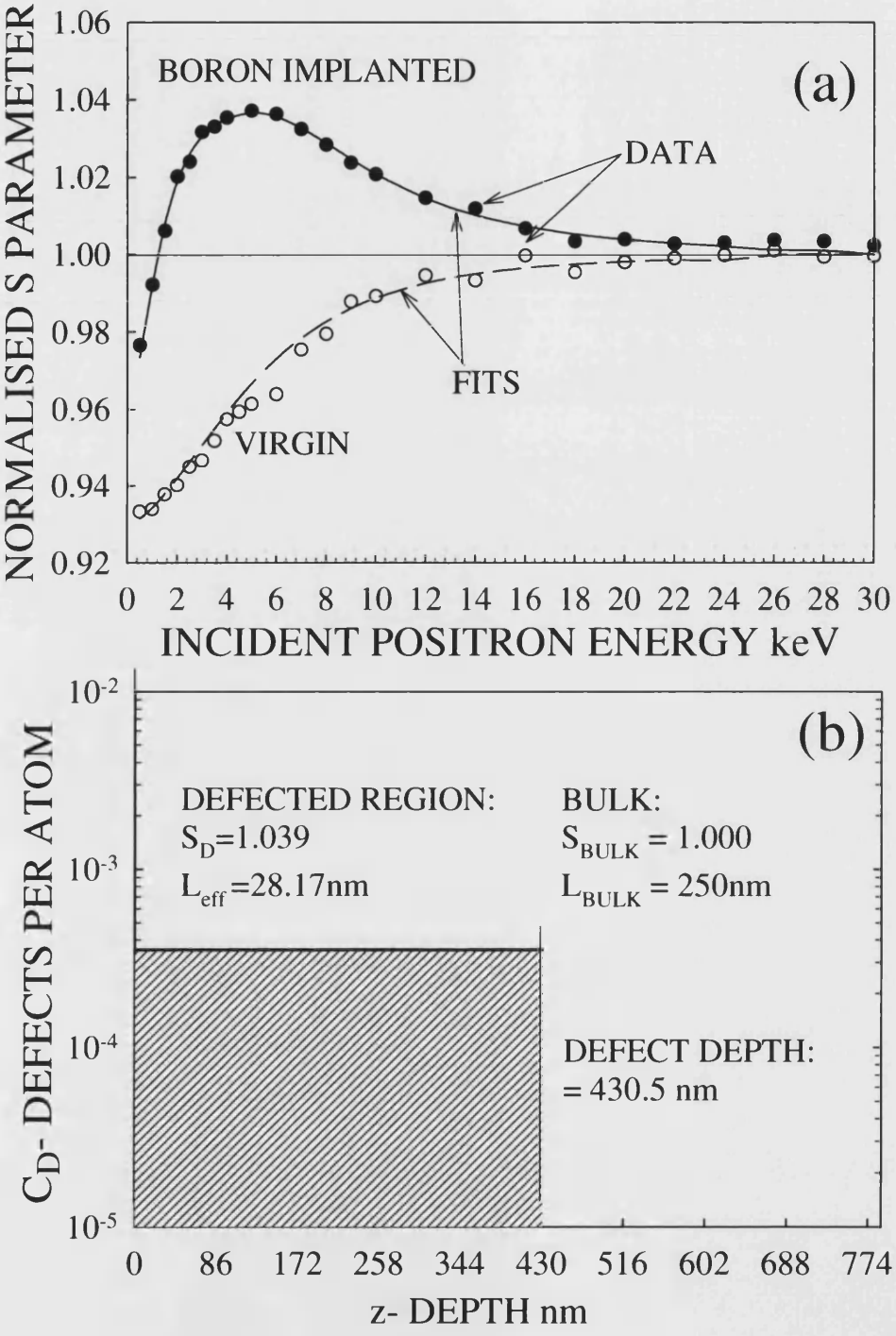

Figure (4.3) (a) *S* parameter data and fits for virgin and 100 keV boron ions implanted into silicon at a dose of $5x10^{14}$ ions /cm^2. **(b).** The square box profile obtained from (a). The simplest profile with a good fit and therefore the one to accept from VEPFIT.

4.3 Enhanced Resolution

The method of enhanced resolution profiling has been applied in a new way with an alternative analytical approach which bypasses the need for VEPFIT. The aim was to build up an accurate, complex, complete picture of the defect profile without losing resolution of deeper defects.

If the non-destructive nature of the standard spectroscopy is abandoned then damage profiling by VEPAS with approximately constant depth resolution can be realized. The sample is progressively etched to bring successive parts of the defect distribution close to the surface. These defects can then be probed using the low energy, high resolution positrons.

This concept – valid only if the etching does not itself introduce appreciable new damage – is illustrated schematically in figure (4.4). After etching the shaded layer of defects is at the surface and a narrow distribution of positrons can be implanted into it, whereas without etching the same layer – now buried – it can only be reached by high-energy positrons which have a very broad implantation profile; only a small fraction of the implanted positrons stop in the layer of interest, and the VEPAS response is considerably smeared as a consequence. Thus the narrow $P(z,E)$ is maintained across the entire damage profile.

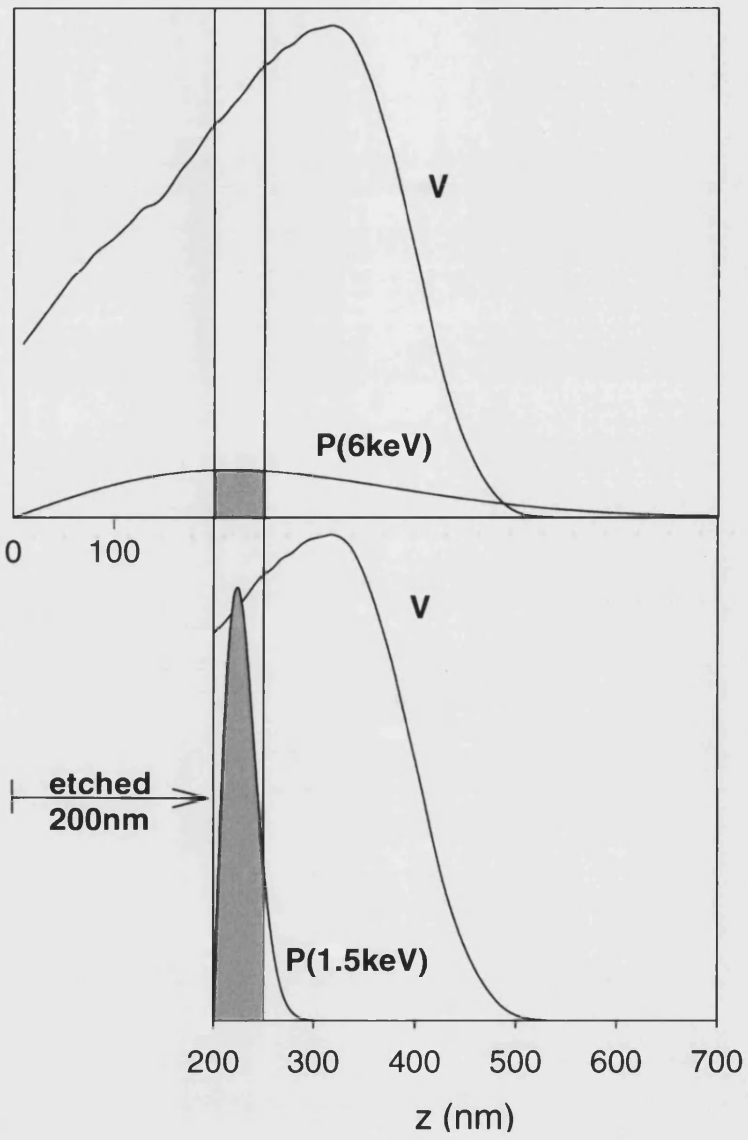

Figure (4.4) Example of interrogation of defects at depths z in the region 200-250nm below surface. Top: non-destructive (standard) method – peak sensitivity with incident positron energy E = 6 keV (FWHM of the positron implantation profile P ~ 350nm). Bottom: etch-and-measure method – over 90% of 1.5 keV positrons are implanted into the defect region after 200nm etched (FWHM ~ 40nm).

4.3.1 Previous Work

The principle of enhanced-depth-sensitivity VEPAS has been discussed by Knights, Coleman and coworkers [4.2-4.4] and by Krause-Rehberg et al [4.5], and applied by Malik et al [4.6], Knights et al [4.7] and Janson et al [4.8] to study deep defect tails, Simpson et al [4.9] to study damage caused by ions implanted through a SiO_2 layer, Fujinami et al to study damage in He-implanted Si [4.10], Saarinen et al and Kauppinen et al to study vacancy distributions in In-implanted GaAs and MeV proton-implanted Si [4.11,4.12], and Krause-Rehberg et al [4.13-4.15] to study damage caused by sawing GaAs wafers and impurity gettering at half-ion-range in self-implanted silicon. In refs. [4.6] and [4.7] simple one- or two-step etching was performed using anodic oxidation as an intermediate stage (as discussed later). In ref [4.8] etching was performed using an inductively-coupled plasma system. In refs [4.9-4.12] direct chemical etching was employed. In ref. [4.13] in-situ ion sputtering was used progressively to remove surface layers. In refs. [4.5] and [4.15] a 1 μm-diameter positron microbeam was used to scan across a wedge-shaped piece (cut angle ~ 1°) of ion-implanted silicon.

The following application of the enhanced resolution depth profiling uses anodic oxidation to etch much finer steps than any previous studies. A total of ten etch steps were used between 50nm and 544nm and a novel analytical approach was applied to the resulting data which was compared to simulation results.

Widely-used codes such as TRIM [4.16] calculate vacancy depth profiles, but do not account for post-implantation migration and agglomeration. For example, earlier VEPAS measurements have confirmed that at room temperature only a few percent of the original vacancies survive, and then in the form of divacancies. Secondary Ion Mass Spectrometry (SIMS) has been performed on the same samples, and advanced simulations have been performed which account for the crystalline nature of the sample and hence ion channeling during implantation.

4.4 Analytical Technique

Damage was introduced into a silicon wafer by implanting 100keV boron ions at a dose of $5x10^{14}cm^{-2}$. The damaged wafer was then divided into 10 pieces, each of which had a different thickness of silicon etched off the top surface. In order for this to work it was essential that the etching did not introduce extra new defects and that the defects in the original wafer varied in depth but were uniform in the x-y plane.

The analysis method is summarised as follows. The assumption is first made that we are able to model the defect profile as a series of ten boxes, each of thickness determined by successive etch depths. For each box layer a constant defect concentration was assumed and for each sample the box we study corresponds typically to the first 50nm or so.

Positrons entering the samples annihilate at the surface, in the bulk and in the defects species: i, ii, iii... with fractions; $F_{SURFACE}$, F_{BULK} and F_{DEFECT_i}, F_{DEFECT_ii}, F_{DEFECT_iii}.....and S Parameters; $S_{SURFACE}$, S_{BULK} and S_{DEFECT_i}, S_{DEFECT_ii}, S_{DEFECT_iii}, respectively. The measured S Parameter is a linear combination of these S Parameters and fractions. In ion implanted silicon the predominant defects are divacancies [4.17] so the measured S Parameter is given by eqn (4.3)

$$S_{MEASURED} = F_{SURFACE}S_{SURFACE} + F_{BULK}S_{BULK} + F_{DIVACANCY}S_{DIVACANCY} \qquad (4.3)$$

The incident positrons annihilate in one of these three locations so the sum of the three fractions is 1.

$$1 - F_{SURFACE} = F_{BULK} + F_{DIVACANCY} \qquad (4.4)$$

Of the positrons that do not diffuse to and annihilate at the surface, $(1\text{-}F_{SURFACE})$, the relative proportions that annihilate in bulk and divacancies (P_{BULK} and $P_{DIVACANCY}$ respectively) are given by eqns (4.5) and (4.6).

$$P_{DIVACANCY} = \frac{\nu C_D}{\nu C_D + \lambda} \tag{4.5}$$

$$P_{BULK} = \frac{\lambda}{\nu C_D + \lambda} \tag{4.6}$$

These proportions add up to 1 and depend on λ, the positron decay rate in defect free material. C_D is the concentration of defects per atom and ν the specific defect trapping rate. In order to convert P_{BULK} and $P_{DIVACANCY}$ to F_{BULK} and $F_{DIVACANCY}$ then one simply multiplies each equation by (1-$F_{SURFACE}$) This is how equations (4.7) and (4.8) are obtained and we now have F_{BULK} and $F_{DIVACANCY}$ in terms of C_D, λ , ν and $F_{SURFACE}$.

$$F_{BULK} = (1 - F_{SURFACE})\frac{\lambda}{\nu C_D + \lambda} \tag{4.7}$$

$$F_{DIVACANCY} = (1 - F_{SURFACE})\frac{\nu C_D}{\nu C_D + \lambda} \tag{4.8}$$

The fraction that annihilate at the surface is given by eqn (4.9) [4.18] where P(z, E) is the Makhovian implantation profile given in eqn (4.1) and L_{eff} is the effective diffusion length given by eqn(4.2)

$$F_{SURFACE} = \int_0^\infty P(z,E)\, e^{\frac{-z}{L_{eff}}}\, dz \tag{4.9}$$

The process by which C_D is obtained for each measured *S* parameter is outlined in the following 6 steps. The process (shown in Figure (4.5)) is repeated for the first few energies of each sample.

(1) Generate range of realistic values of C_D starting from C_D=0.

(2) For each value of C_D calculate the corresponding theoretical diffusion length, L_{eff}, from eqn (4.2)

(3) Calculate $F_{SURFACE}$, for each different L_{eff} / C_D pair, by using the implantation profile with energy, E_i, eqn (4.1) in eqn (4.9)

(4) By using the value of $F_{SURFACE}$ obtained in step (3) in eqns (4.7) and (4.8) calculate F_{BULK} and $F_{DIVACANCY}$ for each L_{eff} / C_D pair.

(5) Use these values of $F_{SURFACE}$, F_{BULK} and $F_{DIVACANCY}$ with S parameter values: S_{BULK}= 1, $S_{DIVACANCY}$ = 1.04 [4.19] and $S_{SURFACE}$ (measured from raw data) in eqn (4.3) to generate a theoretical S Parameter for each value of C_D, $S_{THEORY}(E_i)$.

(6) Values of C_D (and thus also L_{eff}) for which the computed $S_{THEORY}(E_i)$ equals the measured $S_{MEASURED}(E_i)$ are recorded and the process repeated for the two to four values of E_i corresponding to implantation into the first 50-100nm (depending on the etch depth). The weighted average of these is taken as the defect concentration for the near-surface box layer.

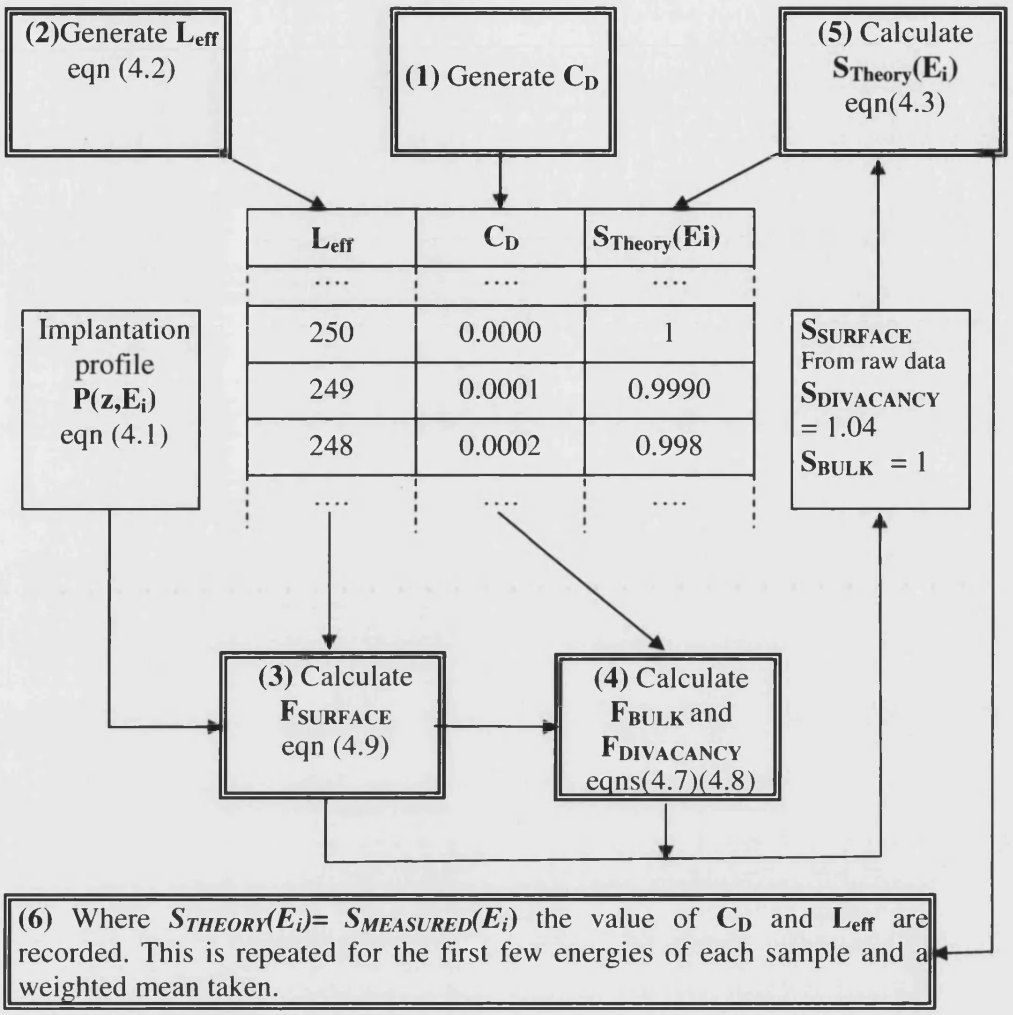

Figure (4.5) Diagrammatic explanation of analytical technique- (1) A range of realistic defect concentrations are generated and (2) their corresponding diffusion lengths. (3) Using the implantation profile at energy E_i the fraction that return to the surface is calculated for each pair of L_{eff} and C_D. (4) The fractions that annihilate in bulk and defect are calculated. (5) The three fractions are used along with the known bulk, surface and defect *S* parameters to calculate a theoretical *S* parameter for each C_D which is compared to the actual measured one. (6) This process is repeated for the first few energies of each sample from which weighted averages are taken.

4.4.1 Theoretical $S(C_D)$ Plots

The analytical technique described in the previous section is based on generating S parameters that would be measured for different defect concentrations (at one particular energy) Figure (4.6) is an example of a generated S Parameter at three different energies, 0.5keV, 1.0keV and 1.5keV for the unetched sample with $S_{SURFACE}$=0.960.

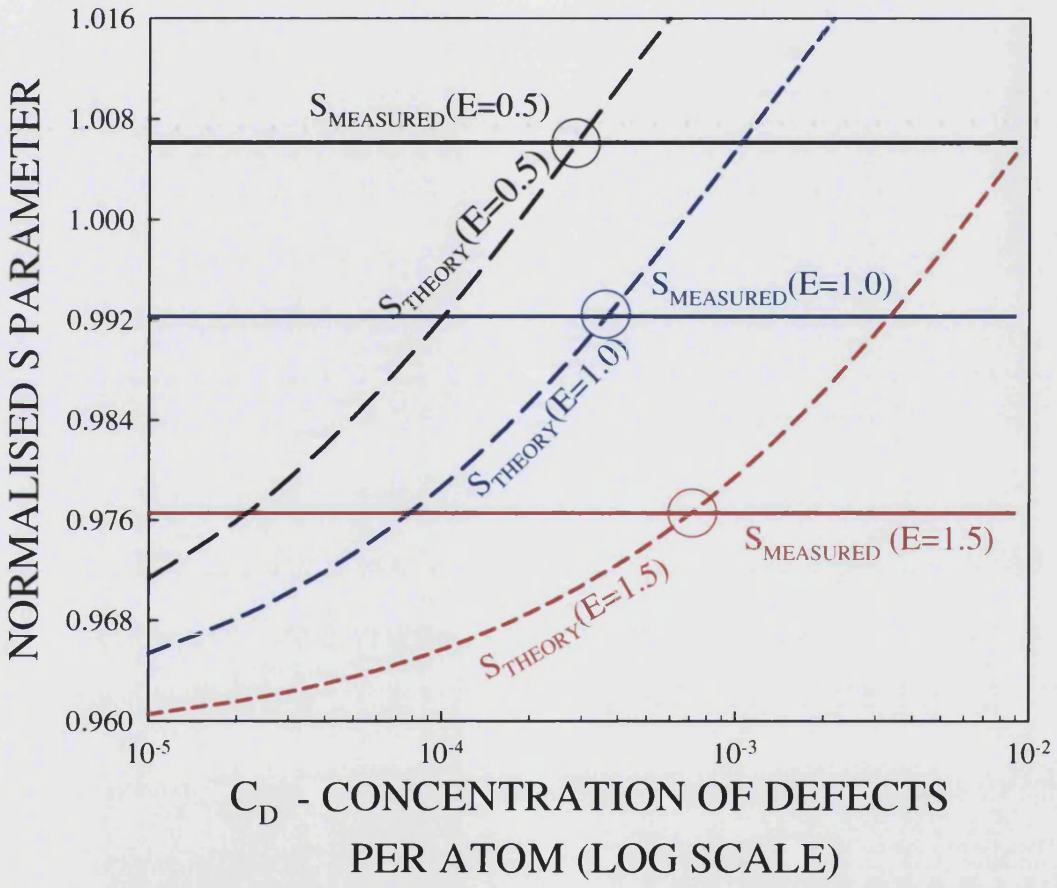

Figure (4.6) This data is for an unetched piece of silicon implanted with 100keV boron ions. For 0.5keV, 1.0keV and 1.5keV positrons, theoretical $S(C_D)$ plots were generated. From the raw data the S parameter of the surface was found to be $S_{SURFACE}$ = 0.960 and the measured $S(E)$ data: $S_{MEASURED}$ (E=0.5) = 0.977, $S_{MEASURED}$ (E=1.0) = 0.992 $S_{MEASURED}$ (E=1.5) = 1.006. where these values intersect the theoretical lines (marked with circles) are the values of C_D

For all three energies as the defect concentration increases, the measured S Parameter increases due to a greater fraction of positrons annihilating in defects (divacancies) with $S_{DIVACANCY} = 1.04$ which is 4% larger than the defect free bulk value of 1.000. The straight lines show the actual measured S Parameters and where they intersect with the curved theoretical lines are the values of C_D of interest. Although figure (4.6) is useful in demonstrating the relationship between $S_{MEASURED}(E_i)$ and $S_{THEORY}(E_i)$ the defect concentrations, C_D were obtained by comparing the numbers, using values of C_D to several decimal places to generate S_{THEORY} in the region close to $S_{MEASURED}$.

4.4.2 Positron Diffusion

An assumption of the theory is that the annihilation and implantation profiles are interchangeable. This is not an unreasonable assumption as at high defect concentrations the effective diffusion lengths decrease rapidly. However after implantation some positron diffusion will take place, the significance of which depends on the defect concentration and the implantation energy.

Once an initial value for C_D is obtained for each box layer (by taking a weighted average of the values obtained from method described above) a first order correction is made which allows for positrons diffusing into and annihilating in the adjacent layer. This is the subject of §4.6.3.

4.5 Experimental Method

4.5.1 The Samples

Samples of Cz Si were implanted with 100keV boron ions at a dose of 5 x 10^{14} cm^{-2}. Each sample was then etched progressively via anodic oxidation; Anodic oxidation is a commonly-used technique for impurity profile determination in silicon. It is described in some detail in [4.6] and in the following section. The samples and etch depths are presented in Table (4.1). These etch depths were confirmed by direct step measurements and by SIMS profiles of the unimplanted boron ions. Figure (4.7) shows the SIMS profiles for s1 and s6 along with the simulated profile. The SIMS depths agreement with the etch depths is within measurement uncertainties.

Table (4.1) The 10 samples created with the thickness of material which was removed. Measurements in nm.

Sample Name	Total etched off (nm)	Subsequent etch depth (Region of interest)
Unetched	-	53
s1	53	37
s2	90	42
s3	132	47
s4	179	30
s5	209	52
s6	261	33
s7	294	84
s8	378	83
s9	461	83
s10	544	No further etches

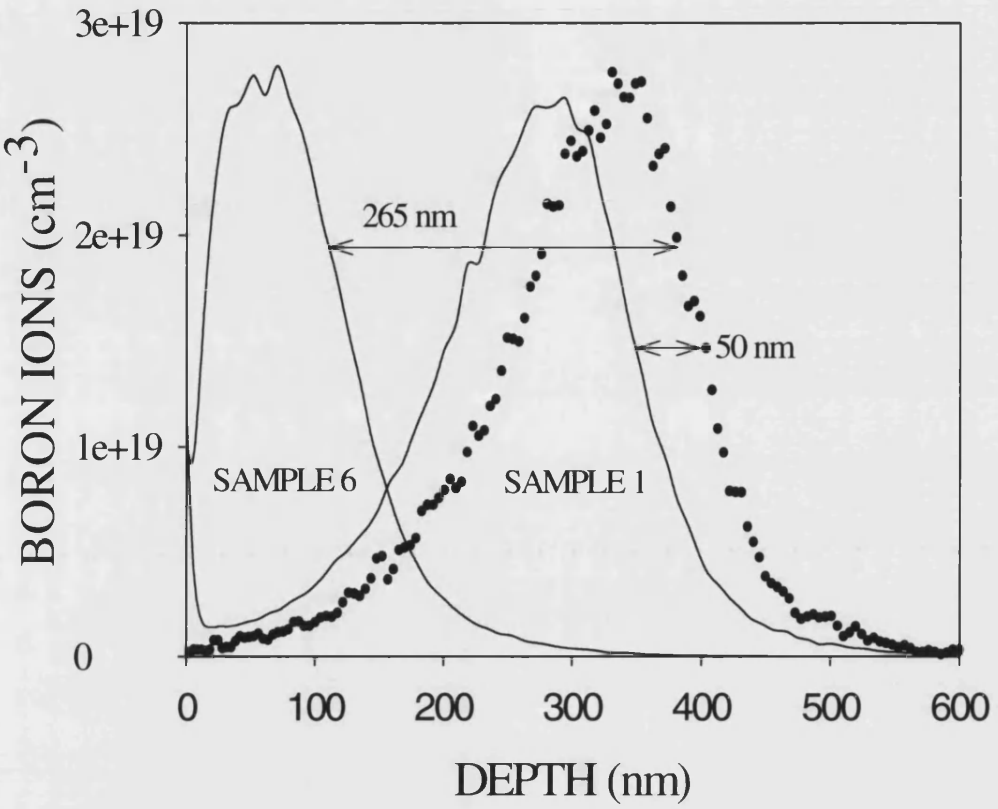

Figure (4.7) SIMS profiles for boron ions for s1 53nm and s6 261nm etch depths, together with the simulated profile. The equivalent etch depths suggested by these profiles are 50nm and 265nm respectively, which agree with the measured etch depths to within uncertainties in measurement. SIMS was performed at McMaster University, Ontario, Canada.

4.5.2 Anodic Oxidation

Anodic oxidation and etching was performed by M van Dyken at McMaster University, Canada, following the procedure described below.

Any native oxide layer on the sample is first removed by dipping in HF. The sample is then dipped into the electrolyte (e.g., 90% ethylene glycol, 0.4% KNO_3 and 10% water) and the voltage supplied between it (the anode) and the cathode immediately. This electrolyte is favoured as it can be used at room temperature, and gives more reproducible results and a more accurate calibration for thin oxide growth. The current density is approximately 12.5 mA cm^{-2}, thus requiring a 50mA current source for a 20x20mm sample. The electrolyte is constantly stirred to ensure uniform oxidation and is illuminated (often using a lamp and reflector) to enhance the anodic reaction. As the oxide grows the measured current decreases, and eventually stops when the applied potential can no longer pass current through the oxide layer. The equilibrium oxide layer thickness is therefore dependent on the potential V applied and, to a lesser extent, whether the Si is n- or p-type. The oxide thickness is measured by ellipsometry, and its variation across a 20mm x 20mm sample is typically ~10% (but can be as low as 2%). Typical results for oxide thickness are 35 nm for V = 60V and 60 nm for V = 100V. The oxide thus grown is then etched off by HF, and the procedure repeated as many times as required.

As mentioned previously an important point is that the anodic oxidation + etching process does not damage the sample surface to any extent measurable by positrons. This was checked by taking positron measurements on an unimplanted but etched sample. The results confirmed that the sample remained defect free despite the etching procedure.

4.6 Raw *S(E)* data and Corrections

The raw VEPAS data, together with VEPFIT results, are shown in figure (4.8). Data for samples s2, s4 and s6 are omitted to aid clarity. Each set of data was fitted individually with VEPFIT (solid lines in figure (4.7)). The depth of the damage box profiles given by VEPFIT decrease in accordance with the etch depths for samples s1-s7 (with the saturated defect *S* value of 1.04), and a deeper tail of defects is revealed for s8 and s9 –ie, beyond 400nm.

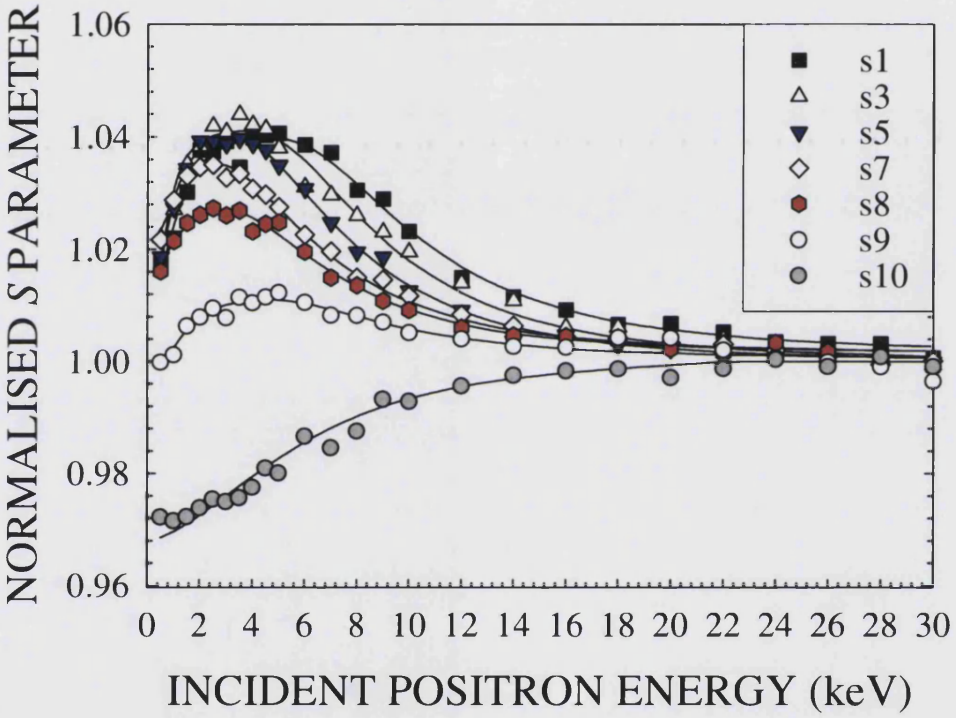

Figure (4.8) Normalised raw VEPAS data *S(E)* for etched samples 1-10 (data for samples 2, 4 and 6 not shown to aid clarity). Solid lines are VEPFIT fits to the data for samples 1-9; the solid line under data for sample 10 is a fit to data for unimplanted Si.

One feasible method for obtaining the full defect profile using VEPFIT is thus as follows:

(a) Set up ten layers corresponding to the etch depths,

(b) Fit the defect profile for layer 10 – i.e. for the most-etched sample,

(c) Fix the parameters for layer 10 and fit the profile for layers 9 and 10 – ie for the s9 data,

(d) Repeat this procedure until reaching s1, each time fixing the parameters obtained from the previous analysis.

In theory this procedure is reasonable for samples which do not exhibit saturation positron trapping; however, this is not the case here and when attempted it became immediately obvious that it is also beyond the scope of VEPFIT to handle the number of parameters required for such a method and still produce physical results. The numerous parameters had to be manipulated to such a degree that the VEPFIT output became arbitrary. This was especially true for the final few samples with up to 10 predefined defect boxes with fixed *S* parameters and diffusion lengths. Yet again one can confidently assert that the best VEPFIT can do is a square box profile for any one of the above samples. In a simpler system this method may work – namely, a non-saturated defect profile with not more than two or three etched layers.

4.6.1 Surface Value and Errors

The surface value is determined from the raw data and is key part of the calculation. It is therefore vital that the value used is as accurate as possible. A small difference in the surface value especially at low positron energies can have a significant effect on the results and be a major source for errors. For each sample a surface *S* parameter was measured to 3.d.p from the raw data by extrapolating to E=0keV with a straight line. Figure (4.10) shows this for s5, only data points up to 1.5keV are used in the extrapolation. In each case judgement was used as to the 'true' surface value and spurious points were neglected

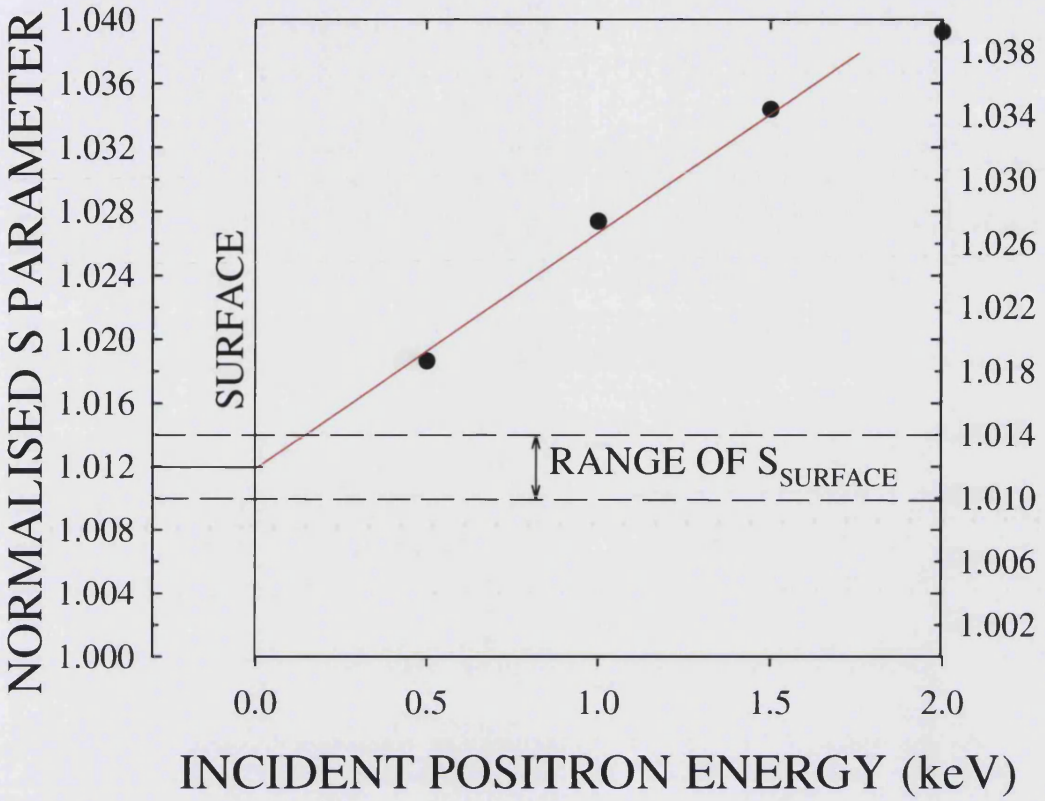

Figure (4.9) Example of $S_{SURFACE}$ determination for s5. (see table (4.1)) A straight line is drawn by eye through the first few points of the *S(E)* data and extrapolated to E=0 in order to obtain a value for $S_{SUFACE.}$ In this case the value of intersection is 1.012 but slightly different lines could have yielded a value anywhere between 1.010 and 1.014.

Once a value for $S_{SURFACE}$ is obtained an $S(C_D)$ plot was generated for each sample at each energy as demonstrated in Figure (4.6). In order to assess the effect of the surface value three lines were generated for each energy; one with the measured surface value and the other two with values slightly above and below that value see figure (4.10).

The range between the lowest and highest possible values of C_D ,ΔC was used as a basis for the weighted averages and error estimation. At low incident positron energies differences in the $S_{SURFACE}$ had a greater effect on the value of C_D and ΔC was bigger than at higher energies. It therefore seemed logical to use the

reciprocal of ΔC to weight the different contributions to C_D at the different energies. See equation (4.10)

$$C_{WEIGHTED\ AVERAGE} = \frac{\left(\frac{C_{(E=0.5)}}{\Delta C_{(E=0.5)}}\right)+\left(\frac{C_{(E=1.0)}}{\Delta C_{(E=1.0)}}\right)+\ldots}{\left(1/\Delta C_{(E=0.5)}\right)+\left(1/\Delta C_{(E=1.0keV)}\right)+\ldots} \qquad (4.10)$$

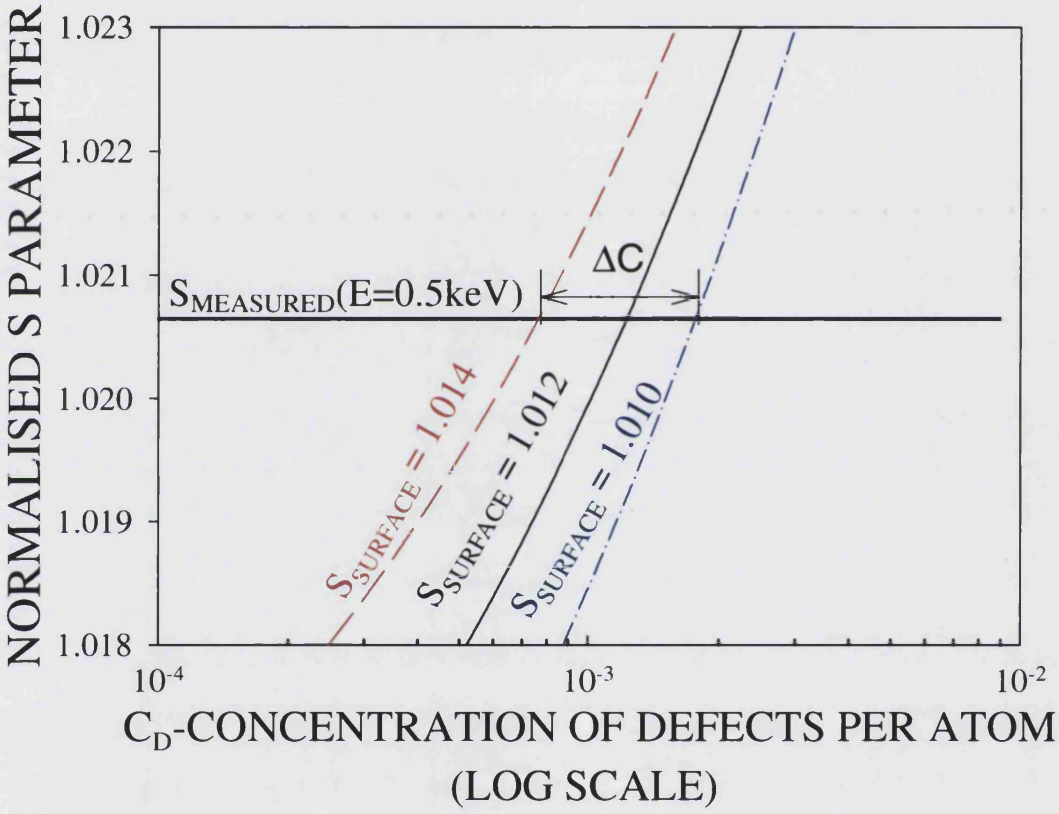

Figure (4.10) $S_{THEORY}(E=0.5keV)(C_D.)$ Generated theoretical $S(C_D)$ plots at 0.5keV for values of $S_{SURFACE}$ = 1.010, 1.012 and 1.014. The solid straight line is the measured *S* parameter for s5 at energy E= 0.5keV and has a value of 1.0206.

4.6.2 Notation

In order to avoid notational confusion with the different samples, energies, calculated defect concentrations and corrections the notation will be clarified here.

The samples are named s1 to s10 with a lower case "s" to avoid confusion with *S* - Parameters. The sample names and respective etch depths are presented in Table (4.1). Each calculated defect concentration is represented by C_{0_sN} or C_{1_sN}. The subscript sN refers to the sample as shown in Table (4.1) and therefore N has values from 1 to 10. The initial 0 or 1 in the subscript differentiates between corrected and uncorrected results with the zero referring to the initial results obtained and the one for the first order corrections. If there were further corrections these would be labelled 2, 3 and so on.

4.6.3 First Order Corrections

Initial values of defect concentrations were calculated using the method described in §4.4. This section is concerned with a first order correction to these values to allow for positrons implanted beyond the etch depth, ED and post implant positron diffusion. The primary aim is to determine what fraction of positrons end up annihilating in the adjacent region beyond the subsequent etch depth ED but contributing to the *S* parameter of the near surface region being scrutinised. Once this fraction is calculated then its contribution can be subtracted from the initial measurements to produce a first order correction. The stray positrons have two sources; initial implantation position which is straightforward to calculate and post implantation diffusion which is a more complex calculation. These fractions will be referred to as $F_{ED\_IMPLANT}$ and $F_{ED\_DIFFUSE}$ respectively with the sum of these being the total fraction called F_{ED}.

The method of computation involves the same equation (4.9) as used to calculate $F_{SURFACE}$, the fraction of positrons that diffuse to the surface. If the implantation profile is transformed from $P(z, E) \rightarrow P((ED-z), E)$ (where ED is the etch depth) and substituted into eqn (4.9) it will yield the fraction of positions that diffuse to beyond a depth of ED, $F_{ED\_DIFFUSE}$ and not the surface as before.

$$F_{ED\_DIFFUSE} = \int_0^{\infty} P(ED - z, E) e^{\frac{-z}{L_{eff}}} dz \qquad (4.11)$$

Figure (4.10) shows two implantation profiles for E=0.5keV with one normal, *P(z)* and one transformed, *P(53.33-z)* where ED =53.33nm. The arrows show the direction of positron diffusion.

To calculate the fraction of positions that are already beyond depth ED $F_{ED\_IMPLANT}$ simply requires solving an integral of the implantation profile with appropriate limits, equation (4.12):

$$F_{ED\_IMPLANT} = \int_{ED}^{\infty} P(z, E)\, dz \qquad (4.12)$$

The values of $F_{ED\_DIFFUSE}$ and $F_{ED\_IMPLANT}$ are calculated by the Maths algebra program MAPLE, and the sum of them, called F_{ED}, is used to correct the results.

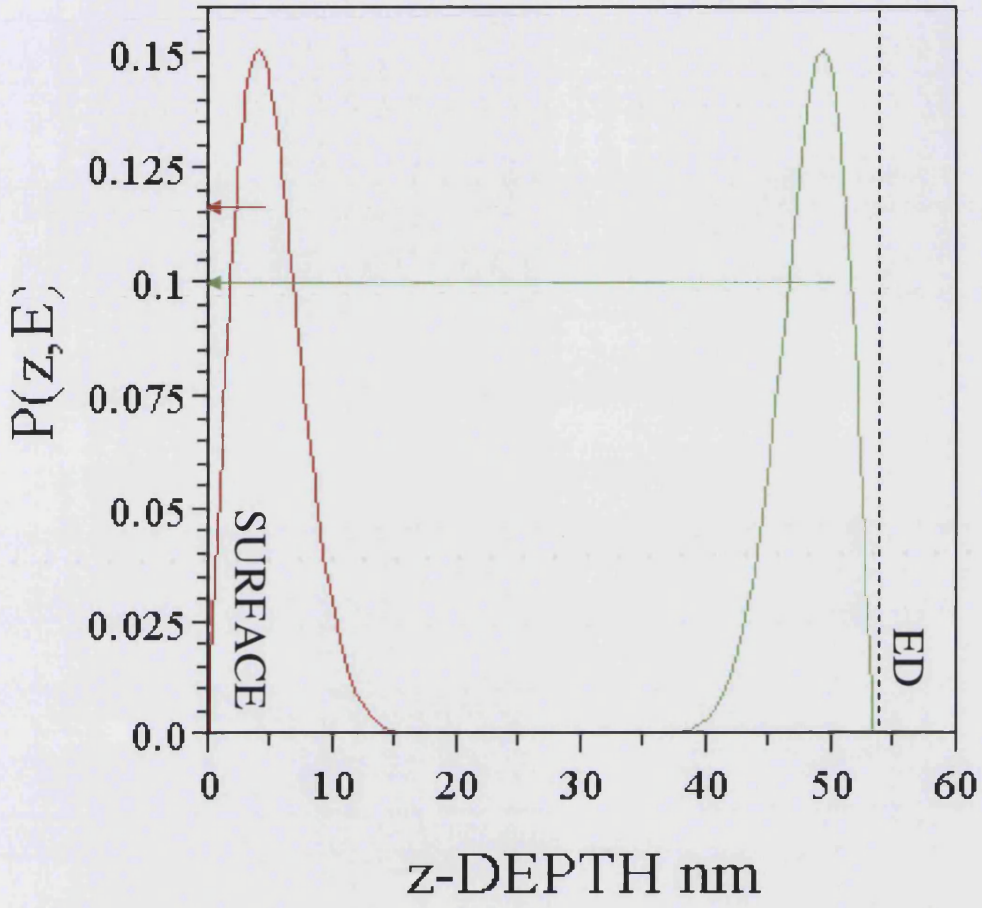

Figure (4.11) A MAPLE-generated graph of P(z,E) and for ED= 53.33nm and E=0.5. The red line is the original P(z, E) when used in eqn (4.9) it calculates what fraction of positrons diffuse to the surface, $F_{SURFACE}$, indicated by the red arrows. The green line is the red line transformed to P(ED-z, E). The dashed green line indicates the location of the surface in this transformed scheme. When eqn (4.9) is used with the transformed implantation profile the fraction of positrons diffusing to a depth ED into the material is calculated (F_{ED}). These positrons are represented by the green arrows.

The calculated value of F_{ED}, is is used in the following way to correct the results:

Of the total number of positrons entering a sample at a particular energy, E_i, a proportion *(x)* annihilate within the etch depth and a proportion *(1-x)* are either already there due to implantation or diffuse to and annihilate in the adjacent region (See figure (4.12)). Of course we now know that (1-*x*) = F_{ED}

This means that the concentration of defects initially obtained (C_{0_sN}) from $S_{MEASURED}$ has a contribution from the next layer. As a first attempt to correct for this we say that the following relationship holds for the first order corrected values for two adjacent layers (C_{1_sN}) and ($C_{1\_s(N+1)}$) and the uncorrected value (C_{0_sN}) of the layer nearer the surface:

$$C_{0\_sN} = xC_{1\_sN} + (1-x)C_{1\_s(N+1)} \tag{4.13}$$

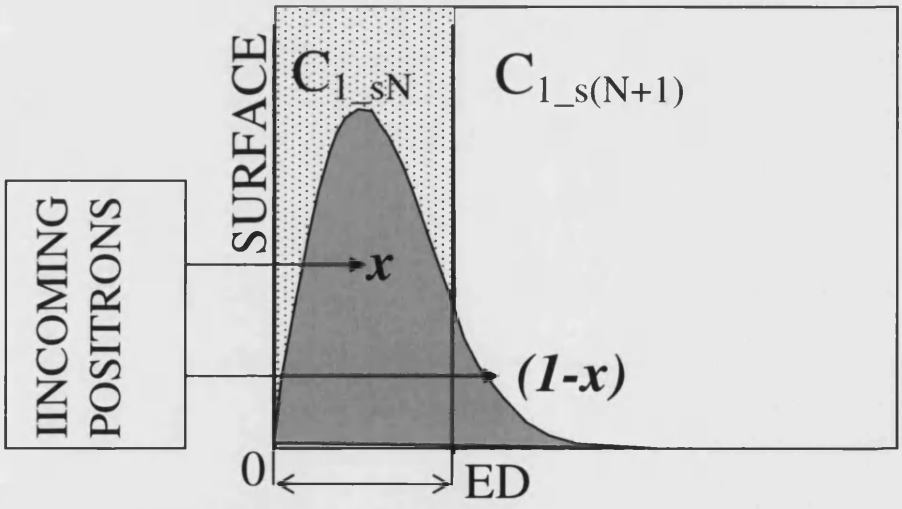

Figure (4.12) At each energy the implantation profile of the incoming positions will not be confined to the region of interest (Shaded region). A proportion (1-x) will end up annihilating in the adjacent layer either by initial implantation or subsequent diffusion. The proportion depends on the energy of the incident positrons and the thickness of the region of interest.

Sample s10 (Table (4.1)) had the most material etched off, 544.4nm, and by comparing the raw *S(E)* data to virgin silicon (shown in figure (4.13)) it was apparent that by this point all of the damaged region had been removed by the etching. The s10 data was fitted with VEPFIT as virgin silicon which produced a convincing fit when compared to the true virgin silicon. The two fits in figure (4.11) differ only in the surface value used.

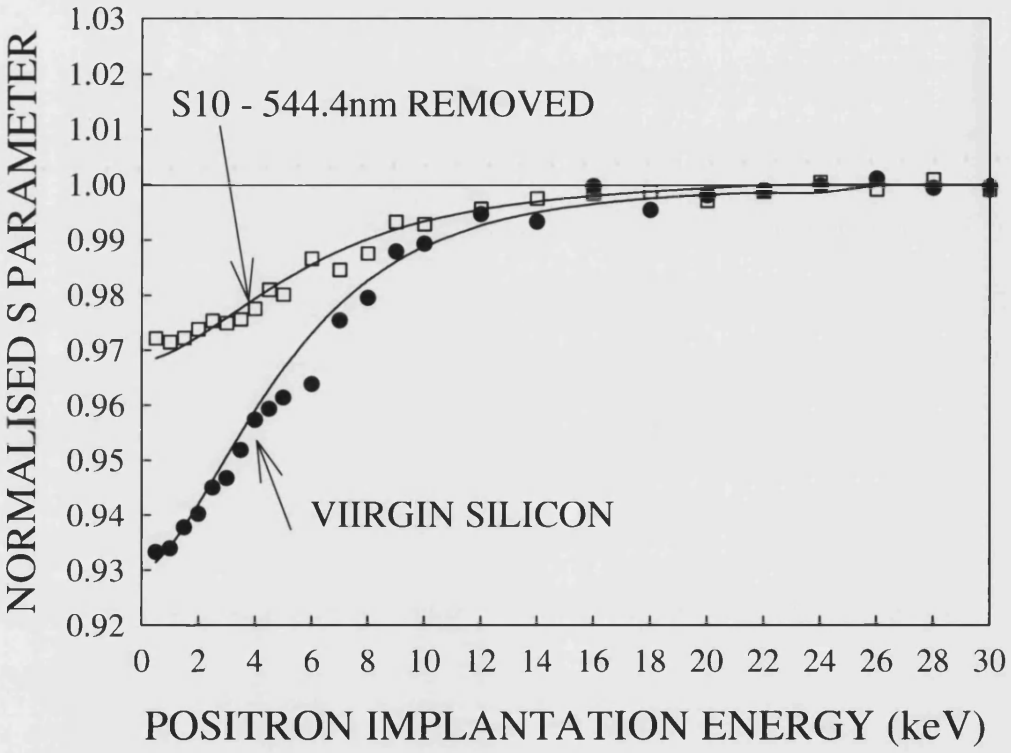

Figure (4.13) Normalised *S*(E) data for s10 (white squares)) and for virgin silicon (black circles). The solid lines are both fits for virgin silicon from VEPFIT with two different surface values.

As we now know s10 is effectively defect free it makes it the logical starting point for corrections. The first correction is simple and there is no need to calculate any diffusing fractions:

$$C_{0\_s10} = C_{1\_s10} = 0 \tag{4.14}$$

The second correction to s9 is not quite so simple but now is possible. By calculating $F_{ED\_DIFFUSE} + F_{ED\_IMPLANT}$ (=F_{ED}) for s9 (ED = 83.6nm) and therefore x for s9 which is called x_9:

$$x_9 = 1 - F_{ED} \tag{4.15}$$

Then:

$$C_{0\_s9} = x_9 C_{1\_s9} \tag{4.16}$$

As now C_{1_s9} is known it can be used with C_{0_s8} to calculate C_{1_s8}. This is continued with s7 and s6 etc until all the results are corrected.

$$C_{0\_s8} = x_8 C_{1\_s8} + (1 - x_8)\left(\frac{C_{0\_s9}}{x_9}\right) \tag{4.17}$$

On the whole the calculated fractions of positrons diffusing into the adjacent layer were small and therefore so were the corresponding corrections. Due to the high defect concentrations and correspondingly small effective diffusion lengths involved this first order correction probably wasn't necessary. However for lower defect concentration this could be a vital step in producing accurate defect profiles.

4.6.4 Summary of Analysis

(A) Each sample had the near surface region analysed corresponding to the depth of the *subsequent* etch. For example the first sample had 53.33nm etched off so this was the region of interest in the analysis of the unetched sample.

(B) For a range of realistic defect concentrations, C_D, theoretical $S(C_D)$ plots were generated for different values of $S_{SURFACE}$ and implantation energies ranging from 0.5keV to 2.0 keV.

(C) By comparing and matching the measured S parameter data with the appropriate theoretical values, (Energy and $S_{SURFACE}$ the same) C_D was computed for up to four energies depending on the depth of the *subsequent* etch.

(D) For every energy and sample a weighting factor was calculated using the uncertainly in the measurement of $S_{SURFACE}$. $S(C_D)$ plots were generated for values above and below $S_{SURFACE}$ to find the possible maximum and minimum values of C_D. The difference between these values was called ΔC.

(E) A weighted average was taken using the reciprocal of ΔC as a weighting factor.

(F) A first order correction was made to the results to account for positrons diffusing out of the region of interest and for those positrons initially implanted beyond the etch depth. The fraction of positrons in the adjacent region was calculated and the contribution of these positions to the initial calculations subtracted.

4.7 Final Results and Conclusions

The final defect profile obtained using the method and corrections described is shown in figure (4.14) (white circles) along with the simple box profile obtained from VEPFIT (blue dashed line) and scaled simulation data (red solid line). The simulations of the vacancy damage used the SSUPREM4 code [4.20] which simulates channelling but not post implant vacancy migration or agglomeration. The simulation results have been scaled down by a factor of 8. The tick marks on the horizontal depth axis correspond to the different sample etch depths and the vertical defect axis is a Log scale. It is particularly satisfying to note the good agreement between the shape of the simulation and the measurements obtained in the deep lying tail of the distribution over a range of three orders of magnitude.

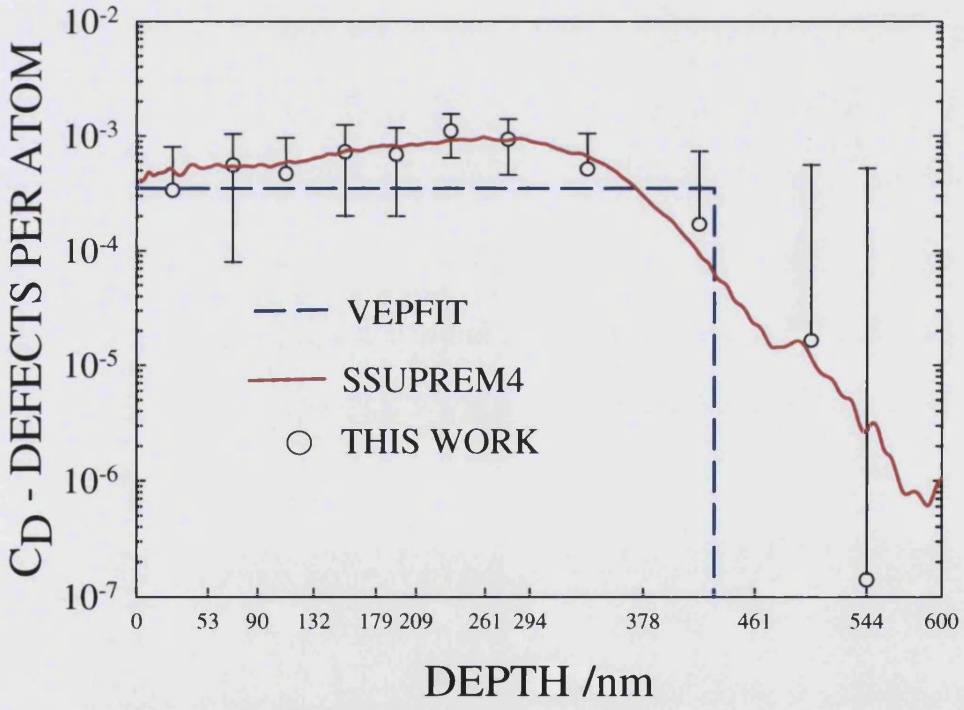

Figure (4.14) Defect concentration profile from: this work o , VEPFIT box profile, – – and the SSUPREM4 simulation—— multiplied by a factor of 0.125. Error bars result from weighted averaging and where not visible are within data points. From [4.21].

The similarity of the monovacancy distribution predicted by simulation and the observed distribution - expected to be primarily divacancies - is probably a result of the high migration energies of divacancies in Cz Si. Further work is underway to compare defect profiles in Cz with those in float-zone and epitaxially-grown Si implanted under similar conditions. The experimental technique and analysis procedure will be honed in light of the experience gained in this pilot study, and it is hoped that new information on the migration of vacancy-type defects in the three types of Si sample will be gained, especially in the deep tail region.

CHAPTER 5

VEPAS STUDIES OF $Pb(Sc_{0.5}Ta_{0.5})O_3$ AND $LaNiO_3$ THIN FILMS

5.1 Introduction

The following work is a collaboration between the University of Dundee, Qinetiq, and the slow positron group at the University of Bath.

An evaluation of oxide film thermal detector performance concluded that the constraining factors in performance were the materials used. A study into understanding the properties of different materials with potential in this application was being undertaken by David Keeble's Dundee group and Peter Wright at Qinetiq.

A series of perovskite oxides thin film samples were prepared by Metal Organic Chemical Vapour Deposition (MOCVD) and were the focus of the study. Vacancies, which positron techniques have a unique sensitivity to, are known to be the dominant type of point defects in perovskite oxides. Variable Energy Positron Annihilation Spectroscopy (VEPAS) allows near-surface depth profiling of vacancy type damage and therefore was one of the methods used to characterize the samples and study the effects of a Rapid Thermal Anneal (RTA).

The samples were studied and analyzed for their defect structure before and after rapid thermal annealing with the slow positron beam at Bath which is described in some detail in Chapter 2 and in [5.1]. The results were analyzed using VEPFIT [5.2] which gave an insight into changes in defect content of the films following rapid thermal annealing. A brief explanation of the background, method and results is given here with emphasis on the positron analysis.

5.2 Motivation and Background

A recent evaluation of thermal detector array performance concluded that the major limitation was currently the detector materials used [5.3]. Lead Scandium Tantalate, $Pb(Sc_{0.5},Ta_{0.5})O_3$ (PST) has a para-electric to ferroelectric phase transition close to room temperature and has been shown to have potential for high performance thermal detection. Metal Organic Chemical Vapour Deposition (MOCVD) has been used to grow PST giving improved detector performance [5.3], [5.4].

Device performance has been found to depend also on the nature of the electrode material used; conducting oxides have been found to be superior to platinum. Lanthanum nickelate, $LaNiO_3$ (LNO), has a simple perovskite structure and can be deposited by MOCVD. Post deposition annealing of LNO can reduce the resistivity to ~ 300 $\mu\Omega$cm.

To optimise the deposition of oxide multilayers feedback from both structural and electrical characterisation techniques is desirable. Characterisation by x-ray diffraction and electron microscopy may not provide sufficient sensitivity to allow electrical property variations to be correlated with structure.

In the studies presented here characterisation of PST, LNO and PST/LNO multilayers by Variable Energy Positron Annihilation Spectroscopy (VEPAS) is carried out. The method is non-destructive and by varying the energy of the implanted positrons response can be depth-profiled through thin-film structures.

Previous studies have shown the sensitivity of VEPAS for characterizing $Pb(Zr,Ti)O_3$ (PZT) structures [5.5][5.6]. It has also recently been used to study the vacancies created during different growth conditions of laser ablated thin films of strontium titanate ($SrTiO_3$) on $SrTiO_3$ [5.7]. It can provide insight on the presence of open-volume defects such as monovacancies, divacancies and small vacancy clusters, and is sensitive to oxygen deficiency [5.5][5.8].

5.3 VEPAS and Thin Films

The technique and apparatus of variable energy positron annihilation spectroscopy (VEPAS) is covered in some detail in Chapters 1 and 2. The benefit of using VEPAS in this situation is because vacancies are known to be the main defect type which the method is very sensitive to. Also thin films are involved and depth profiling is required which is another strength of the technique. In all the cases so far the analysis has been based on much examined materials like ion implanted doped silicon with well known parameters such as defect type, defect trapping rate, bulk S parameter, defect S parameters and so on. The following paragraph summarises the technique where none of these things are known and how the analysis proceeds as a result.

A defect-free material is characterised by a specific, material dependent, value for the S parameter, S_{BULK}. Introduction of a positron trapping vacancy defect will cause an increase in the measured S Parameter, $S_{MEASURED}$, with increasing defect concentration. As the concentration is increased, a point is reached at which all the implanted positrons are trapping at, and annihilate from, the vacancy defects; this condition is termed *saturation* trapping. The value of $S_{MEASURED}/S_{\mathrm{BULK}}$ ratio will tend to a saturation value $S_{\mathrm{DEFECT}}/S_{\mathrm{BULK}}$ characteristic of the particular defect.

The magnitude of the saturation $S_{\mathrm{DEFECT}}/S_{\mathrm{BULK}}$ increases with the size of the open volume defect [5.9]. The defect concentration, $C_D(SATURATION)$, at which saturation trapping occurs depends on the defect specific trapping rate, μ_{DEFECT}; again a characteristic of the particular defect, the trapping rate of positrons to the defect which is given by $\kappa_{DEFECT} = \mu_{DEFECT}\, C_D$. Vacancy defects with a larger defect specific trapping rate, for example defects with negative local charge or larger open volume, will show saturation trapping at smaller values of C_{D}.

5.4 Experimental Procedure

5.4.1 The Samples

The samples were grown by MOCVD, details of which are given in [5.4] and [5.10]. The samples and their deposition conditions are tabulated in table (5.1) but are also briefly described here.

Three samples were created by growing a film of thick lanthanum nickel oxide, $LaNiO_3$, (LNO) on thermally oxidised silicon (SiO_2/Si) in three different sets of deposition conditions. One of these sets was then used as substrate and six further samples were created by growing films of lead scandium tantalate, $Pb(Sc_{0.5}Ta_{0.5})O_3$, (PST) in different conditions. Additionally each sample was subject to a Rapid Thermal Anneal (RTA) of 750°C for 600s for the LNO/SiO_2/Si samples and 850°C for 120s for the PST/LNO/SiO_2/Si. The total number of samples was eighteen.

The listed film depths are the designed and not the actual. From TEM and SEM analysis the actual PZT depths are about 50% bigger than designed and the LNO are about 2.5x the design thickness [5.11].

Table (5.1) Sample descriptions of deposition conditions and film thicknesses . Bracketed numbers are the design thicknesses. The actual figures were confirmed with TEM and SEM analysis [5.11].

Sample Name	Film	Substrate	Film Thickness	Temperature	During Deposition		Post Deposition	Rapid Thermal Anneal
CVI 295	Thick Lanthanum Nickel Oxide $LaNiO_3$ (LNO)	Thermally oxidised silicon SiO_2/Si	2.5 μm LNO (1.0μm)	Standard temperature	100 cc/min Oxygen	400cc/min Helium	/	600s @750°C
CVI 296				Standard temperature	250cc/min Oxygen	250cc/min Helium	/	
CVI 297				Standard temperature	250cc/min Oxygen	250cc/min Helium	Kept at deposition temp in Ozone for 1 hr cooled slowly in ozone	
CVI 307	Lead Scandium Tantalate $Pb(Sc_{0.5}Ta_{0.5})O_3$ (PST)	LNO deposited on thermally oxidised silicon in the deposition conditions of CVI 295	450nm PST (300nm)	630°C	250cc/min Oxygen	400cc/min nitrogen	/	120s @850°C
CVI 308				630°C	100cc/min Oxygen	250cc/min nitrogen	/	
CVI 309				630°C	250cc/min Oxygen	250cc/min nitrogen	Annealed in Ozone at deposition temp for 1 hour	
CVI 310				740°C	100cc/min Oxygen	400cc/min nitrogen	/	
CVI 311				740°C	250cc/min Oxygen	250cc/min nitrogen	Annealed in Ozone at deposition temp for 1 hour	
CVI 312				740°C	250cc/min Oxygen	250cc/min nitrogen	/	

5.4.2 VEPAS Experiments

Positron annihilation measurements were performed using the monoenergetic positron beam at the University of Bath [5.1]. The incident positron energy was varied over the range 0.5–30 keV and the Doppler broadened energy spectra of the annihilation radiation recorded for each implantation energy. Each Doppler broadened spectrum contained approximately 1×10^6 annihilation events and was characterized by the *S* and *W* parameters. The variation in the *S* parameter as a function of *E* was analysed using the Variable Energy Positron Fit (*VEPFIT*) program. Analysis of VEPAS data for different energies, and hence depths, is achieved by splitting the material into a series of intervals. For each interval the *VEPFIT* program determines the fraction of positions which annihilate at a given depth of a material and the corresponding *S* parameter is calculated. The change in *S* parameter following the Rapid Thermal Annealing (RTA) is what is of interest here.

5.5 Results and Discussion

The *S(E)* data presented here is as measured (un-normalised) and uses the 'old' region of interest limits to define the *S* parameter. This make the Doppler spectrum central region ~ 0.5 and the wings ~0.25. See §1.5.2 for further explanation.

From data taken at the time the bulk *S* parameter silicon was measured to be ~0.486. All the data was fitted using VEPFIT to determine the *S* parameters for each PST or LNO film before and after Rapid Thermal Annealing (RTA). The LNO/SiO_2/Si samples were modelled as three layers; LNO, bulk silicon and an interface layer between them of SiO_2. The PST/LNO/SiO_2/Si samples were also fitted with three layers; PST, LNO and an interface layer. The film thicknesses were deep enough in the PST/LNO samples that there was no need to include the silicon substrate or the SiO_2 layer as an insignificant proportion of positrons would have penetrated this far through the dense PST and LNO films. Also, the implantation profile would be too spread out at this point to distinguish these deep layers.

Some of the data was fitted without the first few surface values to simplify the fitting procedure. The results of the fitting are summarised in the bar chart of Figure (5.7). The following sections present and discuss the raw *S(E)* data.

5.5.1 LNO Films

The raw *S(E)* data for CVI 295,296 and 297 is shown in figure (5.1). These are the simplest samples with a layer of LNO deposited on thermally oxidised silicon in a variety of conditions.

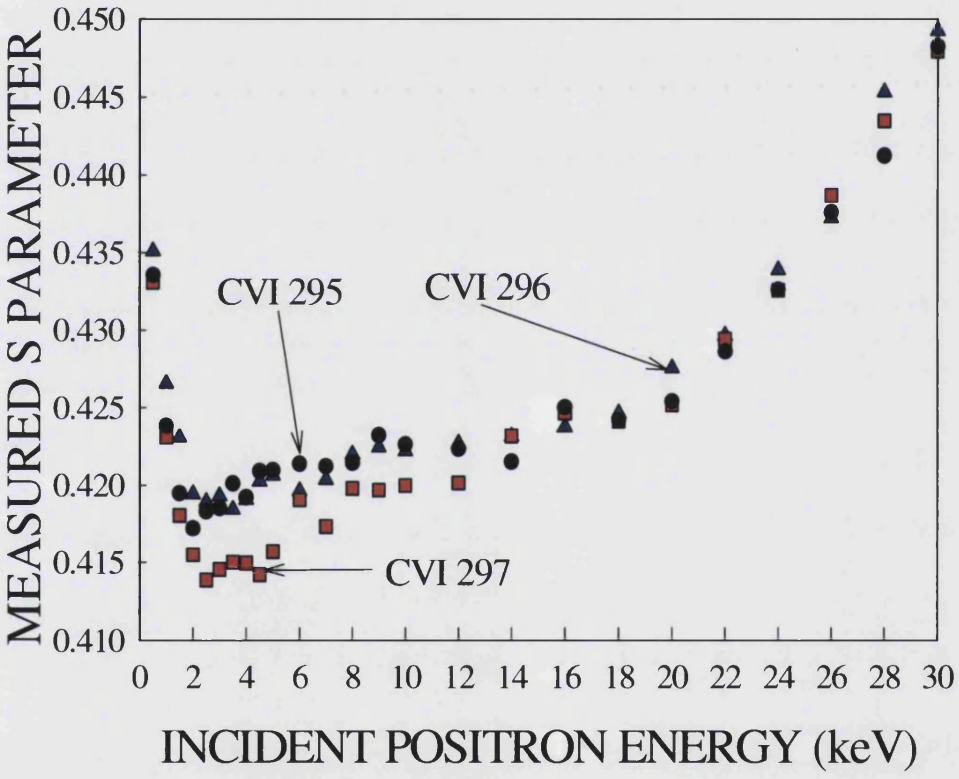

Figure (5.1) Raw *S(E)* data for: CVI 295 (●), CVI 296 (▲) and CVI 297(⊡).

These results clearly show that all three samples have a surface *S* of ~0.436 which is higher than the film (LNO) layer and consequently pulls up the measured S parameter at low energies (< 2 keV). The depth of the LNO layer is known to be approximately 2500nm, after which it is thin layer of silicon oxide and then bulk silicon. The bulk silicon *S* parameter is higher than the LNO film and from previous measurements has a value of ~0.484. Only the highest energy positrons

that have the tails of their implantation profiles beyond 2500nm and the positrons that can diffuse this far are 'seeing' this higher *S* parameter. The contribution of these positrons increases the measured *S* parameter as the energy increases from about 20keV onwards. The bulk *S* parameter of silicon is never directly measured because even at the highest energy (30keV) only a proportion of the positrons are annihilating in silicon (~ 40%). Figure (5.2) shows the implantation profiles and mean implantation depths of 26keV and 30keV positrons in LNO. Because LNO has a higher density (5.1 gcm^{-3}) than silicon (2.3 gcm^{-3}) the positrons have much smaller mean penetration depths. For example at 30keV the mean penetration depth in silicon is ~ 4μm but in LNO this is less than half this at ~1.8μm.

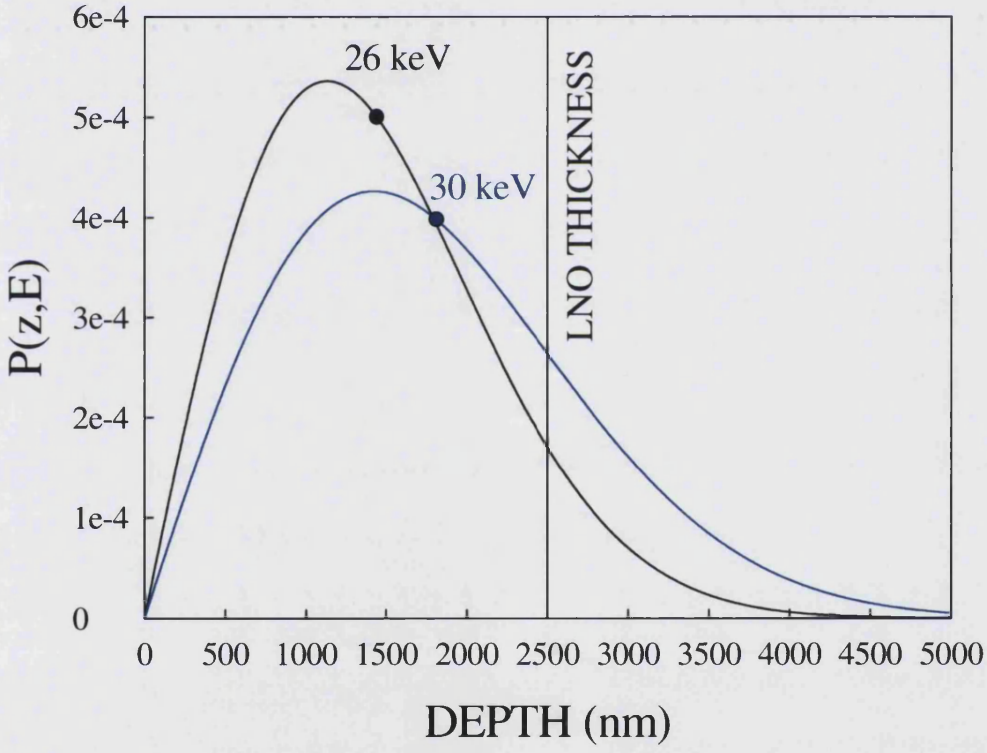

Figure (5.2) Implantation profiles of 26keV and 30keV positrons in LNO which has a density of 5.1 gcm^{-3}. The thickness of the LNO is known to be 2500nm and only ~20% of the 30keV positrons implanted initially penetrate this layer. Post-implant diffusion means that ~ 40% eventually decay in the Si.

The LNO film S parameter is probably measured directly in the region of 8- 14 keV where most of the positrions annihilate within it. This gives an S parameter of ~ 0.423 for the LNO film. This was confirmed with fitting which is discussed later on.

Of the three samples the CVI 295 and CVI 296 are very similar which shows that the differences in their deposition conditions had little effect on the resulting films. However CVI 297, which was kept at the deposition temperature in ozone for one hour and cooled slowly, has a lower near surface *S* parameter which suggests the presence of oxygen which may have been introduced during the annealing or cooling in ozone.

As it is the CVI 295 that is used as a substrate for the PST growth it is only for this sample that we will examine the effect of the Rapid Thermal Annealing (RTA) on the *S(E)* response. Figure (5.3) is the *S(E)* data for the annealed and as grown samples.

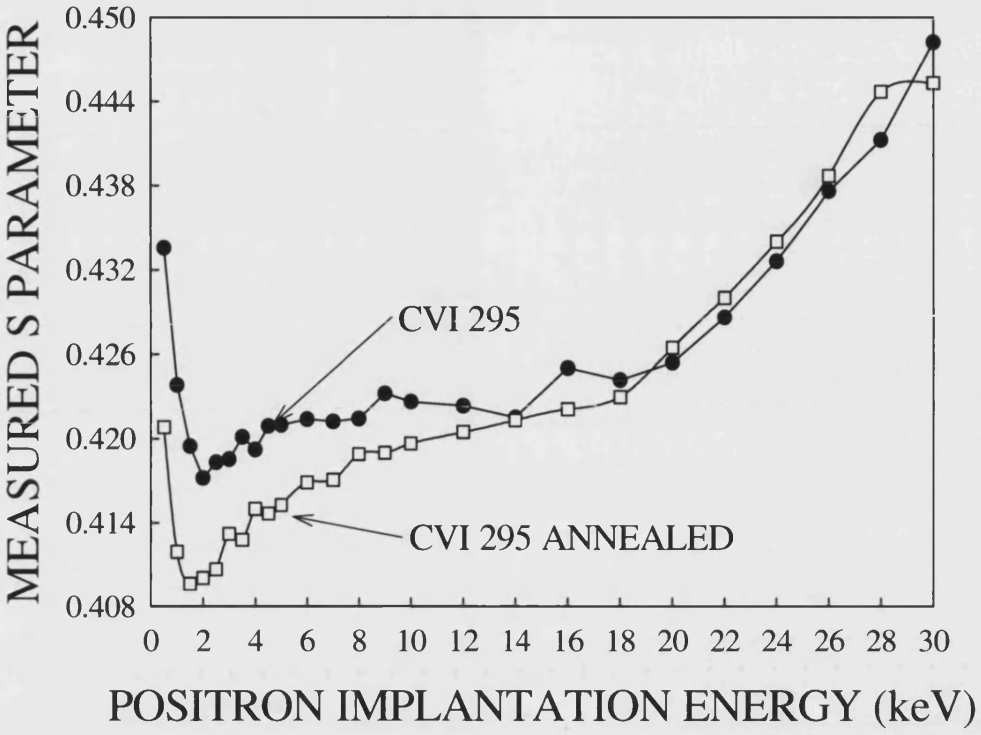

Figure (5.3) The *S(E)* data for sample CVI 295 before and after the Rapid Thermal Anneal (RTA).

At the higher energies the *S* parameter is increasing toward the bulk silicon value and at lower energies the surface *S* parameter is dominating. Again it is within the medium range of energies that we can glean information directly from the raw data about the LNO film. We can see that the LNO *S* parameter has decreased a small amount and now has a value of ~0.418. Again this was confirmed with fitting. The drop in the *S* parameter at low energies after annealing is probably due to a fall in the surface *S* value seen by thermalised positrons (the sharp increase in *S* below ~ 1.5 keV is probably due to epithermal positrons leaving the surface and forming positronium), possibly coupled with an increase in the positron diffusion length in the film.

5.5.2 PST/ LNO films

These samples were more complicated to analyze because of the third layer of PST on the LNO/silicon substrate. The *S* parameters were fitted by VEPFIT for both layers for the as grown and annealed samples. The response to the RTA varied a great deal depending on the sample. Roughly the samples divided into two 'groups'; one which showed a significant change in *S(E)* response post RTA and those for which the annealing had little effect on the *S* parameter other than at the surface. The samples of CVI 309, 310 and 311 were in the latter group with minimal *S(E)* change post RTA. Figure (5.4) shows the *S(E)* response before and after RTA for these samples.

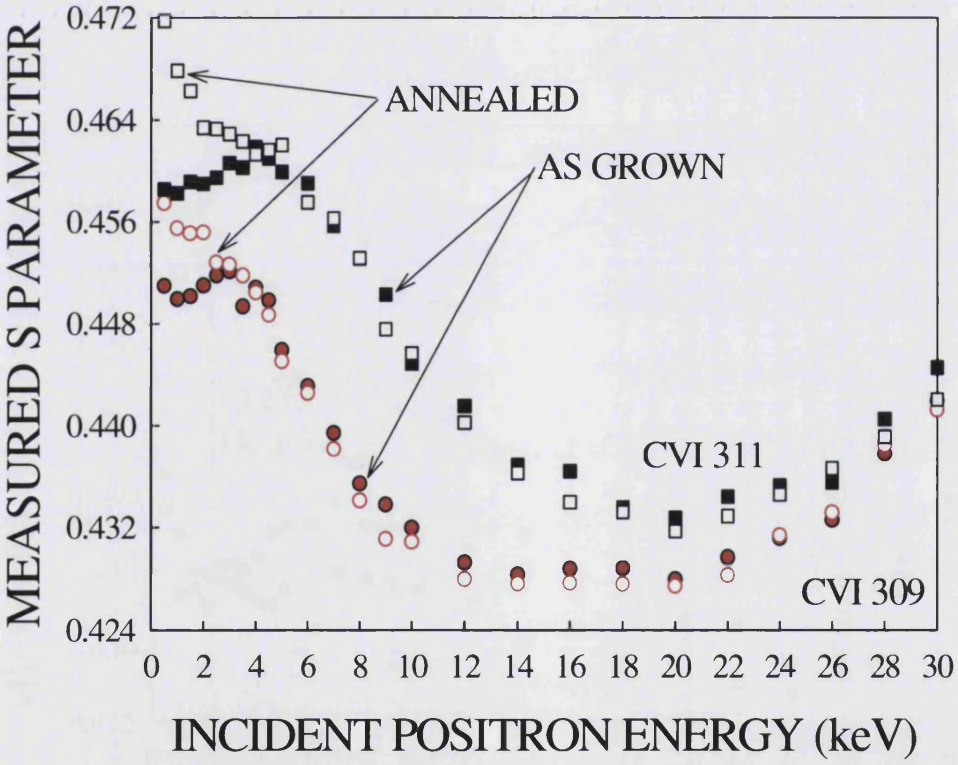

Figure (5.4) *S*(E) response for CVI 309 and CVI 311 before and after Rapid thermal annealing (RTA). The CVI 10 response is very similar and omitted for clarity.

This suggests that for these samples the effect of annealing was simply to remove a layer of oxide that had formed on the surface since deposition and the bulk structure remained unaffected by the RTA. The presence of oxygen lowers measured *S* parameters [5.12] due to the higher momentum of the oxygen electrons; once removed the effect is to increase the measured surface *S* parameter.

The samples in the former 'group' that exhibit a change in *S(E)* response post RTA were CVI 307 and CVI 308. The difference was pronounced and indicated actual changes in the *S* parameters of the films. Figure (5.5) is the *S(E)* response for these two samples before and after the RTA.

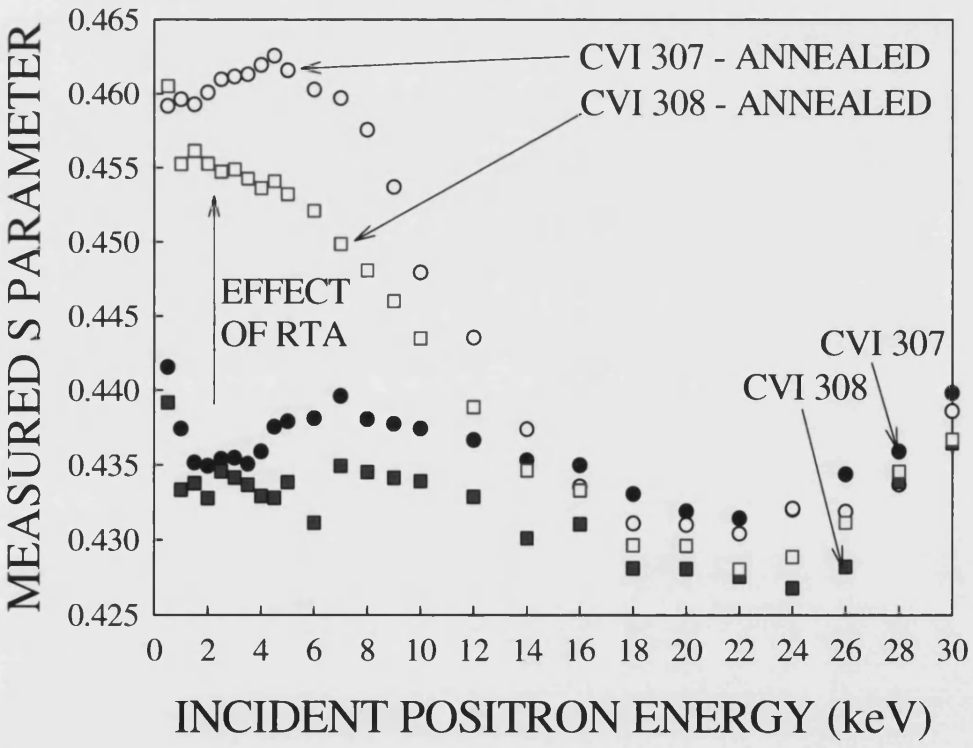

Figure (6.5) *S(E)* response for CVI 307 and CVI 308 before and after Rapid Thermal Annealing. (RTA)

These results show that the effect of the RTA is to increase the measured *S* parameter in the near surface region. This suggests annealing out of oxygen related defects as the presence of oxygen has the effect of lowering the *S* Parameter. Fitting confirmed that the changes of the *S* parameter only occurred in the PST film of each sample and the *S* Parameters in the LNO film remained the same.

Comparing the deposition conditions of the samples with the significant *S(E)* response post RTA (CVI 307-308) and the no response samples (CVI 309-311) reveals possible causes of the differences detected by the positron response.

The CVI 307-308 were grown at a lower deposition temperature (630°C) compared to the 'no response' CVI 310-311 (740°C). It is possible that the lower deposition temperature resulted in more defects being created in the process or prevented annealing of defects. Hence the lower temperature deposition samples had more defects that could be annealed which was observed following the RTA. This change was not observed in CVI 310-311 samples because there were no defects present to anneal out during RTA.

However CVI 309 was also grown at the lower deposition temperature and did not show a change in the *S(E)* response after RTA. This could be due to the fact that after growth it was kept in ozone at the deposition temperature for one hour. It is plausible that during this time the defects introduced in the growing process were able to anneal out even at the lower temperature. This data suggest that keeping a sample at 630°C for one hour post deposition is equivalent to growing at 740°C in terms of the defects introduced/present that are visible to positrons

Sample CVI 312 showed a response that was between the two 'groups' described above. The as grown data was very like that of CVI 310 but not after Rapid Thermal Annealing. CVI 310 only exhibited a surface change like CVI 309 and CVI 311 probably due to the oxide layer being removed by the RTA but CVI 12 showed a definite drop in *S* parameter in the PST film. This was confirmed by fitting. Figure (5.6) show the *S(E)* data for CVI 310 and CVI 312.

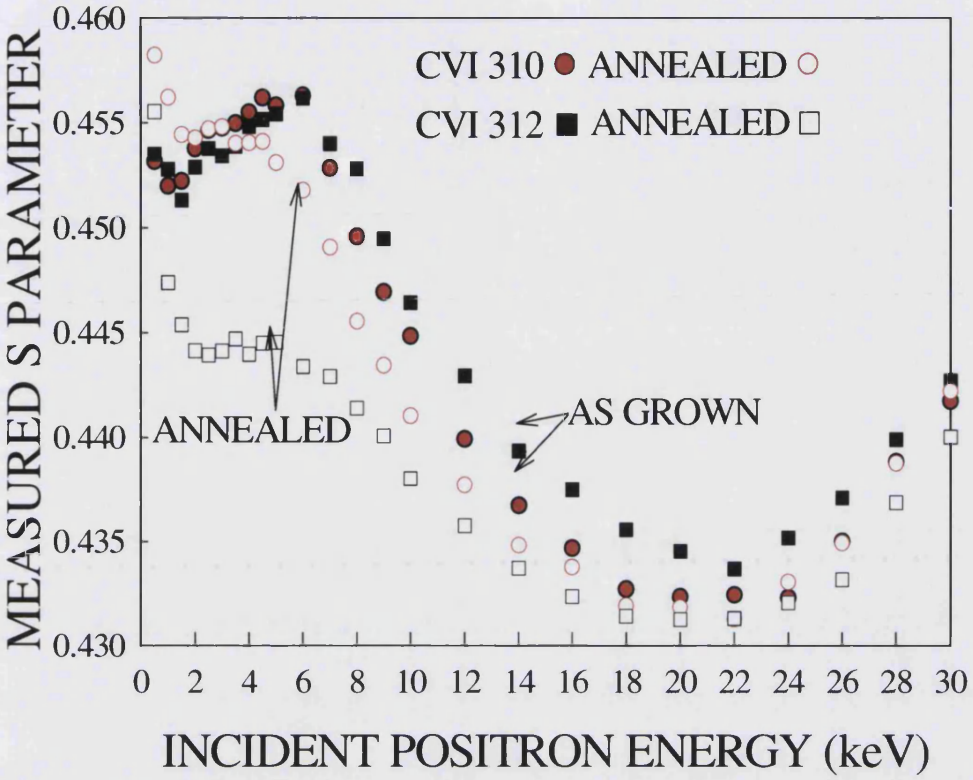

Figure (5.6) *S*(E) response for CVI 310 and CVI 312 before and after RTA.

The only difference between the CVI 310 and CVI 312 were the proportions of gases during deposition. This decrease in *S* Parameter could be due to vacancies with no oxygen involved. Why these would be present in CVI 312 but none of the other samples, especially CVI 310 which has the most similar deposition conditions, is not clear.

5.5.3 Summary of VEPFIT Results

Figure (5.7) is bar chart of the fitted results for the films in each sample obtained using either a three layer model and the thicknesses as given by table (5.1)

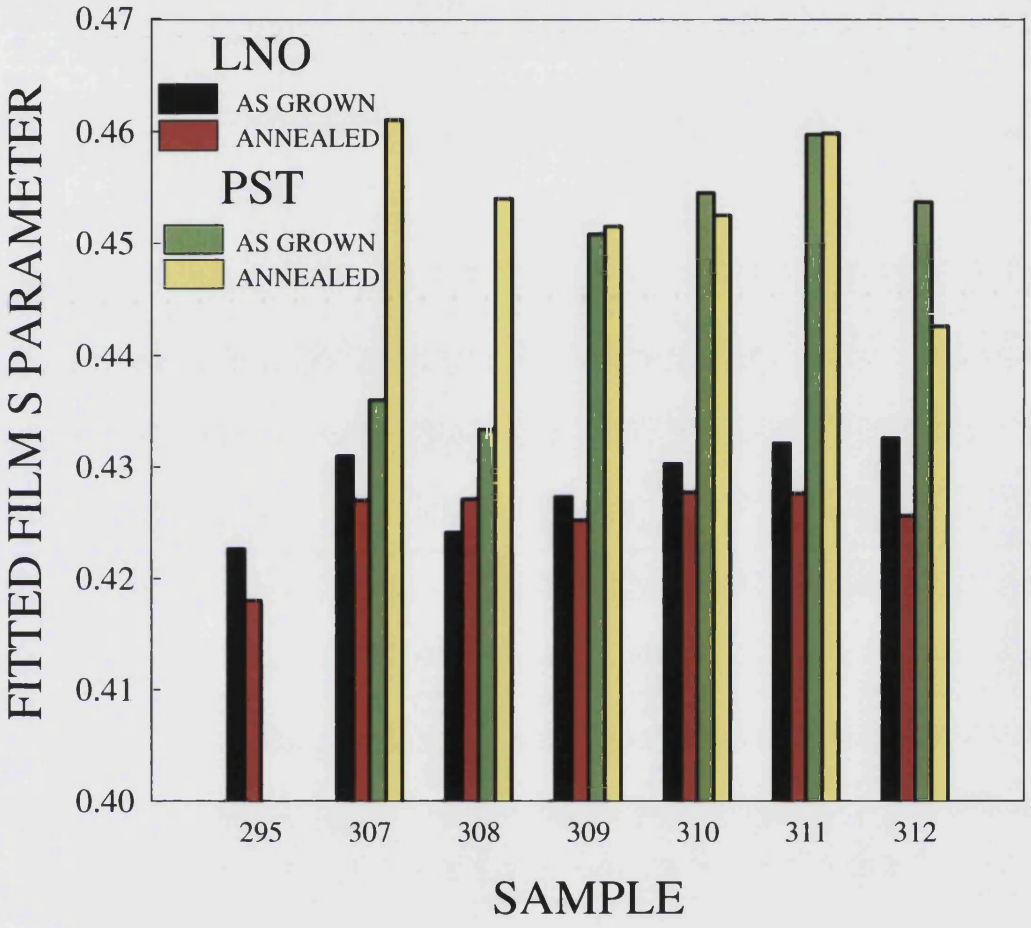

Figure (5.7) Summary of VEPFIT results. Each bar represents the fitted *S* parameter of a film in a sample either before or after Rapid Thermal Annealing (RTA).

5.6 Conclusions

For all the samples the *S* Parameter of the LNO film is relatively unaffected by Rapid Thermal Annealing (RTA).

For samples CVI 307 and CVI 308 the *S* parameter increases significantly in the PST layer after RTA. For CVI 309, CVI 310 and CVI 311 the only effect of the RTA is to the measured surface *S* Parameters which is most likely due to the surface oxide layer being removed by the RTA. The fitted results confirm that the PST and LNO films do not undergo a detectable change in layer *S* parameters.

The two samples that underwent a biggest *S* Parameter change post RTA (CVI 307 and CVI 308) were both grown at the lower deposition temperature of 630°C. Whereas out of the three that didn't change after RTA (CVI 309 CVI 310 and CVI 311) two were grown at the higher deposition temperature of 740°C. Sample CVI 309 which was grown at the lower temperature but exhibited behaviour like the 740°C samples was actually kept at the deposition temperature in ozone for a further hour after growth. This is the main difference between these samples and indicates that defects introduced during growth can be minimised by either growing at a higher temperature, 740°C or by keeping the sample at the lower temperature of 630°C after deposition for one hour.

CVI 312 is an odd one out as it exhibited a decrease in *S* parameter post RTA indicative of plain vacancy type damage free of any oxygen. However none of the other samples showed this type of damage and CVI 310 was made in very similar conditions. The reasons for this are not clear.

FINAL CONCLUSIONS

The focus of this thesis was on three separate studies: Direct observation of monovacancies, step etching to enhance depth resolution and characterisation of thin ferromagnetic films. This final section aims to briefly summarise the aims, achievements and conclusions of each study.

In the quest to directly observe monovacancies it was necessary to depart from the usual experimental procedure involved in positron experiments. Damage needed to be created *in situ* at temperatures below 100K and this temperature maintained for subsequent positron measurements.

The VEPAS results taken between 60K and 300K of the silicon implanted at low 60K with 6 keV Helium showed a damage peak at 2.5 keV. However this peak did not change with temperature as would be expected for monovacancies gradually annealing out to divacancies. This lack of change could be because the monovacancies recombined and agglomerated forming the exact proportion of divacancies that would produce the same *S* parameter. However estimates of the quantities necessary make this unlikely. It may also have been due to decoration of the vacancies by the implanted ions which would influence trapping rates however again the numbers involved are too small to make this a real possibility. The most likely explanation is either that the sample was not in thermal contact with the cold finger at the time of implantation or that the damage caused the sample to become amorphised and it could not be recrystallised at 300K .

From the data obtained it is difficult to draw quantitative conclusions regarding the evolution of monovacancies to divacancies. However, the progress made here into the development of the technique enabled further work to be carried on the activation energies by studying the changes *S* Parameter in the peak as a function of time at a set temperature and this work is continuing.

Traditional VEPAS is a technique capable of profiling damage depth distributions while leaving the sample intact. Due to the spreading out of the positron implantation profile at higher energies there is a loss of resolution with depth. In

order to try and reduce this loss of resolution it was necessary to lose the none destructive nature of the procedure and progressively etch the sample bringing deeper lying damage to the surface.

The sample used was wafer of Cz silicon implanted with 100 keV B^+ ions at a dose of 5 $x10^{14}$ cm^{-2}. The wafer was divided into 10 pieces each of which had a different depth etched off via anodic oxidation. Each sample had VEPAS measurements taken and a new analytical method was used to obtain a defect concentration of roughly the first 50nm. These were then pieced together at the relevant depths to construct a depth profile of the damage. This was compared to Monte Carlo simulations and the profile obtained from only the unetched sample. There was a good agreement between the shape of the simulation and the measurements obtained in the deep lying tail of the distribution over a range of three orders of magnitude. The similarity of the monovacancy distribution predicted by simulation and the observed distribution - expected to be primarily divacancies - is probably a result of the high migration energies of divacancies in Cz Si.

Further work is underway to compare defect profiles in Cz with those in float-zone and epitaxially-grown Si implanted under similar conditions. The experimental technique and analysis procedure will be honed in light of the experience gained in this pilot study, and it is hoped that new information on the migration of vacancy-type defects in the three types of Si sample will be gained, especially in the deep tail region.

A series of samples of interest to the University of Dundee and Qinetiq due to their possible application in thermal imaging were analysed using VEPAS. The *S* parameters of the samples, a series of ferromagnetic thin films grown at different temperatures in the presence of different gas mixtures before and after Rapid Thermal Annealing, were measured and compared. It was attempted to try and determine which growth factors influenced the vacancy content of the films the most by looking at the changes before and after the RTA.

As the S Parameters of the samples that were grown at higher temperatures or kept at growth temperature for a period afterwards were relatively unaffected by the RTA it was concluded that these samples had little vacancy content as they had opportunity to anneal. The samples grown at lower temperatures with no post growth incubation showed the biggest change in S Parameter before and after RTA which suggests that there were vacancies present which then annealed. One of the samples grown in similar circumstances does not conform to either of the above scenarios the reasons for which are not clear.

This study showed the potential of VEPAS to be used as a routine characterisation method for materials other than ion implanted silicon.

REFERENCES

CHAPTER 1

[1.1] C.D. Anderson, "The Positive Electron", *Phys. Rev.*, **43**, p491 (1933)

[1.2] P.A.M. Dirac, Proc. *Camb. Phil. Soc.*, **26**, p361 (1930)

[1.3] P.J. Schultz, K.G. Lynn, *Rev. Modern. Phys.*, **60**, pp701-779 (1988)

[1.4] W. Cherry, *Ph.D Thesis*, Princeton (1958)

[1.5] D.G. Costello, D.E. Groce, D.F. Herring, J. Wm. McGowan, *Phys. Rev. B*, **5**, 1433–1436 (1972)

[1.6] P.G. Coleman, ed, *Positron Beams,* World Scientific, (2000)

[1.7] E. Chason, S.T. Picraux, , J. M. Poate, J. O. Borland,. M.I. Current, T. Diaz de la Rubia,, D. J. Eaglesham, O. W. Holland , M.E. Law , C. W. Magee, J. W. Mayer , J. Melngailis, A. F. Tasch, *J. Appl. Phys.* **81** p6513. (1997)

[1.8] A.P. Mills, 'Positron Annihilation', P.G. Coleman, S.C. Sharma, L.M. Diana, eds., North Holland, Amsterdam, p121, (1982),

[1.9] D. A. Fischer, K. G. Lynn, D. W. Gidley, *Phys Rev B*, **33**, 4479 (1986)

[1.10] Positrons in solids, P. Hautojärvi, ed. Springer-Verlag Berlin Heidelberg, (1979)

[1.11] R.H. Howell, I.J. Rosenberg and M.J. Fluss, *Phys. Rev. B*, **34,** 3069 (1986)

[1.12] A.P. Knights, P.G. Coleman, Surf. Sci. **367**, 238 (1996)

[1.13] O. Jenson, A.H. Walker, *AIP conf proc*, **218**, p44 and p19

[1.14] A.F. Makhov (1961): *Sov. Phys Sol. State*, **2** (1934)

[1.15] R. Krause-Reyberg, H.S. Leipner, Positron Annihilation in Semiconductors, Springer, (1998)

[1.16] A. Vehanen, K. Saarinen, P. Hautojärvi, H. Huomo, *Phys. Rev. B,* **35**, p4606 (1987)

[1.17] A.P. Mills Jr, R. Wilson., *Phy. Rev. A,* **26**, 490 (1982)

[1.18] S. Valkealahti, R.M. Nieminen , *Appl. Phys. A*, **35,** 51-59(1984)

[1.19] O. Jenson, A.H. Walker, *Surf. Sci.* **292,** 83-97 (1993)

[1.20] V.J. Ghosh, G.C. Aers, *Phys Rev B*, **51**, 45 (1995)

[1.21] A van Veen, H Schut, J de Vries, RA Hakvoort and MR IJpma, *AIP Conf. Proc.*, **218** 171 (1990).

[1.22] X.D Pi, C.P. Burrows, P.G. Coleman, *Appl. Surf. Sci.*, **194**, pp 255-259, (2002)

[1.23] P. Hautojärvi, H. Huomo, J. Lahtinen, J.Mäkinen, A. Vehanen, *Mat. Sci. Forum,* **10-12**, 527, (1986)

[1.24] .J. Schultz, E.Tandberg, K.G.Lynn, T.E.Jackman, M.W. Denhoff, G.C. Aers, Phys. Rev. Let. **61**,187 (1988)

[1.24] S.M. Sze, Semiconductor Devices, Wiley, New York, (1986)

[1.25] J.F. Ziegler, J.P. Biersack, U. Littmark , The stopping and range of Ions in Solids, Pergamon Press, New York (1985)

[1.26] L.C. Kinerling, *Inst.Phys.Conf. Ser*, **31** p221

[1.27] H.J. Stein, W. Beezholed, *Appl. Phys Lett.* **17**, p442 (1970)

[1.28] J. Keinomen, M. Hautal, E. Rauhala, V. Karttunnene, A. Kuronen, J. Räisänen, J. Lahtinen, A. Vehanen, E. Punkka, P. Hautojärvi, *Phys Rev B*, **37**, p8269

CHAPTER 2

[2.1] S.M.Hutchins, *Ph.D Thesis*, (1985)

[2.2] R. Krause-Reyberg, H.S. Leipner, Positron Annihilation in Semiconductors, Springer, (1998)

[2.3] P.G. Coleman, ed., Positron Beams and their application, World Scientific (1999)

[2.4] J.M. Dale., L.D. Hulett, S. Pendyala, *Surf. Interface Anal.*, **2**, p199 (1980)

[2.5] S.M. Hutchins, P.G Coleman, R.J. Stone, R.N.West, *J.Phys. E: Sci. instrum.*, **19**, pp282-283, (1986)

[2.6] W.E. Kauppila, T.S.Stein, J.M. Wadehra, (Eds.) Positron (electron)-Gas scattering, World Scientific, pp 342-344 (1986)

[2.7)] N.B. Chilton, P.G. Coleman, *Meas. Sci. Technol*, **6**,pp53-59, (1995)

[2.8] A. Zecca, R.S. Brusa, M. Duarte Naia, *Meas.Sci.Technol.*, **5**, 61,(1994)

[2.9] A van Veen, H Schut, J. de Vries, R.A. Hakvoort and M.R. IJpma, *AIP Conf. Proc.*, **218** 171 (1990).

[2.10] H.J. Stein, W. Beezholed, *Appl. Phys Lett.* **17**, p442 (1970)

[2.11] J. Keinomen, M Hautala, E. Rauhala, V. Karttunnene, A Kuronen, J. Räisänen, J. Lahtinen, A. Vehanen, E. Punkka, Hautojärvi, *Phys Rev B*, **37**, p8269 (1988)

[2.12] J.F. Ziegler, J.P. Biersack, U. Littmark , The stopping and range of Ions in Solids. Pergamon Press, New York (1985)

CHAPTER 3

[3.1] A.P. Knights, P.G. Coleman, *Defect Diff. Forum* 183-5 (2000) 41.

[3.2] R. Krause-Rehberg, H. S. Leipner, eds., Positron Annihilation in Semiconductors: Defect Studies (Springer, Berlin, 1999).

[3.3] P. Hautojärvi, H. Huomo, J. Lahtinen, J.Mäkinen, A. Vehanen, *Mat. Sci. Forum,* **10-12**, 527, (1986)

[3.4] J. F. Ziegler, J. P. Biersack, U. Littmark, The Stopping and Range of Ions in Solids (Pergamon, New York, 1985).

[3.5] G.D. Watkins, in: Handbook of Semiconductor Technology, Ed. W. Schroeter (Wiley-VCH, Weinheim, 1999).

[3.6] P.G. Coleman, C.P. Burrows, A.P. Knights, *Appl. Phys. Lett.* **80**, 947. (2002)

[3.7] X.D. Pi, P.G. Coleman, R.M. Gwilliam, B.J. Sealy, *J. Phys. Condens. Matter* **15,** S2825. (2003)

[3.8] A. Polity, F. Börner, S. Huth, S. Eichler, R. Krause-Rehberg, Phys. Rev. B **58** (1998) 10363.

[3.9] R.E. Mason, P.G. Coleman, *App. Surf. Sci*, **252,** 3228, (2006)

[3.10] N.B. Chilton, P.G. Coleman, Meas. Sci. Technol. 6 (1995) 53.

[3.11] G.D. Watkins, Deep Centres in Semiconductors, P.Baruch (ed.) (Gordon and Breach, New York,1986)

[3.12] P.J. Schultz, E.Tandberg, K.G.Lynn, T.E.Jackman, M.W. Denhoff, G.C. Aers, Phys. Rev. Let. **61**,187 (1988)

[3.13] Data courtesy of P.G. Coleman, and C.P.Burrows. (2006)

CHAPTER 4

[4.1] A van Veen, H Schut, J de Vries, RA Hakvoort and MR IJpma, AIP Conf. Proc., **218** 171 (1990).

[4.2] A.P. Knights, A. Nejim, N.P. Barradas and P.G. Coleman, *Nucl. Instrum. Methods B* **148**, 340 (1999).

[4.3] P.G. Coleman and A.P. Knights, *Appl. Surf. Sci.* **149**, 82 (1999).

[4.4] A.P. Knights and P.G. Coleman, *Defect and Diffusion Forum*, **183-5**, 41 (2000).

[4.5] R. Krause-Rehberg, F. Börner, F. Redmann, W. Egger, G. Kögel, P. Sperr and W. Triftshäuser, *Appl. Surf. Sci.* **194,** 210 (2002).

[4.6] F. Malik, P.G. Coleman, A.P. Knights, R. Gwilliam, A. Nejim and O.Y. Ho, *J.Phys.: Condens.matter,* **10**, 10403 (1998).

[4.7] A.P. Knights, A. Nejim, P.G. Coleman, H. Kheyrandish and S. Romani, *Appl. Phys. Lett.* **73**, 1373 (1998).

[4.8] M.S. Janson, J. Slotte, A. Yu Kuznetsov, K. Saarinen and A. Hallen, *J. Appl. Phys.* **95**, 57 (2004).

[4.9] P.J. Simpson, M Spooner, H. Xia and A.P. Knights, *J. Appl. Phys.* **85**, 1765 (1999).

[4.10] M. Fujinami, T. Miyagoe, T. Sawada, R. Suzuki, T. Ohdaira and T. Akahane, *Phys. Rev. B*, **68,** 165332 (2003).

[4.11] K Saarinen, P Hautojarvi and C Corbel, in *Identification of Defects in Semiconductors*, ed. M Stavola (New York: Academic) p.42. (1998),

[4.12] H. Kauppinen, C. Corbel, K. Skog, K. Saarinen, T. laine, P. Hautojärvi, P. Desgardin and E. Ntsoenzok, *Phys. Rev. B*, **55**, 9598 (1997).

[4.13] F. Börner, S. Eichler, A. Polity, R. Krause-Rehberg, R. Hammer, and M. Jurisch, *Appl. Surf. Sci.* **149** 151 (1999).

[4.14] R Krause-Rehberg, F. Börner and F. Redmann, *Appl. Phys. Lett.* **77**, 3932 (2000).

[4.15] R Krause-Rehberg, F. Börner, F. Redmann, J Gebauer, R Kögler, R Kliemann, W Skorupa, W Egger, G. Kögel and W. Triftshäuser, *Physica B* **308-10**, 442 (2001).

[4.16] J.F. Ziegler, J.P. Biersack and U. Littmark, *The stopping and range of ions in solids* (Pergamon: New York) 1985.

[4.17] P.G. Coleman, C.P. Burrows and A.P. Knights, *Appl. Phys Lett*, **80**, 947 (2002).

[4.18] P.J. Scultz and K.G. Lynn, *Rev.Mod.Phys.* **60**, 701 (1988).

[4.19] A.P. Knights, F. Malik, P.G. Coleman, *Applied Phys Lett,* **75**, pp466, (1999)

[4.20] SSUPREM4, provided by Silvaco International (2003).

[4.21] P.G. Coleman, RE Mason, M. van Dyken and A.P Knights, *J.Phys.:Condens.Matter*, **17**, S2323 (2005).

CHAPTER 5

[5.1] N.B. Chilton, P.G. Coleman, *Meas. Sci. Technol.* 6 (1995) 53.

[5.2] A van Veen, H Schut, J de Vries, RA Hakvoort and MR IJpma, AIP Conf. Proc., **218** 171 (1990).

[5.3] M. A. Todd, P. P. Donohue, R. Watton, D. J. Williams, C. J. Anthony, and M. G. Blamire, in *Materials. for Infrared Detectors II* (SPIE-INT, Bellingham, 2002), Vol. 4795, p. 88.

[5.4] P. J. Wright, M. J. Crosbie, P. A. Lane, D. J. Williams, A. C. Jones, T. J. Leedham, and H. O. Davies, *J. Mater. Sci.-Mater. Electron.* **13**, 671 (2002).

[5.5] D. J. Keeble, B. Nielsen, A. Krishnan, K. G. Lynn, S. Madhukar, R. Ramesh, and C. F. Young, *Appl Phys Lett* **73**, 318 (1998)

[5.6] Q. Zhang, D.J. Keeble, P.G. Coleman, R.E. Mason, INTEGRATED FERROELECTRICS, 62: 119-125 (2004)

[5.7] S. McGuire, D.J. Keeble, P.G. Coleman, R.E Mason, Y. Koutsonas, T.J Jackson, *Jour. Appl. Phys.*(In press 2006)

[5.8] T. Friessnegg, B. Nielsen, and D. J. Keeble, *Integrated Ferroelectrics* **32**, 871 (2001).

[5.9] M. Hakala, M. J. Puska, and R. M. Nieminen, *Phys. Rev. B* **57,** 7621-7627 (1998).

[5.10] P. A. Lane, M. J. Crosbie, P. J. Wright, P. P. Donohue, P. J. Hirst, C. L.Reeves, C. J. Anthony, J. C. Jones, et al., *Chem. Vap. Deposition* **9**, 1 (2003).

[5.11] S. McGuire, Private Communication. (2003)

[5.12] P. Asoka-kumar, K.G. Lynn and D.O. Welch, J. Appl. Phys. **76,** 4935 (1994).